The University of Tasmania

COSMIC X-RAY SURVEYS

by

R.J. FRANCEY, B.Sc.(Hons.)

submitted in fulfilment of the
requirements for the degree of
Doctor of Philosophy

HOBART

August, 1970

This thesis contains no material which has been accepted for the award of any other degree or diploma in any University.

To the best of my knowledge and belief, the thesis contains no material previously published or written by another person except where due reference is made in the text.

R.J. Francey

CONTENTS

VOLUME 1

SUMMARY

ACKNOWLEDGEMENTS

SUMMARY

Chapters 1 to 3 are devoted solely to <u>review</u> of the X-ray sky, the environmental limitations on an experiment, and the techniques of X-ray detection. These are necessary for the design of proportional counters for a series of rocket surveys of the X-ray sky. Particular attention is given to the reduction of background noise, and significant improvements in the performance of laboratory tested detectors is achieved and discussed in Chapter 4. Chapter 4 also describes a wide range of calibration techniques developed and used on the rocket payloads. Because of the desirability of recording design detail, it is included in Chapters 1-4, contained in Volume 1. The first volume is used freely as a source of reference in Volume 2, the analysis section of the thesis.

Results from three early rocket flights were available for analysis. Preliminary results, published at the time of these flights are included in Chapter 5. These are

(1)   the discovery of an intense X-ray source in Centaurus on 4 April 1967 (flight I)

(2)   a measure of the decrease in intensity and steepening of X-ray spectrum of the source, Cen XR-2, by 20 April 1967 (flight II) and complete disappearance by 1 December 1967 (flight III). (The variability made Cen XR-2 unique among X-ray sources at the time.)

(3)   a possible source in Cetus, significant in view of

its large separation from the galactic disc (flight

II, III).

In Chapter 6, flight II data has been reanalysed in

detail and in the light of more recent evidence.   Two

significant findings are

(1)   An accurate and unambiguous location of Cen XR-2 in

galactic longitude.   The new position excludes a

number of objects (hard X-ray, optical, radio), whose

properties have been employed in constructing models

for the source.

(2)   An established variability of X-ray sources in the

Cygnus and nearby regions.

The properties of the variation in Cen XR-2 and a

similar newly discovered variable allow some restrictions

to be placed on source models.

With future low noise surveys in mind, the

possibility of galactic structure in the diffuse X-ray

background is investigated in Chapter 7.   Remarkable

similarities in the spectra of low frequency radio, X-ray

and extraterrestrial electron spectra are displayed, and

can be interpreted in terms of galactic phenomena with

some reservations.   The radio data are used to predict

possible X-ray anisotropies.

Finally, in Chapter 8 attention is given to the possibility of ground based surveys of X-ray stars. Extensive new information on the electron production rates in the ionospheric D-region are compiled and it is shown that the reported detection of a cosmic X-ray effect has implications on the chemistry of the ionosphere.

ACKNOWLEDGEMENTS

chapters were held with many others of the Physics Department staff in Tasmania, including Prof. G.R.A. Ellis.

To my wife who has typed and proof read this thesis goes my utmost praise and gratitude.

CHAPTER ONE

INTRODUCTION

1.1 X-RAY SURVEYS

It is almost a decade since the first detection and
identification of cosmic X-rays by Giacconi et al (1962).
In this time the great majority of experimental evidence
in X-ray astronomy has been gathered with rocket-borne,
and to a lesser extent balloon-borne, equipment —— a
situation demanded by the absorption of X-rays in the
earth's atmosphere. Of the many limitations imposed by
the vehicle on an experiment, the most restrictive is the
short observing time, and the more detailed information on
X-ray sources has generally come from recent flights
employing stabilized platforms to allow a small sky region
to be studied for the full flight duration.

Against the trend to concentrate and obtain detailed
information on a few sources, this thesis describes
techniques and results from more general rocket X-ray
surveys, aimed at providing relatively crude positional and
spectral data over a large area of sky. This approach has
been partly influenced by the type of vehicle available,
however the early flights in themselves have provided ample

justification for the continuation of a survey program.
Table 1.1 briefly summarizes the status of six rocket
flights carrying experiments prepared jointly by the
Universities of Adelaide and Tasmania (UAT), and to which
the author has contributed.

TABLE 1.1

Rocket Flight	Launch Date	Status	
		launch	experiment
I	4 Apr.1967	successful	successful
II	20Apr.1967	"	"
III	1 Dec.1967	"	partially successful
IV	21Jan.1969	failure	-
V	16Apr.1970	successful	data not yet analysed
VI	~Aug.1970	-	-

Anticipating later discussion, flight I observed an intense
X-ray source, Centaurus XR-2, in a region of sky previously
scanned with a null result; flight II, three weeks later,
showed a marked decrease in flux and change in spectral shape
for the source, these comprising the first unambiguous
determination of such variations in any X-ray object. By
the time of flight III, Centaurus XR-2 was below the
threshold of detection. This factor of variability, now
established for several X-ray sources (though generally not

so dramatic as in Centaurus XR-2), gives great significance
to the infrequent "pre-1970" surveys.

An example of the <u>continuing</u> importance of the early
surveys is provided by the flight II data, reanalysed in the
light of recent evidence, to provide significant results
reported for the first time in this thesis (Chapter 6). With
such considerations in mind the experimental detail for the
six UAT flights are included in sufficient detail (in
Chapters 2 - 5) to permit further reanalyses should future
findings warrant it. (At the same time the experimental
detail for the most recent flights shows significant
developments in the design of the survey X-ray detector.)

While the survey information on the spectra,
variability and distribution of point X-ray sources
contributes to the understanding of the nature of such
objects, great cosmological significance has been placed on
observations of the diffuse cosmic X-ray flux under the
assumption that it is extra-galactic in origin. Surveys of
the type discussed here are capable, under favourable
conditions, of elucidating information on a possible
galactic structure in the diffuse flux (Chapter 7), and low
frequency galactic radio emissions can be used to predict
possible anisotropies to be investigated in such surveys.
Upper limits on such anisotropies place restrictions on

models of the galaxy.

A completely different approach to the problem of
monitoring cosmic X-rays involves the ground based detection
of secondary effects produced in the earth's atmosphere by
absorbed X-rays. This is a most exciting possibility from
the point of view of determining past history of sources,
for example from existing ionospheric records. A preliminary
analysis of such effects (Chapter 8) suggests an alternative
approach, that of using known X-ray sources as a tool in the
study of ionospheric processes; perhaps the first "use" of a
new science.

The remainder of this chapter is devoted firstly to a
familiarization with units and with the influence of
atmospheric, and interstellar matter on X-rays. The
limitations of detectors and vehicles are mentioned, followed
by a general discussion on the types and significance of
X-ray sources one might expect to see in a survey of the sky.
Finally the different nomenclatures applied to the X-ray
sources are summarized.

1.2   UNITS

X-ray astronomy is one of many disciplines studying
the universe by observing its electromagnetic radiation. The

cosmic X-ray photons are most commonly described in terms of

their _energy_ ($h\nu$) in units of _kilo electron volts_ (keV), a

course adopted here. However frequent reference is also

made to the wavelength of the X-rays, measured in angstroms

($\overset{o}{A}$), and the following are useful relationships:

$$h\nu(\text{keV}) \;=\; 1.60209_{10}{-9}. \;\; h\nu(\text{ergs}). \tag{1.1}$$

$$h\nu(\text{keV}) \;=\; \frac{hc}{\lambda(\overset{o}{A})_{10}{-8}} \;=\; \frac{12.3981}{\lambda(\overset{o}{A})} \tag{1.2}$$

where the Planck constant $h = 6.62554_{10}{-27}$ erg.sec. and

$c = 2.997925_{10}10$ cm.sec^{-1}. (The Algol notation for powers

of ten, i.e. using subscript 10 followed by the exponent, is

used throughout).

Figure 1.1 summarizes the order of magnitude

relationships existing between different units commonly

employed to describe the electromagnetic spectrum, and gives

perspective to the present endeavours in X-ray astronomy.

The atmospheric transmission as a function of incident photon

energy, taken from Rossi (1965), is included, and the

relevant X-ray section is now discussed in more detail.

1.3   THE ATMOSPHERE

The severe absorption of low energy X-rays in the

earth's atmosphere is the dominating overall restriction on

present experimental methods to directly measure cosmic
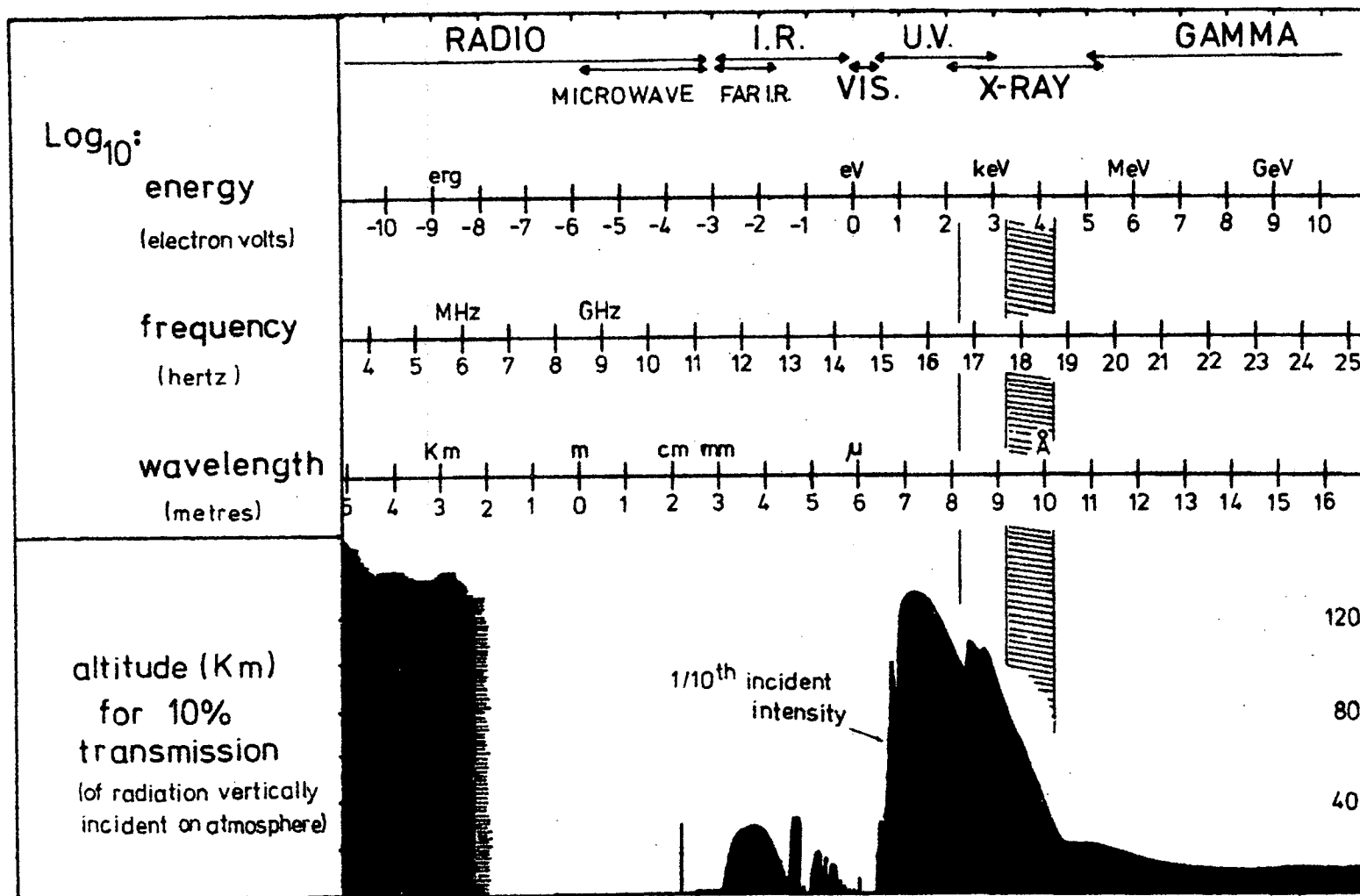
FIGURE 1.1: The Electromagnetic Spectrum: Units and Atmospheric Absorption

X-rays. In both direct and indirect observations an accurate

knowledge of atmospheric properties is required. In this

thesis data from the Cospar International Reference Atmosphere

(CIRA), 1965 has been employed. Of prime importance is the

<u>mass</u>, x g.cm^{-2}, of atmosphere between source and observer,

defined as the integral of the density along a line of sight

between the two, $\int \rho dl$. Figure 1.2(a) shows the mass of

atmosphere above an observer at altitude H (Km) in the

direction of a source at zenith angle z (degrees). The

solid lines are for the CIRA mean atmosphere and for z = 0°,

60°, 80°. These have been obtained from the integration of

a density function approximating a curved atmosphere,

discussed in detail in section 8.2. The approximation is

accurate to within a few percent for z < 80°, however for

the case z = 90° (dashed line) the more accurate Chapman

function correction (Wilkes, 1954) has been used on the CIRA

mean atmosphere. The dotted curves are for z = 0° but apply

to the maximum positive (summer, high latitudes etc.) and

negative (winter, high latitude) deviations from the mean

density profile, defined as deviations exceeded less than

five percent of the time, including data from "all seasons,

latitudes, times of day and solar flux". The extreme values

are unlikely to apply to an appreciable thickness of

atmosphere at any one time and should be taken only as limits.

The interaction of X-rays with the atoms of the atmosphere is discussed in detail in section 3.1.1. It is possible to define an effective mass absorption coefficient, $\mu g^{-1} cm^2$ for air, dependent only on incident X-ray energy, which along with the mass of atmosphere traversed by a beam of X-rays gives the percentage transmission, T, of the beam, i.e.

$$T = \exp(-\mu x) \qquad (1.3)$$

Mass absorption coefficients for air as determined by Henke et al (1967), supplemented at higher energies by data of Victoreen (1949), are shown in figure 1.2(b). Both are for an atmospheric composition 78% N_2, 21% O_2 and 1% Ar and are discussed further in Chapter 3.

For example to measure 90% of 1.5keV X-rays incident vertically on the mean atmosphere, an efficient detector must be at an altitude corresponding to $\sim 9.0_{10}-4$ g.cm^{-2}, i.e. 94 Km; for a source on the horizon $(z = 90^{\circ})$, the corresponding figure is 120 Km. It is interesting to note that vertically incident 1.2keV X-rays and 0.35keV X-rays can both be detected with 90% efficiency at 97 Km because of the O_2, N_2 absorption edges. At the high energies, 90% of vertically incident 10keV photons reach 76 Km.
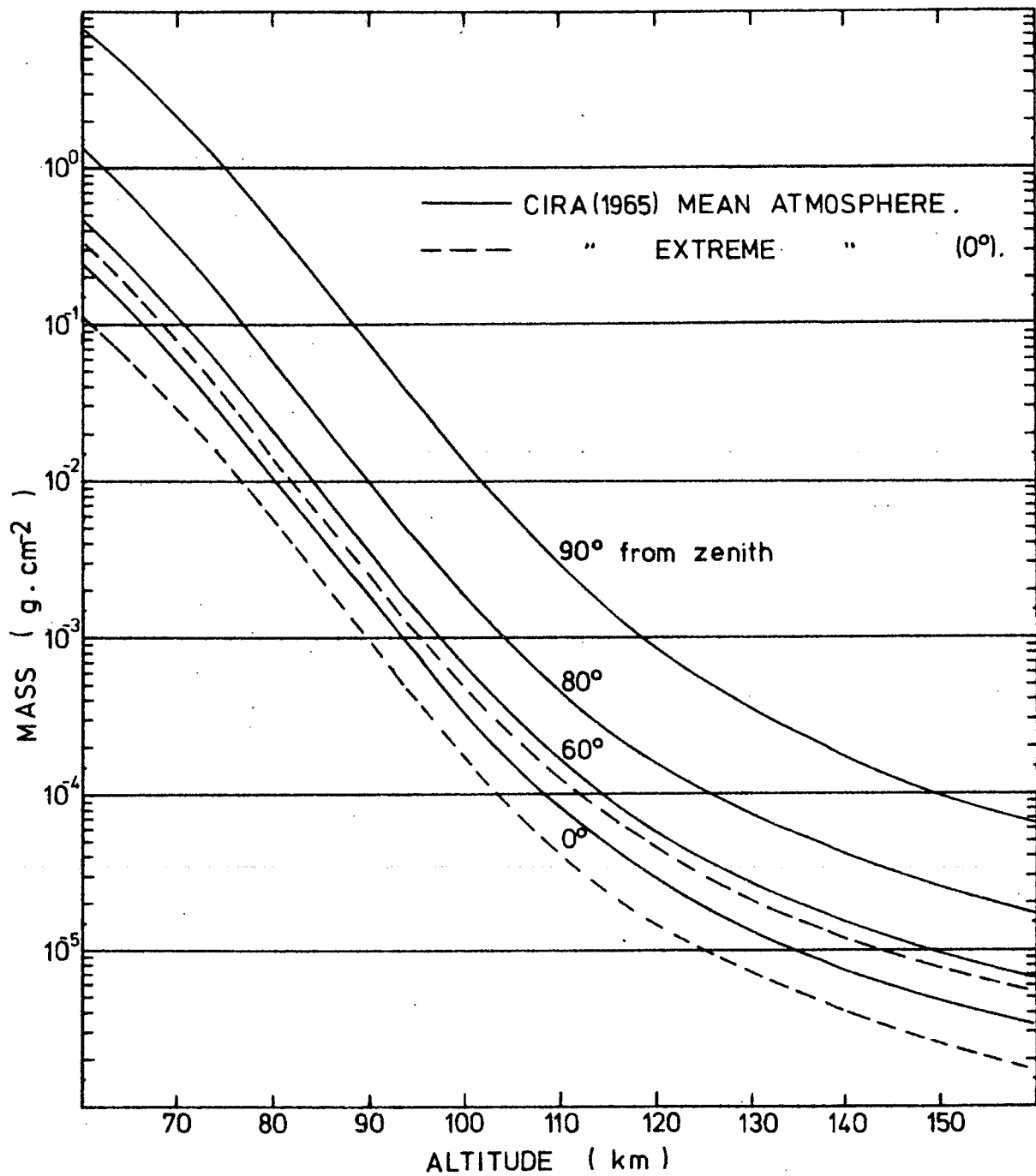
FIGURE 1.2a: Mass (g.cm^{-2}) of Atmosphere as a function of
Altitude and Zenith Angle
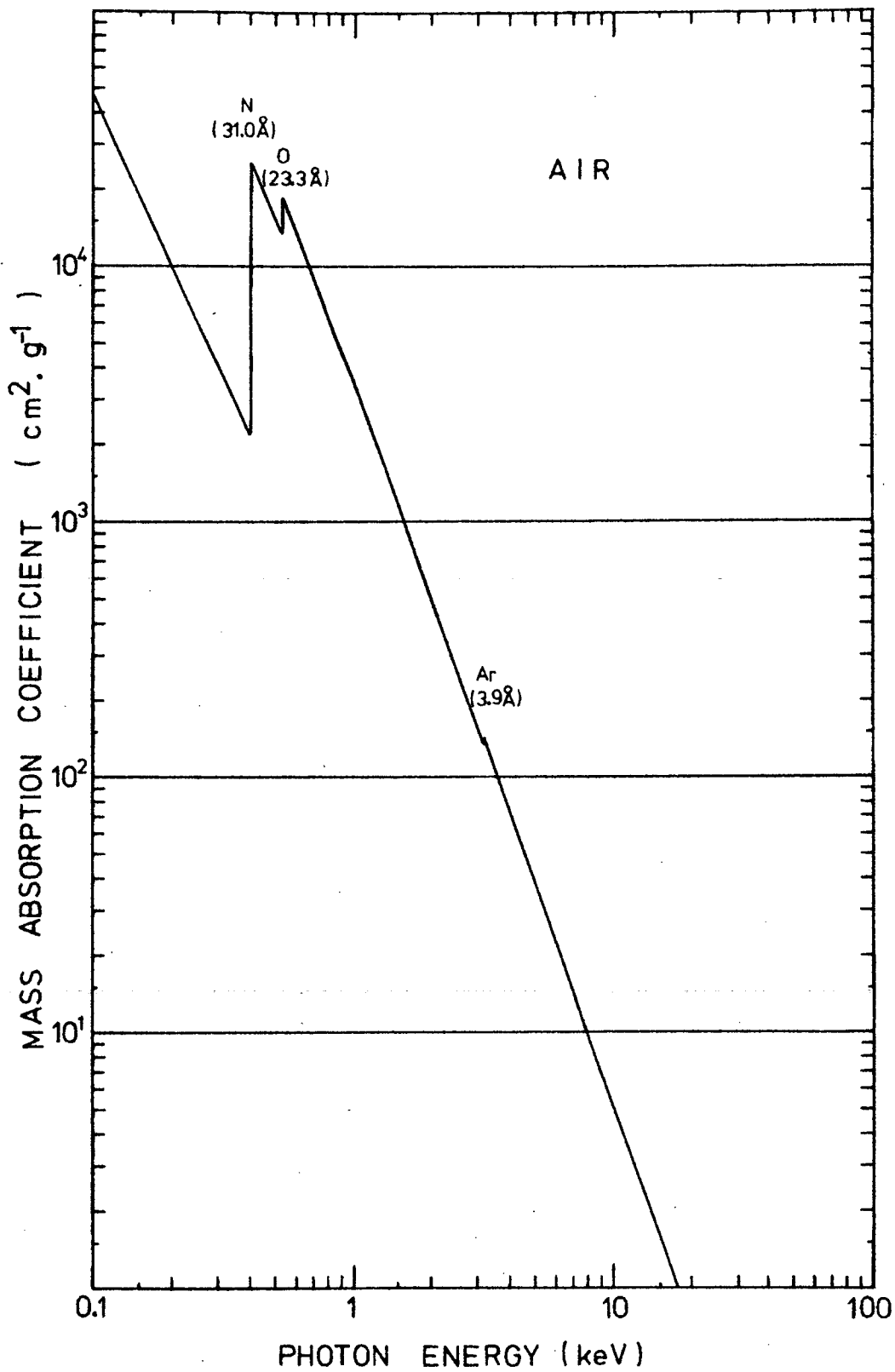
FIGURE 1.2b: X-ray Mass Absorption Coefficients of Air

1.4   INTERSTELLAR ABSORPTION

The literature pertaining to absorption of X-rays in interstellar matter has recently been reviewed by Fenton (1969), and the solid line of figure 1.3 is adapted from this work. The optical depth in units of hydrogen atoms cm^{-2} is given as a function of photon energy. These values were originally derived from those of Bell and Kingston (1967), using their photo ionization cross sections and the cosmic abundances of Aller (1961).

Recently Brown and Gould (1970), have improved estimates of the photo ionization cross section of atomic helium and quoted evidence for lower relative abundances of helium and neon. The overall effect on the total optical depth is to increase it as shown by the dashed line in figure 1.3. As better experimental photo ionization data (e.g. Henke et al, 1967) and cosmic abundance data become available these values may be again adjusted. However at the moment much larger uncertainties are associated with "clumpiness" of the interstellar matter, making it difficult to generally apply these curves. (Optical depth is also shown in parsecs, $3.084_{10}18cm$, assuming 0.5 hydrogen atoms cm^{-3}.)

The results of X-ray measurements on objects for which independent distance estimates exist, are included in
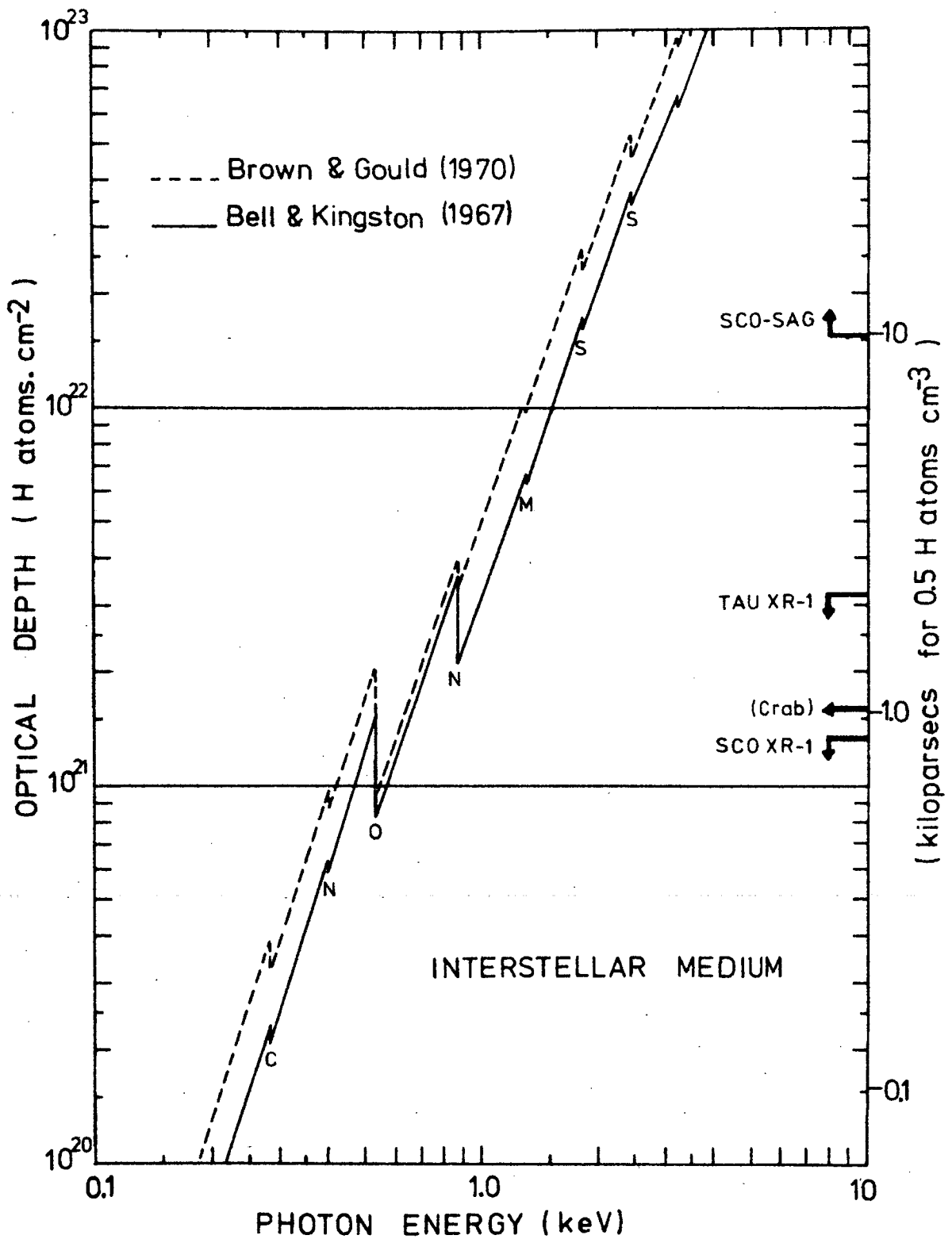
FIGURE 1.3: Interstellar Absorption of X-rays

figure 1.3, taken from the data of Rappaport et al (1969b),

and adjusted to the Brown and Gould interstellar model.

If intergalactic matter is predominantly hydrogen with

a number density about 10^{-5} cm^{-2}, as suggested by Gould (1967),

then intergalactic absorption above 1keV is small over

distances comparable to the radius of the universe.

1.5   DETECTOR AND VEHICLE LIMITATIONS

The techniques of X-ray detection, with emphasis on the

astrophysical application, have recently been reviewed

comprehensively and lucidly by Aitken (1968). Many of the

following points are discussed at greater length and are

fully referenced in his paper.

(1)   Of the X-ray detectors which intrinsically give

information on the energy of an absorbed photon, solid state

detectors have by far the best energy resolution. The

requirement for the solid state element to be sealed in an

evacuated cryostat and kept at liquid nitrogen temperatures

have prevented their wide use in spacecraft. In any case,

sensitive detection areas are limited ($\lesssim$ 30cm^2) with present

technology.

(2)   Proportional counters give the next best energy

resolution for X-rays. Because of the ease of construction

into large, relatively lightweight arrays (500 - 1000 cm²
sensitive area) they have been used almost exclusively in
rockets over recent years, and in particular in the six UAT
payloads.   Proportional counter theory and operation are
discussed extensively in Chapter 3.   Essentially the counter
comprises a sensitive gas volume in which an X-ray is
absorbed releasing electrons. The electrons drift and
avalanche under the influence of a strong electric field
giving a sufficient charge movement to be detected by low
noise, high gain electronic amplifiers whose pulse output
is then proportional to the X-ray energy. The gas must be
contained in a pure state, requiring a thin entrance window
which determines the low energy limit of the counter
sensitivity (∼1.5keV). The gas depth determines the upper
limit (∼15keV). It is the problem of gas confinement with
large areas of exposed thin windows (particularly with the
possibility of micro-meteorite damage), which gives rise to
a lack of long term stability and prevents wide use on
satellites.

(3)   Above 15keV good detection efficiency is maintained by
scintillation counters. Energy resolution is worse, and less
well understood than for proportional counters. In particular,
the situation can be further complicated for X-ray energies
<15keV by crystal geometry and surface conditions. The

typical, steeply falling, cosmic X-ray spectra (low fluxes at high energies), discussed below, make the scintillator ($\lesssim$ 200cm^2) unsuitable for rockets because of the lack of observing time. It is ideal for balloon observations (>20keV) for several hours) and has recently been successfully employed, though with a very crude spectral capability, at energies >3keV on Vela satellites (Conner et al, 1969). A slight spectral distortion by scintillators at high photon energies (>60keV) has been recently noted by Trombka (1970).

(4)   Geiger counters were used on the first experiment to detect cosmic X-rays. Neither these nor external photoelectric effect detectors, with great potential for use at energies < 1keV, intrinsically give information on the X-ray energy.

(5)   Focusing or imaging devices carried on satellites promise to revolutionize X-ray astronomy. Relatively large collection areas ($\sim$50cm^2) will focus low energy X-rays ($\lesssim$1keV) onto a small solid state or proportional counter. The small counter size relieves many of the problems mentioned above and implies marked improvement in signal to noise ratio since noise is chiefly due to cosmic ray induced counts. The greatest improvement is in angular resolution but the detector requires a stabilized platform, and reasonably accurate prior positional information for an object of interest is required (such as might be obtained

with the survey type payloads described later). A

comprehensive preview to the astronomical application of such

devices is given by Giacconi et al (1969).

The restrictions imposed on a detector by the rocket

environment are discussed fully in Chapter 2.

1.6   THE X-RAY SKY

The 1.5 to 15 keV sky, as seen by a typical freely

scanning rocket experiment contains some 30 to 40 discrete

"stars", superposed on a diffuse background. The stars are

concentrated towards the Milky Way and appear to be

correlated with local spiral arm directions (e.g. Gursky et

al, 1967). Photon fluxes ranging from about 100 $cm^{-2} sec^{-1}$ to

less than 0.1 $cm^{-2} sec^{-1}$ (determined by detector sensitivity)

are observed, compared to about 9 photons $cm^{-2} sec^{-1} ster^{-1}$

due to the diffuse flux.

Apart from significant recent developments the following

relies on similar reviews e.g. by Morrison (1967), Harries

(1968), and Rossi (1968). The main aim is to give an

overall picture of the types and significance of X-ray

sources one might expect to see in a sky survey.

1.6.1 Identification

Only very few of the brighter stars have permitted sophisticated positional determination (to within 1 - 10 minutes of arc), and in general the 1 to 5° accuracy typical of survey rockets is insufficient to make identification with optical or radio emitters, particularly close to the galactic plane. However in cases where certain identification has been made, this has given a dramatic increase in the understanding of the nature of the X-ray stars, and peculiar properties of these objects have been used to make further identifications for X-ray stars not so well located.

The first identification was that of <u>Taurus XR-1</u> with the optical and radio source, the Crab Nebula, supernova remnant SN 1054. X-rays were observed from an extended region ($\sim$100" arc), coinciding with optical emission from the Nebula and lying within the more extended radio emitting region (Bowyer et al, 1964, Oda et al, 1967). The discovery of a pulsed component of the Tau XR-1 X-ray emission (Fritz et al, 1969, Bradt et al, 1969) amounting to some 10% of the total X-ray flux, whose period of $\sim$30 m.sec coincides exactly with pulses in the radio (Staelin and Reufenstein, 1968), infra red (Neugebauer et al, 1969a) and optical (Cocke et al, 1969) from a centrally located star, coupled with similar wide band information on the nebula

has given unparalleled information on an astronomical object
(apart from the sun).

The Crab pulsar, NP 0532, is the only pulsar so far
observed to radiate at X-ray (and optical) energies, and
there are no positive identifications of X-ray sources with
other known supernova remnants. Weak X-ray sources near the
positions of Cassiopiea A, Tycho's super nova (SN 1572)* and
Vela X (pulsar PSR 0833-45), may be associated with these
super novae remnants and Cen XR-2 may be associated with
possible SN remnant 13S6A (see Chapter 6), but verification
by obtaining accurate positions or pulsed emission in X-rays
is required. A general statistical correlation of X-ray
stars with super nova positions, summarizing in particular
the super nova data, is given by Poveda and Woltzer (1968);
this is extended by Milne (1970).

The only other certain identification (again apart from
the sun) is for the strong source Scorpius XR-1. An angular
extent of < 20" arc and position to within 1-2 minutes of
arc prompted identification with an unusually blue, faint
optical object reminiscent of old novae (Sandage et al, 1966).
Subsequent observation of correlated optical and X-ray
variations (e.g. Mark et al, 1969a, Hudson et al, 1970)
leaves little doubt on the correctness of the claim.
Additional data have since been collected at radio

*Note added in proof: High resolution evidence for X-ray
sources in the Cas A, SN 1572 positions has been obtained
by Gorenstein et al., Astrophys.J., 160, 1970.

(Ables, 1968) and infra red (Neugebauer et al, 1969b)

energies, both exhibiting variations.

The galactic source GX 3+1 lies within a degree of a

variable, extreme ultraviolet object suggestive of an extreme

Wolf Rayet star or supernova (Freeman et al, 1968) and also

a weak, (apparently) thermal radio source (Goss and Shaver,

1968).

The identification of Cygnus X-2, located to within 10'

arc, with a nearby optical object on the basis of its

similarity to the optical counter part of Sco XR-1 must still

be considered with some reserve. A similar identification

process in the case of Cen XR-2 (admittedly with inferior and

more confusing X-ray data) is shown in Chapter 6 to be

erroneous.

The remaining reasonably well justified identifications

are for objects well removed from the galactic plane and

which appear to be examples of extra galactic X-ray sources.

The well confirmed source Vir XR-1 is within 1° of the

optical galaxy M87 (radio galaxy Vir A), a remarkable

coincidence for a region of sky so sparsely populated by

examples of either object (Bradt et al, 1967). Mark et al

(1969b) have reported a weak source of X-rays, 12° in extent,

coinciding with the position and extent of the Large

Magellanic Cloud, our nearest intergalactic neighbour. Both

identifications require verification which can only come with

better X-ray counting statistics.

1.6.2 Spectra

The majority of source spectra, describing measurements in the 1.5 to 15 keV energy range (and also at "balloon" energies) have been fitted by one or other of two simple spectral forms.

The first is a power law of the form

$$\frac{dN}{d(h\nu)} = \text{const.} \ (h\nu)^{-\alpha} \ \text{photons} \ cm^{-2} sec^{-1} keV^{-1} \qquad (1.4)$$

Tau XR-1 is the prototype of such sources. Combining the Crab spectral information from radio energies to X-rays of several hundred keV, a single smooth curve similar to (1.4) but with slowly varying index α, is an excellent fit over the whole range. The low energy radiations (optical, radio) are polarized in a manner suggesting synchrotron radiation, resulting from the interaction of high energy electrons (in this case with a spectrum similar to equation 1.4 but with exponent $\gamma = 2\alpha + 1$) and a magnetic field. For this reason power law X-ray spectra have been loosely associated with the synchrotron process.

The problems associated with this model for the Crab are the extremely high electron energies ($> _{10}12$ eV) required to give X-rays from the anticipated weak fields ($< _{10}-3$ gauss) and the fact that the radiative lifetimes of

such electrons are extremely short (< 1 year). The discovery

of the Crab pulsar has provided a much sought after energy

source, which might be capable of continuously accelerating

electrons to high energies. Tucker (1969) suggests a basic

model of a rotating neutron star losing mass in the presence

of a large magnetic field, which can account for both

extended and point X-ray stars. The extended sources

(prototype the Crab) represent a situation where the energy

density of protons and electrons forming a neutron star wind

is greater than the star's magnetic energy density and the

particles deposit energy far out in the nebula. Relativistic

electrons are produced in the transfer of energy between

protons and electrons in the shock wave and by magnetic

pumping in hydromagnetic waves which are generated by

fluctuations in the mass loss rate. These radiate by

synchrotron emission over the whole E M range. In the other

extreme of the neutron star magnetic field energy exceeding

that in the mass flow the electrons are accelerated and

radiate in radiation belts close to the star resulting in a

source with small angular diameter. (In applying the latter

case to Sco XR-1 Tucker points out that to explain the gross

relationship between the observed X-ray and optical

radiation, severe restrictions are placed on the angular size

in terms of the flux density and magnetic field strength.

This would imply that Sco XR-1, if pulsing would have a

period of ∼6 m sec.). The restrictions placed on an electron

spectrum by the observed X-ray spectrum are not accounted for

above but are discussed for the case of Tau XR-1 by Tucker

(1967a) (and for Sco XR-1 by Manley (1966), see below).

The Sco XR-1 X-rays have normally been described by the

second simple spectral form, an exponential

$$\frac{dN}{d(h\nu)} = \text{const. } \exp(-\beta . h\nu)/h\nu \text{ photons cm}^{-2}\text{sec}^{-1}\text{keV}^{-1} \quad (1.5)$$

Of the few processes considered as likely sources of cosmic

X-rays (Rossi, 1968) one is due to electron free-free

transitions, or bremsstrahlung, from matter in thermal

equilibrium. For a Maxwellian distribution of electrons of

temperature T, density N_e cm^{-3}, encountering ions (N_z cm^{-3})

of charge Z, the bremsstrahlung flux at earth will be

$$\frac{dN}{d(h\nu)} = 1.033_{10}-11 \ \frac{N_e V T^{-\frac{1}{2}}}{d^2} \sum N_z Z^2 \ g(Z,T,h\nu) \ \exp(-h\nu/kT)/h\nu$$

$$\text{photons cm}^{-2}\text{sec}^{-1}\text{keV}^{-1} \quad (1.6)$$

where the Boltzman constant

$$k = 8.616_{10}-8 \ \text{keV degK}^{-1} \quad (1.7)$$

and $g(Z,T,h\nu)$, an averaged Gaunt factor, is a slowly varying

function discussed and tabulated by Karzas and Latter (1961).

V is the volume occupied by the plasma, situated d cm. from

earth. For $h\nu/kT \gg 1$, g = 1, and this case is represented

by (1.5) for an isothermal, uniform density cloud of matter,

optically thin to its own radiation. At the temperatures

necessary for X-radiation (T $>_{1 0}$7 degK, $1/\beta \sim$ 0.8keV), the

matter will be fully ionized and gaseous, i.e. a plasma.

Naturally X-ray sources with exponential spectra, such as

Sco XR-1, have been freely associated with bremsstrahlung

radiation from thin hot plasmas particularly since such

radiation has been observed for many years from the solar

corona.

The most comprehensive treatment of radiation from thin

hot plasmas is given by Tucker and Gould (1966), and Tucker

(1967). Bremsstrahlung radiation from a plasma with the

cosmic abundance of elements only predominates for temperatures

above about $8_{1 0}$6 degK, below this radiative recombination is

more important. In both cases, line emission from inelastic

electron collisions is present, and for different abundances,

e.g. for that expected in the outer shell of supernova, line

emission can dominate in the X-ray region at around $_{1 0}$7 degK.

Comparison of the X-ray spectrum of Sco XR-1 with

optical spectra (Mark et al, 1969a) and radio flux (Andrew

and Purton, 1968) shows that a simple optically thin isothermal

plasma does not explain the measurements, some attenuation in

the two lower energy bands being required. Chodil et al (1968a)

explain the data in terms of thermal bremsstrahlung from a

plasma not completely transparent to its own radiation, with

some additional interstellar absorption. Recent very low

energy measurements ($<$1keV) by Grader et al (1970), compared

between two flights and also with results of other authors

appear to require a variable absorption of these X-rays in

cool matter. A further difficulty is that of heating and

maintaining a plasma at temperatures $_1{_0}7 - _1{_0}8$ degK. Coronal

emission from hot Wolf Rayet stars, and very close flaring

stars is a possibility however most theories obtain heat by

stopping matter which falls in onto a star from a binary

companion, e.g. Prendergast and Burbidge (1968). Cameron

(1969) avoids difficulties associated with the binary model

by proposing a ring of matter evolving around and accreting

onto a white dwarf. Tarter et al (1969) in a study of the

interaction of X-ray sources with optically thin environments

show that the absorption of medium to low energy X-rays in

the relatively dense emission regions necessary for mass

accretion heating, may cause spectral turn over at around

1keV. Such processes may explain the "variable soft X-ray

emission" required by Grader et al. The location of

absorption edges in the spectrum will indicate whether

absorption is occurring in ionized gas near the source or in

more distant neutral matter (Felten and Gould, 1966).

As mentioned above, Tucker (1969) and Manley (1966)

have avoided the problems of high temperature plasmas by

proposing synchrotron models for Sco XR-1. Manley and Olbert

(1969) have followed up this possibility in considerable
detail. They show that if a radiation instability peculiar
to bounded optically thin magneto-active plasmas can
engender fluctuations in the magnetic field, electrons can
be accelerated to produce a hard spectrum which on
interaction with the magnetic field gives a synchrotron
spectrum in agreement with the observed radio, optical and
"exponential" X-ray data. The underlying plasma is taken to
be at $_1 {}_0 5$ degK to explain observed optical lines (Tucker, 1967a)
and the lack of observed optical polarization is attributed
to a lack of preferred direction in the magnetic field. While
the short term variations in the X-ray and optical fluxes can
be adequately described in terms of magnetic fluctuations,
the variable soft X-ray absorption mentioned above, if
confirmed, may prove a much bigger problem to this thin
source model than to the thermal models. Manley and Olbert
strongly criticize the thermal models relying on mass
accretion on the basis of optical thickness at the low
X-ray energies. Zel'Dovich and Shakura, (1969) carry out a
detailed analysis for a model of accretion onto a neutron
star by interstellar matter or previously ejected matter, and
find no such difficulties for X-rays $> 1\text{keV}$.* On the other
hand Cameron admits to an optically thick ring of matter but

*Note added in proof: Zel'Dovich and Shakura predict a
complex Sco XR-1 spectrum in excellent agreement with recent
high energy observations ($>20\text{keV}$) indicating a "two component"
source (G.R. Reigler, E. Boldt and P. Serlemitsos, Nature 226,
1041, 1970.).

suggests that X-rays will be visible for observers at a
higher latitude than the ring (absorption and re-radiation
of the primary X-rays and nuclear burning of the accreted
mass will make this type of source highly luminous in the
hard UV region). To complete the circle of arguments,
Sartori and Morrison in 1967 proposed a thermal model for
the Crab in which bremsstrahlung from a non isothermal cloud
adequately represents the X-ray power law spectral shape.

A critical test distinguishing between the thermal and
non thermal processes is provided by the detection of X-ray
line emission, only expected from the very hot plasmas. As
pointed out by Angel (1969), on the other hand, the non
detection of lines does not necessarily imply a non thermal
source, since e.g. in the case of Sco XR-1, the large optical
depth at optical and radio frequencies and the high
temperatures of the thermal plasma implies significant
electron scattering accompanied by doppler shifts tending to
broaden the spectral lines. Nevertheless Holt et al (1969)
do report an indication of iron line emission at 6.9keV in
the Sco XR-1 spectrum. Confirmation of the line will then
confirm the hot plasma origin of X-rays at least for this
source. At the same time the Holt et al results, like those
of Grader et al at lower energies, foresee future
difficulties with the simple isothermal bremsstrahlung model.

Their continuum data give an excellent fit to the simple
exponential given by equation (1.5). The deviation from an
exponential introduced by the more accurate isothermal
bremsstrahlung model, i.e. equation (1.6) with $g \neq 1$, produces
significant deviations from the data.

Before concluding the discussion of spectra, a third
possible simple spectral form is worth brief mention. This
is the other extreme of the thermal model, i.e. for completely
optically thick thermal matter. This results in Planck
radiation with flux

$$\frac{dN}{d(h\nu)} = 9.88_{10}31 \quad \frac{(h\nu)^2}{\exp(h\nu/kT)-1} \quad ph. \ cm^{-2} sec^{-1} keV^{-1} \quad (1.8)$$

Such <u>black body</u> radiation in X-rays will come from highly
condensed hot objects such as neutron stars. Rapid cooling
by neutrino emission has generally led to the dismissal of
this radiation as a source of cosmic X-rays. The properties
of these objects are reviewed and discussed in considerable
detail by Harries (1968).

This does not claim to be a comprehensive review,
however it does indicate the type of spectral measurements
required to resolve the nature of the X-ray sources. The
UAT results reported in this thesis can be equally well
applied to any of the three spectral forms given by equations
(1.4), (1.5) or (1.8), and these simple forms adequately

represent the observational X-ray data for the arguments used herein.

1.6.3 Variability

There have been frequent claims of flux variations from early surveys, e.g. Friedman et al (1967), Fisher et al (1968). It is perhaps significant that all the sources claimed to vary were located in regions of high source density (e.g. the galactic centre and the Cygnus regions) where source separation was small compared with the angular resolution of detectors. More recent high resolution surveys of the galactic centre region by Gursky et al (1967), Bradt et al (1968), Bunner and Palmieri (1969), and Mayer et al (1970), with finer resolution, are compared by Mayer et al, who claim that there is no clear evidence for gross time variations (within a factor of 2) in the intensity of these sources for a period of several years.

A possible exception is the first source claimed to be variable, Cyg XR-1 (Byram et al, 1966). Measurements with geiger counters in June, 1964, and April, 1965, showed a factor of four decrease in flux while Cyg XR-2 remained constant. However as pointed out by Harries (1968), data were collected on very few scans and with very different spectral sensitivities. Subsequent rocket flights, spanning several years, have shown no significant variations though

flux variations of less than about 30% are not precluded

(Meekins et al, 1969). On the other hand Meekins et al

claim variability for the Cyg XR-2 source. The Cygnus

observations, are discussed in more detail in Chapter 6,

along with UAT flight II results in this region.

The question of whether or not X-ray sources exhibited

variations was conclusively answered at the time of the first

two UAT flights April, 1967. The strong source Cen XR-2,

first observed on these flights was seen again in May, 1967,

by Chodil et al (1967b), who claimed that this region was

free of sources in October, 1965. The detailed flux and

spectral changes over a period of three weeks in April,

obtained with two identical detection systems is part of the

content of this thesis and was published in 1967, Francey

et al (1967). The subsequent decrease to below detection

threshold in the order of months, and a reported reappearance

of Cen XR-2 at balloon and rocket energies is discussed fully

in Chapter 6. That such dramatic events are relatively

common is indicated by a similar outburst and decay of the

source Cen XR-4, just over two years after the reign of

Cen XR-2. (Evans et al, 1970).

Variability of Sco XR-1 (both long and short term) and

Tau XR-1 (the pulsed emission) are now established factors.

The production mechanisms for X-rays have little trouble in

accounting for spectral variability as such. However the

details of the variation can place severe restrictions on the

model as has been suggested above in the case of the possible

soft X-ray variations of Sco XR-1. Similarly the detailed

flux and spectral changes of Cen XR-2, Cen XR-4 are

incompatible with the changes expected from a cooling neutron

star emitting black body radiation (see 6.2.6). No short term

variations would be expected from a region the size of the

Crab Nebula, or for example from the Large Magellanic Cloud

source.

1.6.4 The Diffuse Flux

The diffuse X-ray flux measurements have generally been

fitted by a power law similar to (1.4). There is a very

strong suggestion of a spectral break and steepening above

about 50keV and below 1keV and further complexity is indicated

above 1MeV (Chapter 7). Again there are problems in comparing

measurements from different detector types particularly since

many of the available results have been obtained with

detector fields of view suitable for point source surveys

but far from ideal for collecting information on the background.

On the basis of isotropy it is usually assumed that the

diffuse X-rays are extra-galactic in origin. Theories of

origin can be grouped under the headings intergalactic

space, unresolved extragalactic discrete sources, and the

local galaxy.

From _intergalactic space_ one can include:

(1)   Non thermal bremsstrahlung. Boldt and Serlemitsos (1969) discuss the interaction between suprathermal ($\lesssim$MeV) protons and ambient electrons. Silk and McCray (1969) consider keV-MeV electrons interacting with a low density ionized medium in an expanding universe. Both give continuous exponential spectra which can approximate a two component power law and are attractive as sources of the relatively "flat" spectra observed < 50keV.

(2)   Inverse Compton radiation involving meta-galactic electrons and both starlight and a universal 2.5 - 3 degK black body radiation. The plausibility of this process was established by Felten and Morrison (1966). A power law electron spectrum produces a power law X-ray spectrum with breaks due to electron losses at $\sim$40eV (3 degK) and $\sim$1MeV (starlight). Making a necessary adjustment for the evolution of the black-body energy density, ($\rho < (1 + z)^4$, z the red shift), does not provide a 50keV break but more easily accounts for the observed X-ray intensity (Brecher and Morrison, 1967, Payne, 1969).

(3)   Thermal bremsstrahlung (free-free emission from a dense, hot intergalactic plasma). First suggested by Hoyle (1963), the steep thermal shape does not agree with observations above 1keV but may contribute below this energy. Henry et al (1968) interpret excess corrected fluxes

at 0.28keV as direct evidence of a dense intergalactic plasma. In view of revised interstellar absorption (section 1.4), clumpiness of the interstellar medium (Bowyer and Field, 1969, 1970) and a possible galactic component (see below), it appears as if the "primordal plasma" is not yet required. Pottasch (1966) predicts strong line emission in soft X-rays from such a plasma.

(4)   Stecker (1969) evaluates a high energy component peaking at $70(1 - z_{max})^{-1}$ MeV, resulting from π^0 decay following cosmic ray interactions at any early epoch. Evidence for a feature in the spectrum at 1MeV (Vette et al, 1970) would imply $z_{max} \simeq 100$ and a spectral cut off at 7GeV (Fazio and Stecker, 1970).

Unresolved extragalactic discrete sources were suggested by Gould and Burbidge (1963) and again by Friedman (1967).

(1)   Contributions from normal galaxies require evolutionary effects to be appreciable and Silk (1968, 1969) develops this model. A spectral break $\sim$10keV is introduced by considering the combined effect of Sco XR-1, Tau XR-1 type spectra. Using a Lemaître universe, Brecher and Silk (1969) predict a 480 MHz (red shifted 21 cm) absorption and a 173keV (red shifted positron recombination) emission feature for this model.

(2)   Inverse Compton scattering of the 3 degK black body radiation and electrons in remote radio galaxies and quasars was suggested by Bergamini et al (1967). A 60keV break can be obtained and implies a break in the synchrotron emission from these sources at 60 MHz (Felten and Rees, 1969). The number of sources necessary to produce the observed background intensity is about 10 per square degree implying 7% intensity variations due to random clumping in 5° fields. The constraint of interaction with an intergalactic medium on any theory involving X- or gamma rays emanating from large red shifts is pointed out by Aarons and McCray (1969).

Many of the above mechanisms have been considered by their authors as possible contributors of a galactic diffuse X-ray flux, and are generally found to produce inadequate flux.

(1)   Hoyle (1965) suggested Compton scattering of 3 degK black body radiation by relativistic galactic electrons. Felten and Morrison, using a galactic electron spectrum derived from low frequency radio measurements showed that the intensity was two orders of magnitude below that observed, though the spectral shape could be accurately predicted (see also Maraschi et al, 1968). Hamilton and Francey (1969), using improved radio data and new halo magnetic field estimates, show that galactic electrons can

produce diffuse X-ray intensities near the observed ones,
and point to a striking resemblance in the available diffuse
radio and X-ray spectral indices. In Chapter 7 further
similarities are illustrated. On the other hand the X-ray
isotropy appears to rule out a predominant galactic
contribution.

(2)   Shivanandan et al (1968), Houck and Harwit (1969)
report a large submillimeter background flux consistent with
a 8.3 degK black body radiation (presumably of galactic or
more local origin*). O'Connell and Verma (1969) show that
scattering of black body radiation of this temperature by
galactic electrons would produce the observed X-ray
intensity but imply a large anisotropy. Bortolot et al
(1969) cast doubt on the continuum nature of the submillimeter
radiation and Cowsik and Pal (1969), using the measured
energy densities predict a negligible halo but appreciable
disc X-ray component, compatible with measured disc
emissions, 2 - 5 keV (Cooke et al, 1969) and 100MeV (Clark
et al, 1968).

(3)   Wide extrapolations of the low energy and high energy
ends of the measured extrasolar electron spectrum are used
by Maraschi et al (1968) and Verma (1968) to produce
galactic X-rays by bremsstrahlung and synchrotron radiation
respectively. Neither can explain the observed X-ray

*Note: See Wagoner (1969). If the radiation has an
extragalactic component it will also contribute Compton
scattered X-rays in the presence of an extragalactic electron
spectrum.

spectrum and nor can galactic supra thermal proton

bremsstrahlung (Boldt and Selemitsos, 1969). Stecker et al

(1968) considers the small gamma ray component from π^{o} decay

resulting from cosmic ray collisions in the galaxy.

(4)   Bunner et al (1969), suggest a contribution from

unresolved population II objects.

1.7 SOURCE NOMENCLATURE

Poor angular resolution and possibly source

variability have led to considerable confusion in the naming

of sources. The early and more prolific source discoverers

each used individual systems, e.g.

Group	Example
Naval Research Laboratories (NRL)	Sco XR-1
American Science and Engineering (ASE)	Sco X-1
Massachussetts Institute of Technology (MIT)	
Lockheed Missiles and Space Company	L 11
ASE	GX 1^{II}
MIT	GX 1^{II} b^{II}

$(1^{II}, b^{II}$ new galactic coordinates$)$.

The UAT and Livermore Research Laboratories (LRL) groups

have used the XR notation and others the X notation, in

fact these two are freely used in the literature in

reference to the same object in the case of the stronger
sources.

The GX l^{II} b^{II} notation can only be used when accurate
source positions are known, otherwise some notation
characteristic of the discovering group is probably
preferable.   In the case of the dramatic variables Cen XR-2,
Cen XR-4 it is suggested that some indication of the time of
observation be included.   The time scale of the events to
date indicates that for example Cen XR-2 (Apr.67) and
Cen XR-4 (Jul.69) might be adequate.   A reason for this
suggestion is apparent in Chapter 6.

CHAPTER TWO

THE SKYLARK VEHICLE

2.1 GENERAL DESCRIPTION

Skylark is an unguided rocket developed primarily as a research vehicle for upper atmosphere studies. It is powered by a solid propellant Raven motor, which may be boosted by other solid propellant motors, Cuckoo or Goldfinch, as required. It is normally fin or spin stabilized, (attitude control was not available for UAT experiments).

The space available for experimental purposes consists of several stacked cylinders or "rings", of internal diameter 38 cm, surmounted by a nose cone of normal total angle 15°. Standard instrumentation includes trajectory and attitude determining devices and telemetry senders to enable the vehicle behaviour and experimental results to be continuously monitored. Typical Raven-Cuckoo combinations lift a head weight of 200 Kg (of which 90 Kg is standard instrumentation) to about 200 Km, allowing 300 seconds of X-ray observation time above 80 Km. Higher performance figures are quoted for the Goldfinch booster. Parachute recovery of the head is sometimes available.

The overall choice of site and facilities available to the experimenter is governed to some considerable extent by the classification of the experiment as a prime or ancillary one. Integration of experiments into the rocket is normally carried out at BAC (UK) before shipment to the launcher at Woomera ($137^{O}E$, $-31.5^{O}S$). Two of the six rockets discussed in this thesis were "engineering vehicles", with refurbished components assembled at W.R.E., Salisbury, S. Aust., and flown to test new flight systems, motors, etc. This has implications on the overall reliability.

Orientation in the rocket is with reference to orthogonal rocket axes $\pm$ OX, $\pm$ OY, $\pm$ OZ with + OX representing the longitudinal axis of symmetry of the rocket, looking towards the nose cone.

2.2   EXPERIMENT SITES IN THE ROCKET

The UAT experiments have been conducted from two general situations; those in which an X-ray counter has been directly exposed to the environment through an aperture in the rocket wall, and those providing a protecting cover which is ejected as the rocket emerges from the atmosphere.

2.2.1 "Exposed" Sites

On the four occasions, in which detector windows were exposed during launch, a complete UAT experiment (counters and associated electronics) rode in a single standard parallel section or ring of height 20.3 cm and average wall thickness 0.5 cm.   The walls were constructed from a magnesium alloy.

Flights I and II each carried a <u>multipurpose forward ring</u> (MR).   Four rectangular slots (3 cm x 7.2 cm) milled in two 2.5 cm build ups on the walls at $\pm$ 0Z, provided apertures for two pairs of X-ray counters.   The counters were pressure sealed over the apertures, and the associated electronics bolted to a pressure bulkhead which formed a floor to the ring.

In Flights III and IV a <u>base ring</u> (BR) was employed. Two rectangular apertures (8.5 cm x 10 cm), normally used for umbilical connectors, and a battery tray aperture (8 x 12 cm) were adapted for use as X-ray apertures. Counters and electronics were mounted as above.

2.2.2 "Protected" Sites

Large areas of thin plastic have been used as counter windows to attain maximum sensitivity to weak X-ray sources. Such windows require protection from aerodynamic heating encountered during passage through the atmosphere.   Both

ejectable nose cones and parallel sections with throw-off
doors have been employed for this purpose.

A type 2 nose cone (NC) is a stainless steel cone of
wall thickness 1/16 inches, split longitudinally into halves,
which are separated and ejected at about 80 Km by an
electronically initiated pneumatic system. A three tiered
pyramid of six counters filled the available space beneath
such a cone in flight IV; the associated electronics were
mounted in a multipurpose ring immediately below the nose
cone, and above the base ring described in (2.1.1).

A type 3 nose cone (NC), differing from the type 2 in
that it has a 30 cm parallel section at the base, protects
two large counters in flight V. A third counter in this
flight is housed in a type 8 parallel body section (T8), of
height 33.5 cm and wall thickness 0.5 cm. The type 8 "bay"
has an ejectable hatch on its circumference, disclosing an
aperture 22.8 cm by 23.3 cm, rounded at the corners by a
2.5 cm fillet radius. The construction is again of magnesium
alloy. In this case the T8 counter, its electronics, and
the NC detector electronics are all mounted on a bulkhead in
the T8 bay. Two T8 experiments, similar to that above, will
fly one above the other, on flight VI.

2.3   TELEMETRY

The Skylark telemetry sender uses an F.M./A.M. system
with Time Division Multiplexing to give 24 channels.   One
channel is occupied by a synchronisation pulse (not
generally available to the experimenter for timing purposes).
Each channel is sampled 80 times per second, and as many as
18 of the channels can be synchronously subswitched to give
quarter channels, sampled 20 times per second; on the other
hand, higher sampling rates can be achieved by super-
commutating data onto a number of suitably spaced channels.
Standard instrumentation and calibrations normally occupy
6-10 channels and in some cases additional senders can be
included if required.   A sender typically transmits 6-8
watts peak power at around 450 MHz, with sub-carrier
frequencies in the range 130-180 kHz.

A sender accepts analogue voltage inputs in the range
-3 volts to +3 volts, and the signal source must be
protected against exceeding these limits.   An input
impedance of 3 Megohms is presented to the signal source.
The frequency stability of the overall system is such that
signal source voltages can be identified to within about
120 millivolts, so that, for example, each sample can carry
a seven bit binary word.

2.4   TRAJECTORY AND ATTITUDE

This section describes the standard instrumentation
which is used to determine the rocket motion. The general
method of employing the data from these to obtain the
"direction of look" of the X-ray detectors at any instant,
is included.

2.4.1   Trajectory

Initial trajectories are predicted from motor
combination, head weight and possible launch angle. Actual
velocity and position data are obtained using a Doppler
transponder in the rocket (which receives a 104 MHz signal
from ground and re-emits it at 208 MHz); optical tracking,
and radar tracking of a 6 cm Missile Tracking System (M.T.S.)
beacon on the rocket, provide azimuth and elevation angles
during the early part of a flight. An accurate (to $\pm$ 0.1 Km
if necessary) post flight trajectory is normally provided by
W.R.E.

The attitude of the rocket co-ordinate system in space
is determined at every instant by reference to four types of
attitude sensor.

2.4.2 Accelerometers

Three accelerometers are mounted parallel to the three rocket axes, and are calibrated such that full scale telemetry deflections due to the OX accelerometer correspond to accelerations of -3g and +15g. OY and OZ accelerometers were monitored in the range -1.8g to +1.8g for flights I to III; in flights V and VI a $\pm$ 5.6g range will be used.

2.4.3 Rate Gyroscopes

Two orthogonal rate gyroscopes are included. In a normal stable free flight motion (see section 2.4.6) a spin about the OX axis and the precession of this axis about a cone are measured. The "spin" or "p-gyro" telemetry output is calibrated in the range $\pm$ 200° sec^{-1} for a despun rocket, and $\pm$ 1800° sec^{-1} in the spun-up case (table 2.1, below). A deflection in the positive direction (0 to +3 volts) indicates an anticlockwise rotation (looking forwards along OX). The "pitch" or "q-gyro" measures the rotation about the OY axis and is calibrated in the range $\pm$ 20 degrees/per second. A positive telemetry indication (0 to +3v) indicates a rotation of +OX towards +OZ.

2.4.4 Magnetometers

Three flux-gate magnetometers measure the components of the earth's magnetic field along the three rocket axes in

the range 0.7 to -0.7 oersteds; a trace above the zero level
on the telemetry record indicating a positive component of
the geomagnetic field in the positive direction of the
respective rocket axis. Ground level calibrations of the
magnetometers are of limited value since the magnetization
of the rocket changes significantly, as the rocket leaves the
launcher, as the boost motor separates, and possibly also as
the main motor case heats up in the atmosphere. Above about
70 km there should be no change in the magnetization.

2.4.5 Sun Slits

Four "sun-cells" (or "moon-cells") are located at the
+OY, -OY, +OZ and -OZ axes of a forward ring. Each cell has
a pair of crossed slits (of width 20 min. of arc) and each
slit is backed by a photo sensitive element which gives a
uniquely identifiable telemetry indication when irradiated
by the sun. The "vertical slit" is parallel to the OX axis
and will detect the sun at angles of up to $\pm$ 67 degrees from
the equatorial (YZ) plane of the rocket; the second slit is
at an angle of 45° to the vertical and its response is
restricted to angles of $\pm$ 40° from the YZ plane.

2.4.6 Attitude Solution Methods

The accelerometers measure the booster thrust from 0
to +5 seconds and the Raven thrust from about +7 seconds to

+50 seconds. After this time the rocket motion with respect

to its centre of mass is normally uninfluenced by external

forces until re-entry (about +400 seconds), with no

accelerometer response. The motion of a rigid body in a

force free field has been well studied (e.g. Symon, 1960)

and results in a rocket motion consisting of a spin about

the minor axis of inertia accompanied by a precession (in

the same sense) of the spin axis about the pitch or

precession axis, which is fixed in space and parallel to

the total angular momentum. The half angle of the precession

cone ρ, is related to the spin rate (ω_s) and precession rate

(ω_p) by

$$\cos \rho \quad = \quad K_i \; \omega_s/\omega_p \qquad\qquad (2.1)$$

where K_i is a constant depending on the moments of inertia

of the rocket.

The Skylark is subject to "lock in", and at a critical

roll rate (about 1 rev/sec) can fail structurally due to a

roll-yaw resonance. The fins of the motor are canted to

give roll rates either well below (about 0.1 rev/sec), or

well above (about 3 rev/sec), the critical rate. Table (2.1)

gives typical flight parameters representing both types of

motion.

TABLE 2.1

TYPICAL SKYLARK FREE FLIGHT PARAMETERS

	despun	spun up
spin rate, ω_s	36° sec^{-1}	1080° sec^{-1}
precession rate, ω_p	1° sec^{-1}	15° sec^{-1}
precession cone half angle, ρ	60°	5°

(flight duration > 80 km, approx. 300 secs)

A preliminary method used to obtain the rocket orientation in space at every instant is discussed in some detail by Harries (1968) and is summarized briefly here. The angle between the OX axis and a fixed direction in space OC is given by
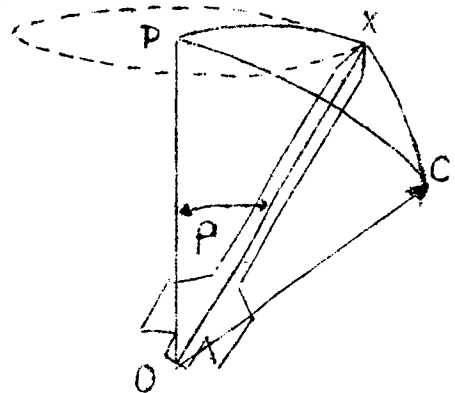
$$\cos \widehat{XOC} = A + B \cos (\omega_p t + \varphi) \qquad (2.2)$$

where the constants A, B are simply related to ρ and the angle POC, between OC and the precession axis OP.

In the case of the magnetometers, the X magnetometer output is of the form $M \cos \widehat{XOM}$, where M is the geomagnetic field strength, and with maxima and minima determined by ρ and $\widehat{POM}$ as in equation (2.2). The Y and Z magnetometers

also vary sinusoidally as the rocket spins; all three vary

with respect to zero levels determined by the unknown

permanent magnetism of the rocket. By choosing evaluation

points at for example $M_{y\ max}$, then M_z is at the zero level

and since

$$M_x{}^2 + M_y{}^2 + M_z{}^2 = M^2,$$

$$M_{y\ max} = \pm M \sin X\hat{O}M.$$

The use of peak to peak value eliminates the unknown d.c.

component. Two other effects must be accounted for. The

first, induced magnetism in the rocket due to heating etc.,

acts like a change in sensitivity and can be largely

eliminated by inflight calibration at selected points, e.g.

when $X\hat{O}M = 90°$. The second is due to a variation with

altitude (h) in the geomagnetic field. At Woomera

$$\sin X\hat{O}M = \frac{M_{y\ max}}{M_0(1-4.97_{10}-4.h)}$$

where M_0 is the sea level intensity.

The angle $S\hat{O}X$ between the sun position and the OX axis

can be determined at times on a spin when both the vertical

and diagonal slits of a cell see the sun. The time

difference ΔT, over the time between two successive sightings

by the vertical slit, T, is related to $S\hat{O}X$ by

$$\cot S\hat{O}X = \sin (360\ \Delta T/T) \tag{2.4}$$

provided $S\hat{O}X$ changes monotonically over T (normally, a good

approximation).

A celestial globe, marked at the sun and magnetic field positions, can now be used to find positions for +OX at the points of intersection of arcs corresponding to $\hat{SOX}$ and $\hat{MOX}$ at each instant for which both are evaluated. The ambiguity as to which of the two possible intersections corresponds to the true +OX position is resolved by the order of sighting the sun and the magnetic field (knowing the spin direction from the rate gyroscopes).

Thus for a rocket motion which has a circular precession cone and constant ω_p, the evaluated OX positions lie on a circle on the celestial globe, i.e. completion of the circle gives the position of the OX axis in celestial co-ordinates at every instant of free flight.

The intersection of the OYZ plane with the celestial sphere is now readily calculated at each instant. The phasing of the OY and OZ axes is related to sun sightings using the vertical sunslits (again knowing the spin direction).

The above is a greatly simplified approach and there are a number of factors which impose modifications. For example, inertial asymmetries can cause significant departures from the ideal motion (roll rate modulation, spin axis "wobble"), or air leaks from the sealed head can alter the precession rate. The solution can be complicated by inadequate sun sightings during the flight. A more

rigorous method, involving a least square's fitting

technique to the magnetometer and sun cell data, is

described by Herbert (1967) and is carried out by the

British Aircraft Corporation (Bristol, U.K.) for Skylark

flights.

A valuable check on attitude solutions is provided

by the collimated X-ray detectors when they sight strong

sources of known position (e.g. the sun, Sco XR-1, Tau XR-1).

2.5   ELECTRICAL POWER

The main inflight power source is a battery of silver-

zinc cells mounted on a removable tray in a base ring. One

battery supplies all of the standard instrumentation plus

some experimental equipment, a second supplies the bulk of

the experimental equipment, plus vehicle services such as

nose cone and hatch jettison or head release. Under normal

load conditions of 10 to 15 amperes, the voltage of each

battery will vary between 32 and 26 volts D.C. during a

flight. Under light load conditions the voltage can be as

high as 37 volts D.C.

2.6   GROUND FACILITIES

The ground _priming unit_ is essential to the preparation

and testing of Skylark. It supplies and controls electrical

power to the head, controls operations within the head,

verifies their correct functioning, and monitors voltages

and currents at various other points throughout the rocket.

Connection is made to the rocket via cables which connect to

a base ring through two pairs of 24 way butting connectors.

The connectors are removed by hand in the laboratory, or by

ejector arms in the launcher. The priming cables are long

(19 feet in the laboratory and 550 feet at the launcher) and

unscreened.

A separate control and monitoring panel on the priming

unit is allocated to each experiment (or D.C. converter). A

nominal 26 volts D.C. is switched to the converter in the

experiment bay by a 10 amp cut-out, the current being

indicated by a 0-10 amp meter and the supply voltage at the

round by a 0-40 volt meter. Two D.C., 0-100 microamp

meters of 1600 ohms resistance, each with six way input

selector switches, are provided to measure voltages and

currents in the experiment. A number of 10 amp double pole

switches (service ways) are provided for miscellaneous

purposes, and each is accompanied by an indicator lamp wired

to show either the switch has closed or the required

operation in the round has occurred. These have been

utilized to operate electro-mechanical (Ledex) switches which

expose counters to calibrating radiation in flight.

2.7   ENVIRONMENTAL CONDITIONS AND TESTS

The range head at Woomera experiences extremes in weather which can influence proportional counter behaviour. The experiment must also be capable of surviving the acceleration and vibration of launch, aerodynamic heating during passage through the atmosphere and pressure differentials (both from mechanical and electrical viewpoints) as the rocket leaves the atmosphere. The ejection of protecting covers, above the atmosphere can be hazardous. In some circumstances, essential ground tests aimed at reproducing the rocket environment produce stresses not normally encountered during flight.

2.7.1   Launcher Environment

Final integration, involving the setting and locking of amplifier gains, bias levels and supply voltages etc., takes place in air conditioned workshops (constant $20^{\circ}C$). However, the time between leaving the workshops and launch can be long, as much as weeks in cases where a main experiment has a tight restriction on launch time (e.g. requiring a time of particular magnetic disturbance). The launcher experiences temperature extremes of $0^{\circ}C$ at night in winter to approaching $50^{\circ}C$ on summer days. The gain of a given proportional counter, flushed and sealed with gas at an ambient temperature of $50^{\circ}C$ is $\sim 100\%$

higher than when flushed and sealed with gas at the
temperature of the workshop environment simply as a result
of fewer gas atoms in the counter, (described in terms of a
lower pressure in table 3.1, next chapter). To avoid
invalidation of bias level settings in such counters care
must be taken to ensure that gas cylinders used for counter
flushing are kept at a relatively constant temperature and/or
amplifier gains are easily adjustable.

Summer thunder storms at Woomera can produce
conditions of high relative humidity (a value in excess of
90% occurring during UAT flight IV preparations). Counters
with large area thin plastic windows and using epoxy resins
in construction are susceptible to gas contamination by
water vapour with a consequent gain and energy resolution
deterioration. If such unusual humidity conditions occur
when these counters are in the launcher, some form of
dessication or protection may be necessary.

2.7.2 Vibration and Acceleration

During the motor thrust phases the Skylark is subjected
to sustained acceleration and vibration. In a typical
Raven-Cuckoo combination expected accelerations are 10g and
1g in the longitudinal and lateral directions respectively.
(For a Raven-Goldfinch combination the figures approach 15g
and 2g, respectively). Resonances at about 400 c/s are

particularly destructive, this frequency being associated
with the passage of the vehicle up the launcher.

Normal practices of locking screws, nuts and
potentiometer controls, anchoring cables, conformally
coating electronic components etc., are followed. Payloads
are vibration tested by subjecting them to sinusoidal
vibrations of accelerations 6g longitudinally and 2g
laterally, while the vibration frequency is slowly swept
from 20 Hz to 2000 Hz. Probes are used to search for and
measure resonance gains. This has been found to be
adequate for Skylark trials.

If recovery of the payload is required, it must
withstand impact at velocities of 30 Km/hr. with a
parachute. Impact velocities of 200 Km/hr. are experienced
after free fall.

2.7.3 Aerodynamic Heating

At the time of launch of the first UAT flights, it
was anticipated that the skin temperature of the parallel
sections could rise up to $200^{\circ}C$ and the nose cone up to
about $700^{\circ}C$ due to aerodynamic heating during the 50 seconds
or so to pass out of the atmosphere. The brevity of the
heating plus the large thermal capacity of the rocket
indicated that temperatures of components mounted away from
the walls in the parallel sections would alter slightly and

slowly. This behaviour was confirmed in flights I and II, in both of which four thermistors were mounted against the inside wall and throughout the electronics package. The inside wall thermistors increased from $25^\circ C$ to $65^\circ C$ at 100 seconds and remained relatively constant around $70^\circ C$ until re-entry. Most other thermistors increased slowly and steadily from $25^\circ C$ at launch to $30^\circ C$ at re-entry ($\sim$400 secs.). (In the power converter, which generated a considerable amount of heat, there was a corresponding steady rise from $35^\circ C$ to $44^\circ C$).

Detailed findings are reported by Anderson and Fike (1969), for a similar rocket, the Aerobee 150. Outside skin temperatures reached a maximum at 50 to 100 seconds. The maximum temperature of about $150^\circ C$ was found to vary markedly from flight to flight (by as much as $60^\circ C$) and similar variations were observed on any one rocket, around its circumference. The experimental package, a cylinder 5/16" from the skin, showed a rapid temperature increase from $25^\circ C$, levelling out at $30^\circ C$ after 150 seconds. (This difference from Skylark is interpreted as being partly a result of the smaller heat capacity of the Aerobee). Anderson and Fike eliminate conduction as a source of heat transfer by using insulated experiment mounts, and calculate that radiative transfer accounts for less than $1^\circ C$ of the rise. Forced convection is neglected since the experiment

was well removed from venting holes, and free convection was

shown to be unlikely. This leaves conduction through the

air as the principal heat transfer mechanism. Since air

conductivity is independent of pressure (for molecule mean

free paths $\ll$ the conduction path) air conduction remained

high despite 15 half inch venting holes in the nose cone, and

in fact continued to be appreciable throughout the flight

(for pressures $\sim 10^{-2}$ torr) even after nose cone ejection

(presumed by Anderson and Fike to be due to out gassing).

For large UAT plastic window counters under a split

nose cone, radiative cooling in, and suppression of

convection by the counter collimators are the main means of

protection against the high skin temperatures, and forced

convection due to venting and nose cone ejection respectively.

On most flights the inside surface of the nose cones can be

lagged. Similar forced convection problems arise in the

type-8 bays. The effectiveness of the collimator as an all

purpose protection for the window is indicated from the

results of UAT flight III in which a plastic window counter

was flown in an exposed site (see section 5.3).

2.7.4 Pressure

The standard instrument section of the head is sealed

by pressure bulkheads fore and aft so that it contains air at

ground level pressure during flight. This is to prevent

electrical corona at high altitudes. The sealing bulkheads are mechanically deformed (as much as 0.4 cm at their centre) with one atmosphere differential.

In the "exposed" sites of 2.2.1 the UAT ring has formed part of the sealed head section, requiring the detector to be sealed over the ring aperture such that with the atmosphere differential in flight, the leak rate is less than 1 lb./sq.in/hr. The normal method of leak testing on ground is to pressurize the head to two atmospheres —— thus since the counter gas remains at one atmosphere the counter walls have to withstand this compressive differential. In order to maintain a high "volume to leakage" ratio throughout flight, the UAT bulkheads common to adjoining sealed rings must be well vented.

The "protected" sites of 2.2.2 are vented and remain reasonably close to ambient pressure throughout the flight (e.g. Anderson and Fike). Two alternative means of preventing corona exist; one is to leave connections exposed and switch on E.H.T. above the atmosphere where corona no longer occurs; the second is to seal all E.H.T. connections so that they remain at ground level pressure throughout. The latter course was chosen in these flights to allow counter calibration during ascent, and can be achieved using potting compounds and plumbing for E.H.T. wires. The counter walls must be capable of containing the gas at one atmosphere in a

vacuum environment, which for the large light-weight
counters used in these sites, often demands external
reinforcing.

Of course in all sites, the thin counter windows have
to withstand an atmosphere differential (i.e. 15 lb/sq.in.
over up to 100 sq.in.). Window support in UAT counters has
been provided by the collimators.

2.7.5 Ejection of Covers

As has already been mentioned, nose cone and door
ejection at about 70 Km is accompanied by forced convection
as a result of a sharp drop in pressure (typically from about
.5 to .05 torr, according to Anderson and Fike). A more
serious problem has occurred with nose cone ejection from
spun up rounds. In such a case, nose cone experiments must
be adequately protected against mechanical damage from
collision with a nose cone half which fails to separate
cleanly.

2.8   LAUNCH SEQUENCE

A typical launch sequence is as follows

Time (secs)	Altitude (Km)	
-3600		X-ray experiment ON (ground supplies). Calibrate counters, rejuvenate if necessary.
-1800		Finish calibration of X-ray experiment. All equipment ON (ground supplies), commence check out.
-1200		Telemetry recording run (2 min), counters calibrated.
-40		Start rocket programme motor (subsequently initiates all events e.g. launch, ledex pulse, nose cone eject, etc).
-30		Switch to internal supplies.
-20		Extract priming unit connectors. (a "snatch" plug remains connected until launch; in the event of missfire, internal supplies can be shut off).
ZERO	0	Cuckoo ignite.
+4	4	Boost burn out.
+6	6	Raven ignite.
+30	30	Raven burn out (X-ray ledex calibration ON).
+70	70	Nose cone and hatch release (X-ray ledex OFF).
+250	200	Apogee
+430	70	Re-entry (X-ray ledex ON) Motor-head separation.
+620	0	Head impact (with no parachute).

2.9   FLIGHT RECORDS

The telemetry from the rocket sender is received on the ground and decommutated into the 24 channels. Up to five channels can be displayed on a cathode ray <u>tube</u>, each channel display consisting of a series of dots separated by 1/80 second. All tubes display a channel containing a 0%, 40% and 100% of F.S.D. plus a +2.68 volt reference (Mallory cell) to calibrate the record.

The tube displays are photographed and two types of record produced. For flights I, II and III "quick-look" records, 24 inches long and containing all results for the whole flight gave a ready overall reference. High speed (2 inches/sec.) records of a selected tube were available for analysis, allowing resolution of individual telemetry samples. Flights V and VI records will consist of high and low speed photographic records (in this case 2 inch and 1/8 inch per second respectively) plus a magnetic tape direct from the receiver). The latter will be used to produce a digital output from a W.R.E. analogue to digital converter.

THE DETECTION OF COSMIC X-RAYS USING

PROPORTIONAL COUNTERS

3.1 THE PROPORTIONAL COUNTER

In what has been called the "ancient art of proportional
counting", the general principles involved are understood, and
relatively straight-forward methods of successful counter
construction and operation have evolved, e.g. see Curran and
Craggs (1949), Wilkinson (1950), West (1953) and Franzen and
Cochran (1962).

It is convenient to describe the proportional counter
action under the following headings

(1)   absorption of the incident radiation,

(2)   initial ionization of the counter gas,

(3)   "low field" drifts of the electrons and positive ions,

(4)   gas multiplication due to ionizing collisions by the
electrons in "high field" regions near the anode, and

(5)   pulse formation on the anode.

Largely as a result of the complex nature of the ionizing
processes, the simpler proportional counter theories are little
more than descriptions of the available data, and the more
complex theories are unwieldy and applicable to only the simpler

gases. Thus in the discussion of steps (1) to (5) in following
sub-sections only those data of particular significance to the
present application are referenced, along with useful
approximate design relations. (This includes recent information
not available at the original UAT design stage).

The basic features of a UAT counter (with typical
dimensions) are the long (15-40 cm), rectangular (5 x 5 cm),
conducting box or cathode, surrounding a thin anode wire
(3.5, 0 -3 cm radius), centrally mounted and at high positive
potential (2400 volts). One side of the box is replaced with
a conducting window, thick enough to form a gas tight barrier
under the environmental conditions of a rocket flight and thin
enough to efficiently transmit the low energy X-rays (>1.5keV).
The sensitive volume of the counter, between anode and cathode,
is filled with a gas (normally P-10, a commercially available
90% argon - 10% methane mixture, at one atmosphere) which is
isolated from the environment. Among the necessary gas
properties are its ability to efficiently absorb the radiation
of interest (<15keV), and under the influence of the electric
field, to produce a final number of ion pairs proportional to
the energy of an incident parent photon. In practice, large
areas are attained using multi-anode counters, in which a number
of the boxes or units are placed side by side, with a common gas
volume and paralleled anodes.

3.1.1 Absorption of the Incident Radiation

The counter commences operation in the desired manner when a photon from an X-ray source traverses the intervening medium and window and deposits its entire energy in the counter gas. At the energies 1.5 to 15 keV the interaction is by the <u>photo-electric effect</u>, involving the total absorption of the photon by an electron bound in an atom. The most tightly bound atomic electrons have the greatest probability of absorbing a photon of energy $h\nu$ greater than B, the binding energy, and the atomic cross section for absorption is described very approximately by

$$\tau_a \; \simeq \; K \; Z^4 (h\nu)^{-3} \quad (cm^2 \; atom^{-1}) \qquad\qquad (3.1)$$

Here K changes discontinuously at absorption edges corresponding to the electron binding energies in an absorber of atomic number Z.

Henke et al (1967) have recently produced tabulations of <u>mass absorption coefficients</u>, μ, where

$$\mu \quad = \tau_a \; N/A \quad (cm^2 \; gm^{-1}) \qquad\qquad (3.1a)$$

(N = Avogadro's number = $6.023_{,0} \; 23$ and A = atomic weight). The tabulations are for elements with $Z < 19$, and compounds comprising these elements, and are a result of an interpolation between experimental points of their own plus those from a comprehensive list of previous authors, weighted according to the consistency and amount of data available. This process, according to Henke et al, "permits prediction .... with considerably more precision than can be obtained with present

theory." At the same time it is worth noting that the predicted

values for argon differ by up to almost 20% from the recent data

of Bearden (1966), in the 2-200$\overset{\circ}{A}$ wavelength range considered.

The Henke et al data have been used here, supplemented at

higher energies and for heavier elements (where overlapping

data are in good agreement), by those of Victoreen (1949) and

Allen (1935). These coefficients are related to the percentage

transmission of a beam, I_0, of X-rays through x gm cm^{-2} of

absorber by

$$I/I_0 = \exp(-\mu x) \tag{3.2}$$

The electron which absorbs the photon, the photo-electron,

is ejected with energy

$$T = h\nu - B \tag{3.3}$$

with the remainder of the photon energy exciting the parent

atom. De-excitation is by a series of rearrangement processes

to fill the inner shell vacancy and can become very complicated.

For example a K shell vacancy is filled in about 10^{-17} to 10^{-14}

seconds by an electron from an L sub-shell or higher shell, and

the difference in binding energy between the two shells is

released as a K X-ray, or is transferred to another bound

electron which is ejected and is called an Auger electron. The

vacancy or vacancies that exist after this step are filled by

similar processes, which continue, with the emission of L, M,

N, etc. X-rays and Auger electrons, until a highly charged

positive ion (i.e. with a number of outer shell vacancies),

remains. These processes are reviewed extensively by Fink et
al (1966), who list the _fluorescent yield_, f, (the probability
of a radiative transition to fill a particular inner shell
vacancy) for all gas atoms and shells of interest here; as a
guide, the fluorescent yield for K and L transitions is given
approximately by

$$f_i \; \simeq \; (1 + c_i/Z^4)^{-1} \hspace{3cm} (3.4)$$

where $c_K \simeq 10^6$ and $c_L \simeq 6_{,0} 7$.   The probability of a
fluorescent X-ray (for which the parent gas is relatively
optically thin) escaping the counter with part of the original
photon energy, can in practice be made small by choice of gas
and by geometrical design, else suitable correction must be made
to the measured spectra —— this is the _escape peak_ phenomenon
discussed later.

3.1.2 Initial Ionization of the Counter Gas

The electrons released by a photon absorbing atom are
rapidly reabsorbed. For example a 10keV electron is absorbed
by argon at N.T.P. in about 2mm (Berger and Seltzer 1964);
argon L X-rays will be absorbed in a similar distance, whereas
the absorption length (when $\mu x = 1$) for the K X-rays is about
3 cm. Many of the liberated electrons have sufficient energy
to ionize the surrounding gas and "secondary" ionization
continues for about 10^{-7} seconds until the energy of ejected
electrons falls below the ionization potential, I, of the gas.

Part of the energy lost by these electrons goes into processes other than ionization, so that the <u>average energy to create an ion pair</u>, W, is always greater than I.

W has been investigated experimentally for a variety of common gases and a few gas mixtures using a number of ionizing techniques; the results can be summarized as follows —— the values of W (typically 30 eV) are not simply related to I (typically 15 eV) and vary only moderately with the type of atom. The variation is even less with the type and energy (particularly in noble gases) of the ionizing particle. On the other hand trace impurities with suitably low ionization potentials can cause marked increases in ionization (due to collisions between impurity atoms or molecules and excited but un-ionized gas atoms with consequent ionization), with a corresponding decrease in W. An extensive review of measurements, results and empirical data is given by Valentine and Curran (1958), and of particular interest are the data of Melton et al (1954), Jesse and Sadausksis (1955) and Alkazov et al (1967), for mixtures of noble gases with a variety of additives. In an argon-methane mixture W falls from 26.5 eV for 100% argon, to a minimum of 26.0eV with 5% CH_4, rising slowly through 26.3eV at 10% CH_4 to 29 eV at 100% methane. (Acetylene, unusual in that it has an ionization potential below the 11.5 eV metastable state of argon, produces the most marked effect of the additives used by the above authors. W falls to a minimum 20.5 eV with 0.5%

acetylene, is only 22 eV at 10% C_2H_2 and 27 eV at 100% C_2H_2.)

The actual number of ion pairs formed, J, is subject to statistical fluctuations, first studied by Fano (1947) who obtained a variance, σ_J^2, of J for a fixed energy of ionizing particle in the form

$$\sigma_J^2 \; = \; F \ddot{J} \tag{3.5}$$

where $\bar{J} = h\nu/W$, and F is the Fano factor. For hydrogen Fano showed $1/3 \lessgtr F \lessgtr 1/2$ (compared to $F = 1$ for a Poisson distribution). In noble gases, the magnitude of the ionization fluctuations is mainly determined by redistributions of the numbers N_i, N_{ex}, of ionized and excited atoms formed, rather than energy loss variation in ionization and excitation. As seen above, the addition of small amounts of molecular gases results in a total number of ion pairs, J, much closer to $N_i + N_{ex}$ than in their absence, with a corresponding decrease in F. Alkhazov et al measure values of F in Ar – 0.8% CH_4, and Ar – 0.5% C_2H_2 at 0.19, 0.09 respectively, in reasonable agreement with their updated version of Fano's theory. These values can be compared with $F \sim 0.2$ for pure argon, and also for P-10.

3.1.3 "Low Field" Drifts of Electrons and Ions

The electrons and ions resulting from the initial ionizing event begin drifting toward anode and cathode respectively under the influence of the counter electrostatic field. The drift is

superposed on a thermal motion determined by the neutral gas
temperature. Energy is gained from the field, and lost in
collisions with gas atoms and/or molecules, so that the ratio of
field strength to gas pressure, X/p, is often used as the
parameter determining the drift velocity, (as well as influencing
the gas multiplication as discussed in the next sub-section).

The field in a counter with anode of radius a, at voltage
V_a, and with a cylindrical cathode of radius b, is given as a
function of radius by

$$X(r) \quad = \quad \frac{V_a}{r \ln(b/a)} \qquad\qquad (3.6)$$

With p = 760 torr, X/p then ranges from about

(130 volts cm^{-1} $torr^{-1}$ at the anode, to
(
(0.16 volts cm^{-1} $torr^{-1}$ at the cathode,

For example, X/p falls to a tenth the anode value in about
1/100th the cathode radius, emphasizing the relative
insensitivity of counter properties determined by X/p on the
actual cathode shape and the position of the original ionizing
event. This concentric cylinder approximation suffices for
most calculations and the "low field" region can be thought of
as occupying practically the total counter volume (excluding
only one to two anode radii where electrons are accelerated
sufficiently to make inelastic collisions).

In normal counter operation the electron drift across the
low field region takes place while the positive ions are
effectively stationary. The very slow ion drift rate,

$$\mathbf{v}_{ion} = \kappa\,(X/p) \qquad\qquad (3.7)$$

where the ion mobility, κ, depends on the nature of the gas and

the ion mass but is relatively independent of the ion charge.

The <u>electrons</u>, because of their small mass, accelerate

rapidly and lose little energy in elastic collisions. On the

other hand the probability for an elastic collision differs

greatly from gas to gas and is in general strongly dependent on

electron energy. Also the addition of impurity molecules to a

noble gas has the effect of decreasing the thermal agitation

energy (due to low energy inelastic collisions) with a

consequent increase in drift velocity. Measurements of

electron drift velocity as a function of X/p for a variety of

gases have been made by English and Hanna (1953) and Bortner

et al (1957). In strong fields $v_{electron}$ is described in a

similar fashion to v_{ion} in equation 3.7. In weaker fields a

$(X/p)^{\frac{1}{2}}$ dependence is applicable. (Typical values for P-10 at

$X/p = 1$ volt $cm^{-1} torr^{-1}$ are $v_{electron} = 4$ cm $(\mu\ sec)^{-1}$, compared

with $v_{ion} = .002$ cm $(\mu sec)^{-1}$).

3.1.4 Gas Multiplication

The accelerating electrons begin losing energy by

inelastic collisions; when the energy gained from the field in

a mean collision-free path exceeds the gas ionization potential,

ionization by electron impact results in a rapidly multiplying

electron avalanche. The <u>gas gain</u>, A, of the counter is defined

as the ratio of electrons collected at the anode to the number

produced in the initial ionizing event. This avalanche effect

is normally described in terms of the <u>first Townsend coefficient</u>,

α, the mean number of ion pairs formed by an electron per cm of

its path measured along the field (i.e. the reciprocal of the

mean free path for ionization) - a simple relationship between

α/p and X/p being assumed. In atomic gases, α can be markedly

decreased by traces of molecular impurities, in this case in

sympathy with the decrease in thermal agitation energy (and

thus increase in drift velocity) mentioned above.

Williams and Sara (1962), have measured the variation in

gas gain of a P-10 filled counter, with anode and cathode

radii, anode voltage and gas density, for a limited range of p

about 1 atmosphere. Two analytical expressions for the <u>mean</u>

<u>gas gain</u>, one due to Diethorn (1956), and differing only in the

assumed function α/p (X/p), were used to predict the behaviour,

which was found to agree with the data except at large anode

radii (low gas gains). Zastawny (1966) used a third function

α/p (X/p) obtained from measurements on CO_2, and obtained an

expression for $\bar{A}$ in the form,

$$\frac{\ln \bar{A}}{p \, a \, S_a} = K + B \left(\ln \frac{S_a}{S_0} + \frac{S_0}{S_a} - 1 \right) \qquad (3.8)$$

where, using (3.6),

$$S_a = (X/p)_a = V_a / (p \, a \, \ln(b/a)),$$

and K, B, S_0 are constants which can be determined by
successive graphical approximation. (S_0 represents X/p at the
commencement of multiplication in an idealized gas). Applying
(3.8) to the data of Williams and Sara at 712 torr., Zastawny
(1967) obtains excellent agreement for all radii using values
for P-10 of,

$$K = (0.5 \pm 0.1)_{10} -3 \quad \text{volt}^{-1} ;$$

$$B = (3.00 \pm .03)_{10} -2 \quad \text{volt}^{-1} ;$$

$$S_0 = (25 \pm 1) \text{ volt. cm}^{-1} \text{ torr}^{-1} \qquad (3.8a)$$

Zastawny considers the empirical α/p (X/p) relations used by
different authors, for example Zastawny, Diethorn, Rose and
Korff (1941), to successively approach the true situation with
increasing X/p.

A useful criterion for defining the range of
proportionality in Xe-CH_4, Ar-CH_4 counters for an energy
deposition of hν was obtained by Hanna et al (1949) in the form,

$$h\nu . \bar{A} \lesssim 10^8 \quad eV \qquad (3.9)$$

consistent with a total charge released in the avalanche
approaching the electrostatic charge per unit length in the
counter capacity, with consequent distortion of the field.
This is known as a _space charge_ effect, discussed in some
detail by Hendricks (1969).

The statistics of the multiplication process continues to
be the subject of many experimental and theoretical

investigations, e.g. Gold and Bennett (1966), Campbell and

Ledingham (1966), Cookson and Lewis (1966), Legler (1967)

Carver and Mitchell (1967), Campbell (1967), Charles and Cooke

(1969), Byrne (1969). The most common experimental study

involves the release of <u>single electrons</u> into a selected gas in

an electric field. The results in proportional counters with a

methane filling at low gas gains (Gold and Bennett) and with

argon mixtures over a range of gas gains (Campbell and

Ledingham) are consistent with a pulse height distribution of

the form,

$$f(z) \;=\; \exp(-z) \tag{3.10}$$

where z is proportional to A. At higher gas gains in methane

(Gold and Bennett), and in argon-methane according to the much

quoted results of Curran et al (1949), a peaked distribution

approximately of the form,

$$f(z) \;\simeq\; z^k \exp(-z) \tag{3.11}$$

is present. The methane results are in accord with observations

in this gas (and in N_2), for uniform electric fields, in which

there is a gradual trend from exponential to peaked

distributions with increasing X/p (e.g. Cookson and Lewis).

The most comprehensive data by this single electron

release method is that of Carver and Mitchell, who accurately

measure deviations from the exponential shape for a variety

of gases and mixtures (including P-10), and for a range of gas

gains. Their resulting distributions are described as follows:

(1)"at small pulse heights there may be a reduced
number of pulses compared with the exponential
distribution if the electron multiplication commences
in a region of low field strength"; (attributed to
variations in the electron ionizing efficiency,
represented by $k \sim (X/\alpha I)^{-1}$, at the commencement of
multiplication;

(2)"at large pulse heights there may be an excess of
pulses owing to the occurrence of secondary
successor avalanches initiated by photo-electric
effects".

The parameter describing (1), k, was found to be relatively
insensitive to the applied voltage, unlike that for (2),
which rapidly increased with increasing voltage. In the absence
of successor avalanches, the Carver-Mitchell equation reduces to
a form similar to (3.11), for which the relative variance is
given by

$$\left(\frac{\sigma_f}{f}\right)^2 \;=\; \left(\frac{\sigma_A}{A}\right)^2 \;\approx\; \frac{1}{1+k} \tag{3.11a}$$

(according to Byrne, the term $1/(1+k)$ can be interpreted as
the fraction of avalanche electrons with energies above a
threshold energy between two and three times the ionization
energy, when the number of electrons is large).

Information on the multiplication process can also be
gained by measuring the pulse distribution from a proportional

counter due to the absorption of <u>mono energetic photons</u> in the
gas, assuming a knowledge of W and F (section 3.1.2). The
distributions, for photon energies above about 2keV are well
described by a <u>Gaussian</u> shape, but below 2keV a distinct
asymmetry appears (Campbell and Ledingham). It is convenient
to measure the energy resolution of a detector in terms of the
<u>full width at half maximum</u> of the pulse distribution due to
photons of energy $h\nu$, expressed as a fraction of the mean pulse
height $\bar{P}$. For a Gaussian of standard deviation σ,

$$FWHM = 2.36 \; \sigma/\bar{P} \tag{3.12}$$

The relative variance $(\sigma_P/\bar{P})$ of the pulse distributions has
frequently been investigated over the range of proportionality,
a $(h\nu)^{-\frac{1}{2}}$ dependence being established (e.g. Charles and Cooke,
Campbell and Ledingham).

The very careful measurements of Charles and Cooke give

$$\sigma_P/\bar{P} = 0.15 \; (h\nu)^{-\frac{1}{2}} \tag{3.13}$$

as a possible best resolution (smallest variance) in a P-10
counter. This is in substantial agreement with previous
isolated measurements summarized by Mulvey and Campbell (1958),
and can be compared with theory (see equation 3.5), using
$F = 0.2$, and $W = 2.63_{10}-2$ keV, i.e.

$$(\sigma_J/\bar{J})^2 = 5.26_{10}-3 \; /h\nu. \tag{3.14a}$$

Assuming no interaction between the initial and avalanche
electrons,

$$(\frac{\sigma_P}{\bar{P}})^2 = (\frac{\sigma_J}{\bar{J}})^2 + \frac{W}{h\nu}(\frac{\sigma_A}{\bar{A}})^2, \tag{3.14b}$$

and thus the avalanche process has a relative variance

$$(\sigma_A/\bar{A})^2 \quad = \quad 0.68 \tag{3.14c}$$

Equation (3.14b) can be re-expressed in the form

$$(\frac{\sigma_P}{\bar{P}})^2 \quad = \frac{W}{h\nu} \quad (F + (\frac{\sigma_A}{\bar{A}})^2 \quad) \tag{3.15}$$

Thus in P-10, the avalanche process contributes about 75% of the overall variance.

As has been mentioned in section 3.1.2, the addition of traces of polyatomic gas to noble gases increases the ionizing efficiency (for molecular ionization potentials suitably small), thus decreasing W and F. In the absence of complicating factors such as successor avalanches, the factor k might be expected to decrease with the addition of molecules, in sympathy with the decrease in the mean electron energy, and therefore α, (the $k \sim \alpha I/X$ dependence is discussed in more detail by Byrne, 1969). Thus from 3.11a, $(\sigma_A/A)^2$ increases and tends to offset the improvement in resolution in going from a pure gas to a mixture, realized by the decrease in W and F.

It is instructive that no effect on resolution due to variations in ionizing efficiency has been observed in X-ray spectra observed with a given proportional counter (in accord with the relative insensitivity to applied voltage observed by Carver and Mitchell, and despite expectations to the contrary from the single electron results of Curran, and Gold and Bennett for argon-methane mixtures). Similarly, the sharp increase in photon induced avalanches at high voltages, evident

in the single electron results, are far less noticeable in the X-ray results because of the competing space charge effect (see equation 3.9). The real situation is apparently a complex one, involving a combination of these effects, and with the possibility of trace impurities in gases markedly influencing behaviour.

3.1.5 Pulse Formation on the Anode

Of the electrons collected at the anode, the majority are formed in the avalanche region very close to the wire and traverse only a small fraction of the potential across the counter. The pulse on the anode due to the electrons is therefore small compared with that due to positive ions formed in the avalanche and drifting through practically the whole counter potential. With a drift velocity given by equation (3.7) in a field described by (3.6), the ion collection time at the cathode is given by

$$T = \int_{r \simeq a}^{r = b} v_{ion}^{-1} \, dr \simeq \frac{b^2 p \, \ln(b/a)}{2 \kappa \, V_a} \qquad (3.15)$$

(for $b \gg a$). In a typical situation $T = 5m.sec.$, introducing serious dead time errors at moderate count rates if all ions must be collected.

The shape of the voltage pulse on the anode can be described by, (Franzen and Cochran, pge 66),

$$V(t) \simeq \frac{-q}{2C \, \ln(b/a)} \, \ln\left[1 + \frac{2V_a \, \kappa \, t}{p \, a^2 \, \ln(b/a)} \right] \qquad (3.16)$$

where q is the positive charge in the "ring" of ions and C the

electrostatic capacity of the counter. Thus the voltage reaches

$\frac{1}{2}$ V(T) = -q/2C, in a time, using (3.16),

$$t_{\frac{1}{2}} = a/b \left(\frac{b-a}{b}\right) T \simeq (a/b)T \qquad (3.17)$$

in this case $t_{\frac{1}{2}}$ = 7μsec).

Since the pulse rise times (for initial point ionization)

are determined solely in the avalanche region, and are

insensitive to the position in the low field region of the

initial event, in a practical situation the output pulses can

be "clipped" after a few microseconds with no loss of relative

pulse height information —— just a fixed attenuation determined

by the shaping circuit (Mathieson and Charles, 1969 a,b).

3.1.6 Factors Affecting Gain and Energy Resolution

Because of the heavy dependence of our understanding of

proportional counters on experimental data, it is worth dwelling

briefly on factors which can influence measurements.

Variations in anode supply voltage, anode and cathode

radius and gas pressure, have the effect of spreading the

counter response to mono energetic photons by varying the mean

gas gain in a manner described by equations (3.8), and

conveniently summarized in table (3.1). These effects are

particularly important in the large window area, multi-anode

counters where variation along a unit and from one unit to

another (particularly in anode values) are integrated into the

final overall response.

TABLE 3.1

PROPORTIONAL COUNTER PARAMETER VARIATIONS WHICH

PRODUCE A FIVE PERCENT CHANGE IN GAS GAIN

Anode Radius $a \times 10^{-3}$ (cm)	Gas Gain A	Anode Voltage $\Delta V_a/V_a(\%)$	Anode Radius $\Delta a/a(\%)$	Cathode Radius $\Delta b/b(\%)$	Pressure $\Delta p/p(\%)$
2.50	$1.5_{10}5$	+ 0.24	− 0.83	− 1.64	− 0.54
3.75	$1.3_{10}4$	+ 0.26	− 0.82	− 1.76	− 0.56
5.00	$2.2_{10}3$	+ 0.30	− 0.82	− 1.88	− 0.58

V_a = 2400 volts;   b = 2.5 cm;   p = 760 torr.

(see equation 3.8).

Field distortion at the ends of a counter (and near
window mounts) can affect resolution, particularly in the
present application where windows are as large as possible.
End effects can be limited by blocking photons which might be
absorbed in the field distorted regions, amounting to about a
cathode radius (2-3 cm) at each end. Other methods involve
shaping the field, for example, the field tubes of Cockroft
and Curran (1951), or the field electrodes used here in the
commercial counters of flight I (six concentric wires about
1 cm from the anode and operated at a voltage to comply with
the field requirement of equation (3.6)). Amplifier and
pulse height analyser noise and stability also affect
measurements.

Careful mechanical and electronic design and construction
can largely eliminate all these effects (see for example
Charles and Cooke). However there are a number of additional
factors, which can modify the ionizing and avalanche processes.

Capture of electrons formed in the initial ionization,
by electronegative impurities in the gas, results in slow
moving negative ions which do not contribute to the pulse
forming avalanche. Cross sections for electron capture vary
markedly with electron agitation energy and from gas to gas,
common contaminants being O_2, H_2O, NH_3, HCl and the halogens.
Wilkinson (pge. 39) gives a detailed discussion and includes a
very rough calculation indicating concentrations of O_2 present

to 1 part in 10^5 in argon at 760 torr. capture about 1% of electrons in a typical counter.

In the absence of electronegative gases, <u>recombination</u> of ion pairs is not a serious problem since it most often occurs via the formation of negative ions (in which case it is indistinguishable from electron capture), (Franzen and Cochran, pge. 214). Even so, the effect can occur at very low values of X/p (e.g. near the cathode). Watt (1967) gives values of X/p for various gases above which recombination effects are negligible. A value of 0.15 volts $cm^{-1}torr^{-1}$ for argon (and P-10) is one of the lowest, and can be compared with the 0.16 volts $cm^{-1}torr^{-1}$ obtained from equation (3.7) for a typical cathode.

Electron capture is also of possible relevance to the phenomenon of gas gain decreases at very <u>high count rates,</u> observed by many authors and summarised by Spielberg (1966). Space charge (Hendricks, 1969) accounts for most of the observed gain decrease effects, but not for variations with anode material, and Spielberg suggests that electron capture of avalanche electrons by impurities (avalanche debris or absorbed gases) ejected from the anode by preceding avalanches may contribute. A possibly related effect is the <u>ageing</u> in P-10 counters, first indicated by a resolution deterioration after about 10^8 counts, reported by den Boggende et al (1969). These authors convincingly attribute the ageing to a change in

anode radius due to deposited carbon compounds. A marked
improvement in lifetime (measured in number of counts) was
observed using an Ar - 20% CO_2 mixture.

Pure noble gases are unsuitable as counting gases because
of the long-lived <u>metastable states</u> (lifetimes $\gg$ the "clipping
time"), which are effectively removed by de-exciting collisions
with small amounts of a molecular gas ―― thus the CH_4 or CO_2,
etc. The additive gas fulfils two other essential functions.
Unlike argon, methane is relatively opaque to U-V photons which
might be liberated from ions or atoms excited in the initial or
avalanche ionizing processes; <u>photon successor avalanches</u>
resulting from photo-electric absorption of these photons
(mainly in the cathode) are therefore suppressed. That 10%
CH_4 in argon is ineffective in completely suppressing such
avalanches is obvious from the data of Carver and Mitchell, and
Gold and Bennett. Finally, in the 5 m sec or so that it takes
a positive ion to drift to the cathode, practically all of the
original ions will undergo <u>charge exchange</u> resulting in
molecular ions which lose energy by dissociation with the
cathode surface. In the simpler gases such dissociation is
impossible and a photoelectron is ejected, giving an <u>ion</u>
<u>induced delayed avalanche</u>.

3.2   GAS FILLING

The choice of proportional counter gas in X-ray astronomy is governed not only by the properties discussed in the previous sections, e.g.

(1)   ability to absorb the photons,

(2)   absence of electron capturing molecules,

(3)   suppression of successor avalanches, and

(4)   a combination of W, F and α to give minimum σ_p, i.e. good energy resolution,

but also by very important economic and convenience factors.

One first makes a decision on the mode of gas rejuvenation in the counter, choosing between

(a)   an "infinite" lifetime counter, requiring elaborate outgassing and sealing techniques,

(b)   a continuous flow counter, demanding an in-flight gas reservoir and sophisticated pressure regulating devices, or

(c)   a flush counter, with limited but useful sealed lifetime, and with emphasis on ease of rejuvenation and calibration. With large areas of thin plastic window, high temperature outgassing is not feasible, pin holes are difficult to detect and permeability to electron capturing gases (H_2O, O_2) exist, —— thus modes (b) or (c) are necessary. Both these modes consume large amounts of gas, mostly in extensive pre launch testing and calibration. Apart from the beryllium window-xenon filled, sealed counters of flights I and II, UAT counters have operated in mode (c).

The non-electronegative requirement suggests the inert
gases, He, Ne, Ar, Kr and Xe, and only the heavier members
efficiently, stop 15keV X-rays. The choice is simplified by
the high cost of Xe and Kr, also by very limited suitable supplies.
Commercial supplies are extracted from the atmosphere in which
contamination by 10 year half life Kr^{85} appears to be doubling
every four years (Clark and Gross, 1969); the source of
contamination is mainly the spent fuel elements from nuclear
reactors. Clark and Gross describe the limitations of
krypton filled counters. Similar results had already been
obtained in these laboratories with xenon filled counters in
which background counts of some 20,000 counts per minute were
recorded, compared to 100 counts per minute with pre-1960 gas.
That at least some of this was due to Kr^{85} was indicated by a
slight count rate decrease after preliminary fractionation of
the gas sample (b.p. of Kr, Xe are $-152^{\circ}C$ and $-107^{\circ}C$
respectively). (A.G. and K.B. Fenton, private communication).

The commercial availability of the counting gas P-10, an
argon-methane mixture in the ratio 9:1, at low cost and in
convenient high pressure cylinders makes it then the obvious
choice. This is not to say that it is the best possible gas
(e.g. section 3.1.4) and it appears that experimentation with
different mixtures, particularly with molecular gases has
received very little attention. The commercial grade P-10
(supplied by C.I.G. (Aust.) Pty. Ltd.) has the composition

listed in table (3.2). From the discussion in (3.1.6), this
mixture might be expected to have some electron capture due to
O_2 and H_2O, particularly as the cylinder empties. This, plus
uncertainties in the effect of the other impurities on the
ionization parameters (W, F and α) and ion mobility, imply
possible variations in gain and resolution from one cylinder
to the next, and emphasize the need for accurate calibration
and facility to easily adjust amplifier gains or bias levels.

Figures (3.1), (3.2) summarize the absorption properties
of the common gases. In figure (3.1) the mass per unit area,
x gm cm^{-2}, is plotted against depth (cm) for the inert gases at
760 torr and $0^\circ C$ and for P-10 at $0^\circ C$, $20^\circ C$ and $50^\circ C$. Figure
(3.2) gives the mass absorption coefficients, μ $cm^2 gm^{-1}$ (see
section 3.1.1) as a function of photon energy $h\nu$. The absorption
in the gas is from equation (3.2),

$$(I_0 - I)/I_0 \;=\; 1 - \exp(-\mu x) \tag{3.18}$$

The prominent absorption edges in figure (3.2) complicate data
analysis, both in the efficiency correction and because of the
escape peak mentioned in (3.1.1). For example, in argon some
13% of incident photons with $h\nu > 3.2$keV will result in
fluorescent (2.9keV) photons; a considerable fraction of these
are reabsorbed in the counter gas (or in gas of an adjoining and
paralleled unit in multi-anode counters) with no deleterious
effects. For the cases when a fluorescent X-ray escapes the
window or is absorbed in the walls an output pulse equivalent

TABLE 3.2

COMPOSITION OF C.I.G. COMMERCIAL GRADE P-10

| Component Gas	Concentration			
Methane (CH_4)	9 - 11%			
Ethane (C_2H_6)	1000 volumes per 10^6			
Nitrogen (N_2)	850	"	"	"
Propane (C_3H_8)	125	"	"	"
Carbon Dioxide (CO_2)	125	"	"	"
Hydrogen (H_2)	1	"	"	"
Oxygen (O_2)	20	"	"	"
Water Vapour (H_2O)	25	"	"	"in full cylinder at 15°C.
	60	"	"	"in 10% full cylinder at 15°C.
	900	"	"	"in 5% full cylinder at 15°C.
Argon (Ar)	~ 90%			
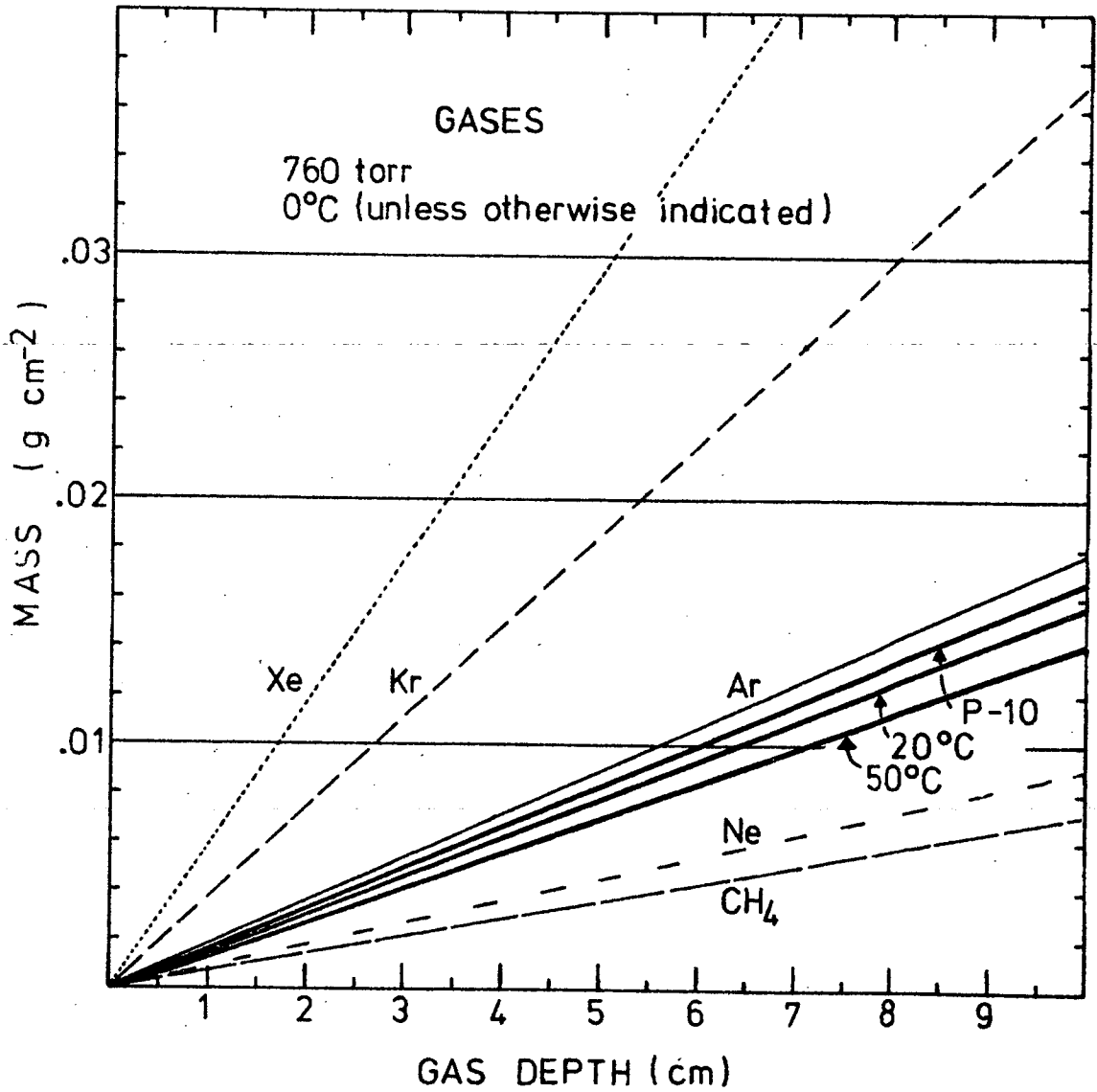
**FIGURE 3.1 : Mass per Unit Area for given Depth of counter gas.**
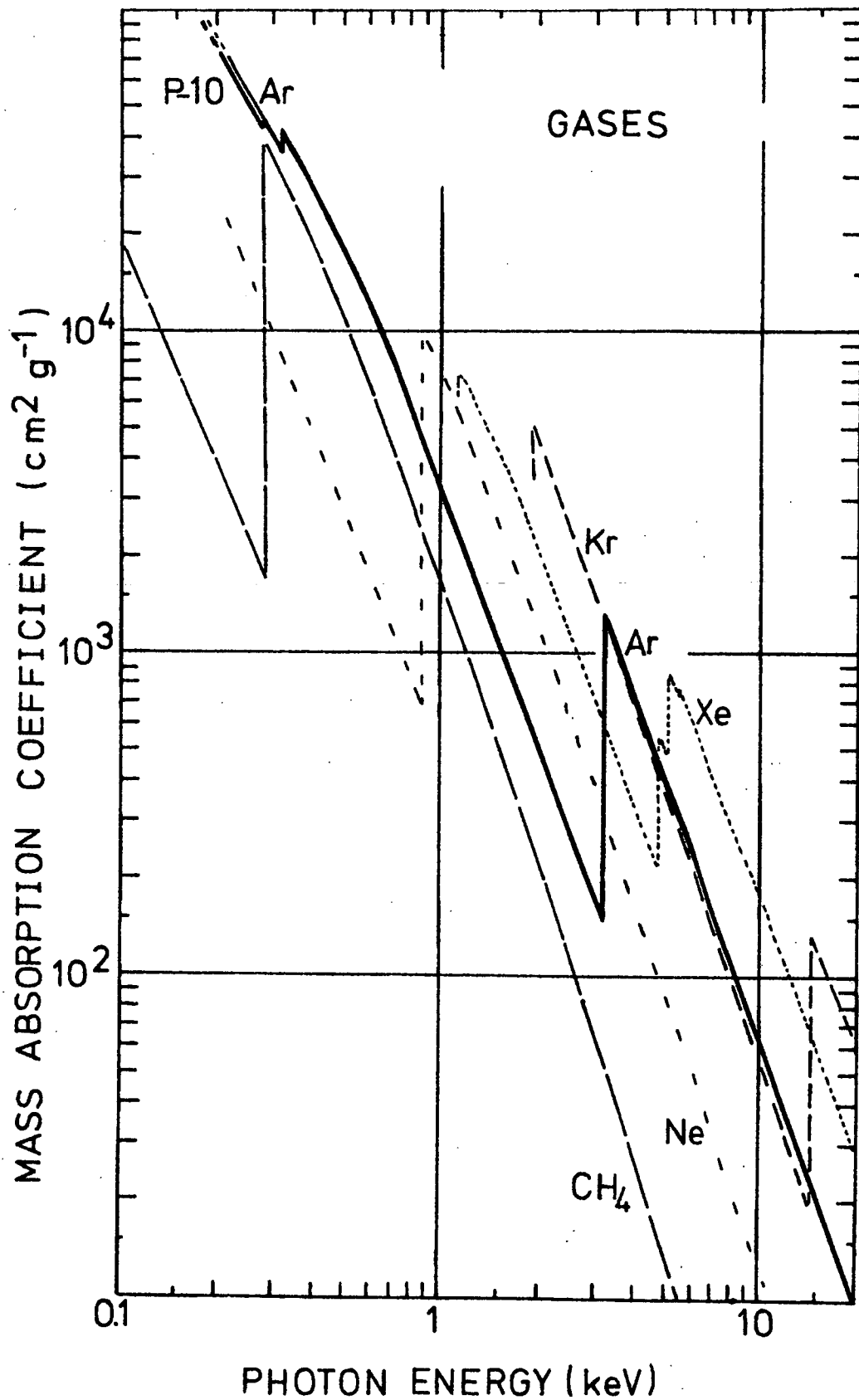
FIGURE 3.2: Mass Absorption Coefficients for X-rays in counter gases.

to the absorption of $(h\nu - 2.9)$ keV is observed. In some
counters it is also possible for escape X-rays to be absorbed
in the detecting medium of a surrounding "anti coincidence"
counter so that the event is totally vetoed and the detection
efficiency for photons > 3.2keV correspondingly decreased.

3.3   WINDOW MATERIALS

A counter window admits the low energy X-rays, at the
same time maintaining gas purity and pressure, and electric
field uniformity. Normally a thin, pinhole free, metal foil or
metallized conducting film is supported over the window area by
an open mesh or grid. These experiments have used the common
beryllium and aluminized polyethylene terephthalate (sold
commercially as Melinex by I.C.I. and as Mylar in the U.S.A.),
and a film new to X-ray astronomy, polypropylene (made by I.C.I.
under the trade names Propafilm and Propathene), similarly
aluminized. The plastic films have been effectively supported
against the inflight 760 torr pressure differential by
collimators - aluminium frames primarily constructed to define
the field of view (see section 3.5). In some cases the high
polymer films are "oriented", or stretched in one or more
directions to increase the tensile strength and stiffness in
these directions and this influences the orientation of the
window against an asymmetric collimator support.

The beryllium is obtained in guaranteed pinhole free, rolled sheets to a specified thickness and size. Sheets about 2.5 x 2.5 cm have been received and thickness variations of up to $\pm$ 20% have been obtained from careful measurements of the area and weight of individual sheets, assuming a density of 1.848 gm cm^{-3}. (Micrometer readings confirm the relative variations but tend to overestimate the mass due to the granular surface). No attempt has been made to check the purity of the foil for heavy metal content (e.g. as little as 1% by weight of iron in a 2 mil Be window decreases the 2keV transmission from 47% to 38%).

The plastic films must be given a conducting surface, otherwise static charge builds up as ions collect and eventually field distortions near the window prevents electron collection, particularly for low energy X-rays preferentially absorbed in this region. (Similar effects have been observed here with a poorly earthed conducting window). Approximately 1000Å of aluminium has provided the conducting surface. The evaporation technique may have produced variations in aluminium thickness of up to 50% since only rough optical transmission methods of monitoring have been employed, however at energies of 1.5 to 15 keV the errors are small. For example, in a worst case at 1.5keV, transmission through 40G polypropylene + 1000Å of Al is 53%, and with 1500Å, 50%. At 0.28keV the corresponding transmission figures are 7.1% and 4.7% respectively.

The physical properties of the two plastic films are compared in table (3.3). Melinex shows superior temperature and O_2 permeability properties but is markedly inferior as regards water vapour transmission. Despite this, no marked differences have been observed in counter behaviour from one window to the other, within the framework of normal routine and environmental testing (described in Chapter 4). The permeability numbers can be given some significance from the results of Culhane et al (1966). Using a $3.75_{10}-4$ cm (25G) Melinex window of .05 cm² area, they show that gas contamination in a normal laboratory environment is predominately due to water vapour permeability with about a 20% gain and energy resolution deterioration over several days.

A big advantage of the Propafilm is its markedly better X-ray transmission properties, compared with Melinex of similar thickness and strength (e.g. see figure 3.5). The specified mass per unit area (x gm cm⁻²) of common windows is shown in convenient form in figure (3.3); figure (3.4) gives the corresponding mass absorption coefficients μ, and the transmission is given by equation (3.2), i.e.

$$I/I_0 = \exp(-\mu x)$$

As with the beryllium, no attempt has yet been made to analyse these plastics for heavy impurities. Unlike earlier experiments, flights V and VI may yield results with sufficient inflight calibration, energy resolution and counting statistics to give

TABLE 3.3

PROPERTIES OF I.C.I. PLASTIC WINDOWS

	Melinex	Propafilm
Formula	$(C_{10}H_8O_4)_n$	$(CH_2)_n$
Synonym	polyethylene terephthalate	polypropylene
Density $(g.cm^{-3})$	1.395 - 1.405	0.90 - 0.91
Available thickness $(\times 10^{-4}cm)$	(6.35 (25G) (12.7 (50G)	10.15 (40G) 15.25 (60G)
Tensile strength (lb/sq.in)	27,000	25,000
Elongation at break (%)	70	70
Melting point ($^\circ$C)	260	170
Permeability to O_2 *	210	3500
Water Vapour Transmission **	42	10

I.C.I. test procedures   (*cc.m^{-2}(24hr)$^{-1}$ at 760 torr
    (50G film)   (differential, 25°C.
   (**g. m^{-2}(24hr)$^{-1}$ at 90% R.H., 38°C.
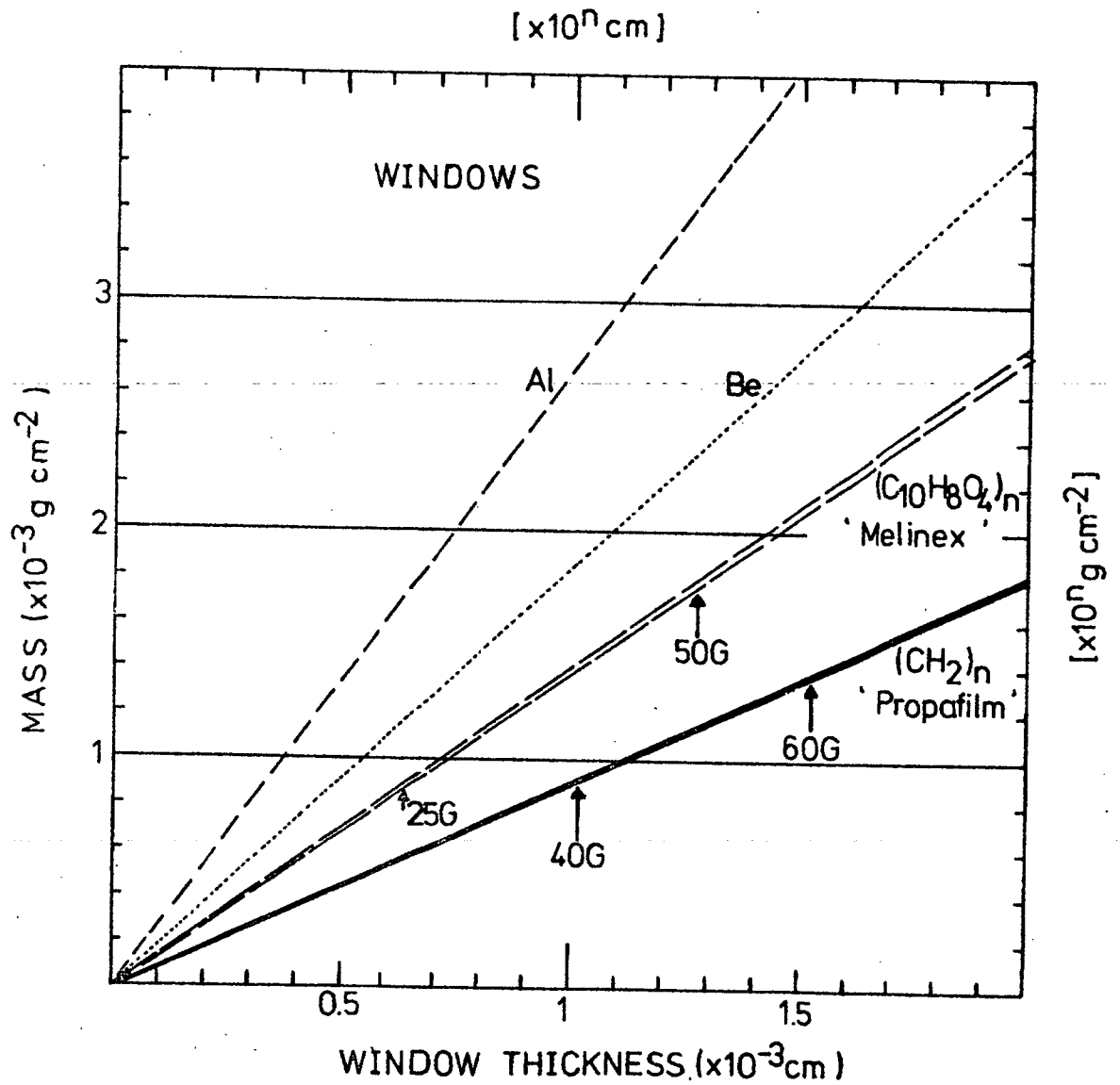
FIGURE 3.3: Mass per Unit Area for counter window
of given Thickness.
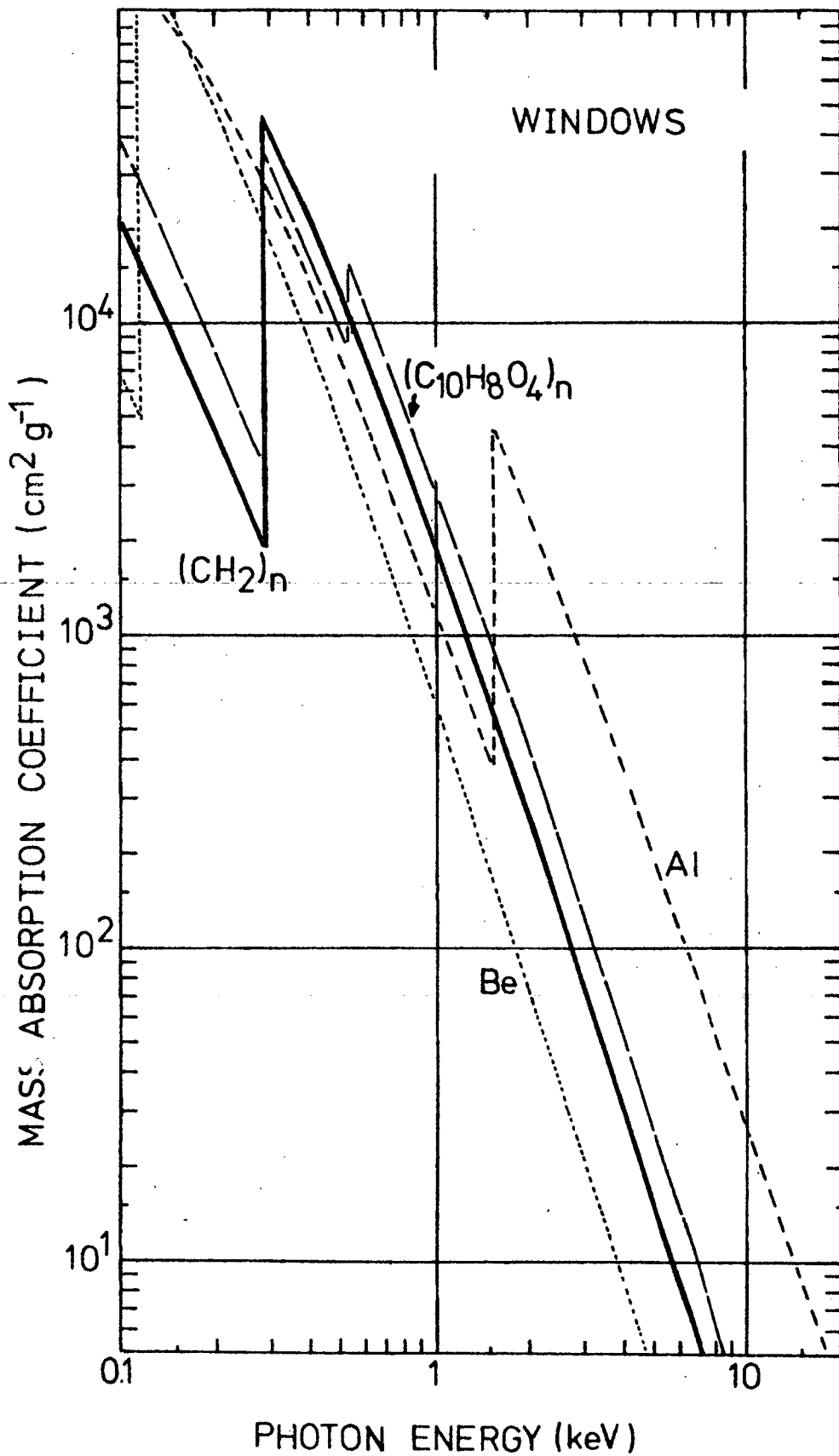
FIGURE 3.4: Mass Absorption Coefficients for X-rays in counter windows.

absolute spectra; in this case chemical analysis and/or direct
X-ray transmission measurements of sample windows will be
necessary.

Of interest is the carbon absorption edge in the plastic
films, at 0.284keV (43.5Å). This has received increasing
attention as a means of obtaining cosmic photon fluxes at
energies immediately lower than 0.284keV, and the flight IV
payload included a detector with electronics sensitive to these
energies (see section 5.4). Absorption edges of aluminium,
fluorine and oxygen compounds have also been employed by other
groups, to "fill in" spectra between 0.27keV and 2keV
(Rappaport et al 1969, Cornell et al 1968).

3.4   CORRECTION OF DATA FOR COUNTER EFFICIENCY AND RESOLUTION

The preceding sections have shown that the relationship
between the incident spectrum and the pulse height distribution
will be affected by absorption in the counter window, "non-
absorption" in the gas and by an intrinsic counter resolution,
to give a pulse height spectrum on the anode. Flight data can
be analysed by assuming a source spectrum, and, knowing the
detector properties, predicting a pulse height spectrum or
histogram with limits defined by the experiment pulse height
analyser (pha). A least squares comparison with the observed
pha count rates for a number of assumed input spectra then

determines a source spectrum of best fit. This technique was

used in the analyses of flights I and II (1967), and has since

been published in some detail by Gorenstein et al (1968).

It is instructive, and a useful design exercise, to

anticipate source and detector properties and carry out part

of this procedure on a known X-ray source. This is done here

for the T8 counters (section 4.1), and for a Sco XR-1 type

spectrum described by the simple exponential

$$I(h\nu) = 50 \; exp(-h\nu/5)/h\nu \quad photons \; keV^{-1} \, cm^{-2} \, sec^{-1} \quad (3.19)$$

plus a line at 6.9keV with a ratio of power in line to power

in 1.5 to 6 keV continuum of $5_{, 0}$-3 (as suggested by the data of

Holt et al, 1970). This spectrum is shown, marked I, in

figure (3.5), where for convenience, the line is shown with a

width of 100 eV (one plotter step), centered about 6.95keV.

Representing the counter absorption efficiency by $\xi(h\nu)$,

the number of source X-rays which give a response in the

counter is from equations (3.2), (3.18), simply

$$I\xi = I(h\nu). \; exp(-\mu x)_w . (1-exp(-\mu x)_g)$$
$$photons \; keV^{-1} \, cm^{-2} \, sec^{-1} \quad (3.20)$$

with discontinuities at window and gas absorption edges. A

simple power law fit, $\mu = K(h\nu)^k$, to the mass absorption

coefficients of Henke (section 3.1.1) has been employed for

both the polypropylene and P-10 of the T8 counters, with

separate evaluations of the constants above and below the

carbon and argon K absorption edges respectively. (The power

law approximation produces a maximum deviation from the data of

about 5% over the 1-10 keV range of prime importance, outside

this range errors are larger). Equation (3.20) is displayed

in figure (3.5), marked $I\xi$.

The actual efficiency of the counter is modified by the

escape phenomenon discussed at the end of the previous section.

Preliminary tests indicate that about 40% of the fluorescent

X-rays escape the sensitive X-ray volume, and of these, about

50% are not absorbed in veto, or anti-coincidence counters.

Thus, ignoring the argon L edge, (3.20) can be expressed as

$$
\begin{aligned}
I\xi(h\nu < 0.28) &= I\xi(h\nu) \\
I\xi(0.28 < h\nu < 3.2) &= I\xi(h\nu) + F_1\, I\xi(h\nu + 2.9) \\
I\xi(h\nu > 3.2) &= F_2\, I\xi(h\nu) + F_1\, I\xi(h\nu + 2.9)
\end{aligned}
\right\} \quad (3.21)
$$

where $F_1 = (.13)(.4)(.5) = .026$, and $F_2 = 1-(.13)(.4) = .948$

The response of the T8 counter to mono energetic X-rays,

is shown in section (4.4.2) to be gaussian with standard

deviation

$$
\sigma \simeq S\,(h\nu)^{\frac{1}{2}}, \quad \text{with} \quad S = 0.18,
$$

similar to equation (3.13), where pulse height H is measured

in keV and $h\nu = \bar{\bar{H}}$. The pulse distribution is then

$$
P(H) = \int \frac{1}{\sigma\sqrt{2\pi}} \exp\left[\frac{-(H-h\nu)^2}{2\sigma}\right] I\xi(h\nu)\, d(h\nu) \qquad (3.22)
$$

This expression has been numerically integrated over three $h\nu$

regions of continuous $I\xi$, for pulse heights between 0.1 and

10keV. The results are added, along with the gaussian response

to the 6.9keV line (magnified inset) to give the curve P (17.5%)

for both 40G Propafilm and 50G Melinex in figure (3.5). The
percentage refers to the FWHM at the calibrating 5.9keV
energy, obtained from equation (3.12). The calculation has
been extrapolated to very low energies, ignoring possible
source spectrum modification, modifications in efficiency
(e.g. due to evaporated Al) and uncertainties in counter
behaviour. The results show qualitatively the effect of the
carbon edge on efficiency.

Assuming that the continuum spectrum can be accurately
established (a situation not expected unless several large
calibrated detectors are included in a payload), the
possibility of observing the 6.9keV line at this strength
can be expressed in terms of the observation time with a
400 cm² counter to give a number of counts greater than three
times the standard deviation of the continuum counts in a
selected energy interval, (assuming negligible background
counts). Table 3.4 summarizes the situation, where for three
counter resolutions 10%, 17.5% and 25% FWHM (5.9keV),
observation times are listed for pha channel widths of
approximately 2, 3 and 4 times the standard deviation of the
counter response at 6.9keV. A 10% FWHM (5.9keV) has not yet
been achieved with proportional counters but is included as
a possible best resolution using alternative gas mixtures
(see section 3.1.4); the 25% FWHM (5.9keV) represents a
similar situation to the Holt et al experiment. A spin
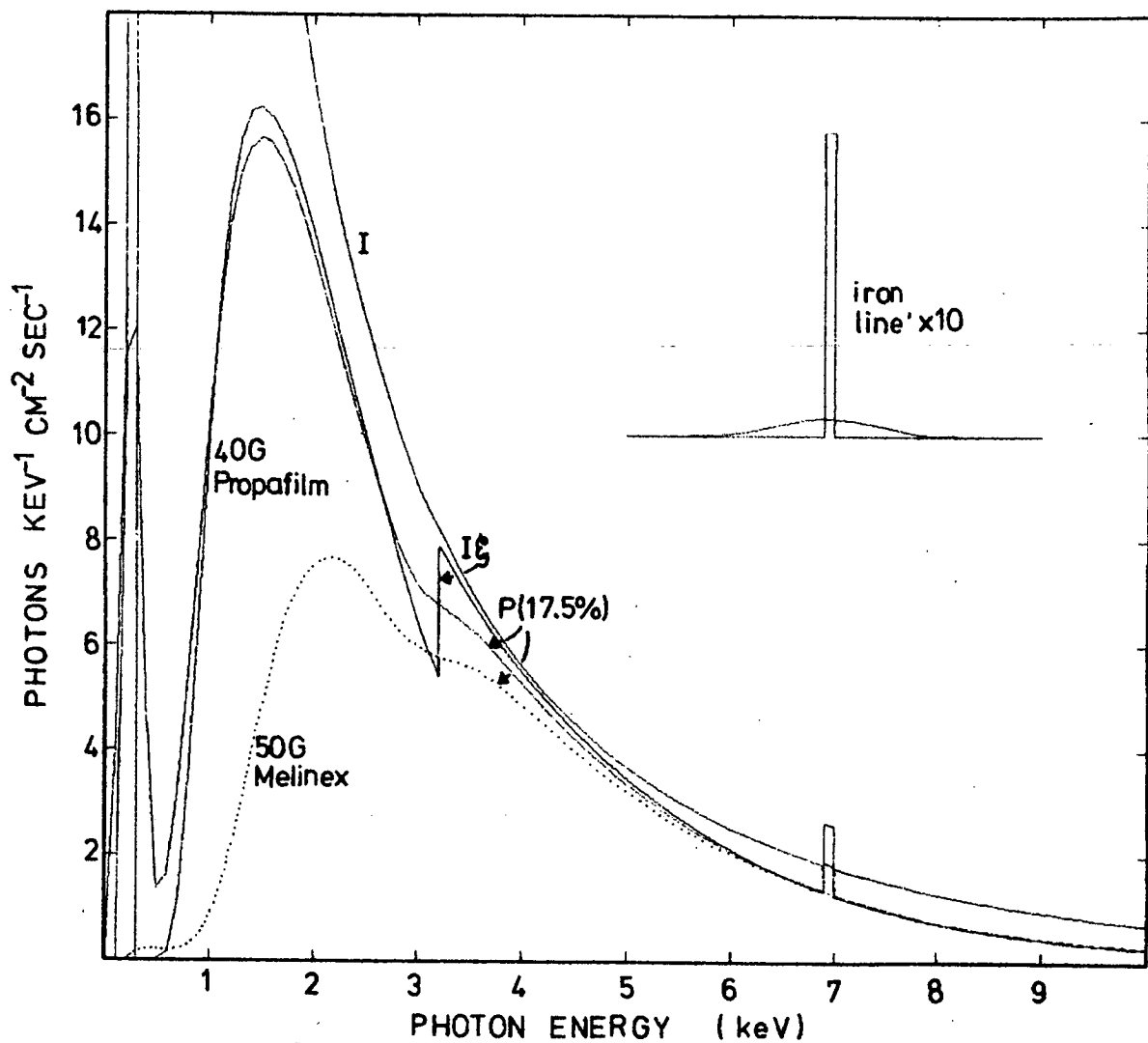
FIGURE 3.5: Effect of Absorption Efficiency (ξ), and Resolution FWHM (5.9keV) = 17.5% , on incident SCO XR-1 type spectrum (I).

TABLE 3.4

OBSERVATION TIME OF SCO XR-1 TO DETECT 6.9keV LINE

Counter area   =   400 cm²

Line strength   =   8 photons (cm² sec keV)⁻¹

FWHM (5.9keV) %	σ(6.9keV) keV	Channel Width keV	Observation Time sec.
10	0.29	0.6	2.1
		0.9	2.05
		1.2	2.3
17.5	0.47	1.0	3.7
		1.5	3.3
		2.0	3.9
25	0.73	1.4	7.3
		2.1	5.2
		2.8	5.9

(N.B.   For an established continuum spectrum).

stabilized rocket launched at a suitable time, will allow an
observation time of up to 10 seconds during a flight.

3.5   BACKGROUND COUNTS

The previous discussion has ignored the background
contribution to the measured count rate. Apart from the
point source and diffuse cosmic X-rays, a proportional
counter at rocket altitudes responds to a variety of other
radiations which are discussed here under four headings,
namely

(1)   high energy charged particles (e.g. cosmic rays) which
deposit energy by ionization in the counter gas and
immediate environment,

(2)   gammas, betas, etc, resulting from nuclear collisions
in the counter environment and indirectly or directly
ionizing the gas.

(3)   low energy electro magnetic and charged radiations
(e.g. of geomagnetic or solar origin) penetrating the window
and depositing their total energy in the counter, and

(4)   an intrinsic counter background.

3.5.1 High Energy Ionizing Particles

The high energy charged particle flux at rocket
altitudes consists of primary cosmic rays, with energy

exceeding the local geomagnetic cutoff. At Woomera $\{-31.5^{\circ}$S

and with a McIlwain L parameter, $L \simeq 1/\cos^2$ (geom.latitude)

$= 1.8\}$ protons of energy greater than 5.2GeV are allowed

from the vertical direction. This implies intensities

ranging from .06 particles $cm^{-2} sec^{-1} ster^{-1}$ at **solar**

minimum, to .03 particles $cm^{-2} sec^{-1} ster^{-1}$ at solar maximum

(McDonald and Webber, 1962). An atmospheric albedo (mostly

electrons with sufficient energy to penetrate the counter

walls, can amount to 5-10% of the primary intensity

(Charakhch'yan et al, 1967).

The count rate of an efficient convex detector in a

semi-spherical isotropic flux of J particles $cm^{-2} sec^{-1} ster^{-1}$

is

$$C = \frac{1}{2} \ \pi \ JS \ \ \text{counts sec}^{-1} \qquad\qquad (3.23)$$

where S (cm^2) is the surface area of the detector.

The majority of fast charged particles lose energy in

the counter gas by inelastic collisions with atomic electrons.

Following Evans (pge. 637), there are a very small number of

"hard" collisions, in which the energy transferred to the

atomic electron is much greater than the electron binding

energy, and the ejected swift electron, or δ-ray, produces

secondary ionization. In the remaining ionizing collisions,

the energy transfer ranges down to the excitation or

ionization energy of a single atomic electron. In an absorbing

medium containing N atoms cm^{-3}, each of atomic number Z, the

dependence of the average ionization and excitation loss along path ds, by a heavy particle of velocity βc and charge ze, is well approximated by

$$\frac{dE}{ds} \simeq \frac{4\pi e^2 z^2 NZ}{m_e \beta^2 c^2} \left[\ln \frac{2m_e \beta^2 c^2}{I(1-\beta^2)} - \beta^2 \right] \qquad (3.24)$$

with $I \simeq 13.5\ Z(eV)$. Accurate and comprehensive tables of ranges and stopping powers for a variety of absorbers are listed by Barkas and Berger (1964). For protons, (3.24) has a minimum at $\beta \simeq 0.95$, ($E \simeq 2GeV$) and the energy loss rate for these <u>minimum ionizing particles</u> in argon, krypton and xenon (NTP) are

$$
\begin{array}{lll}
\text{Ar} & \simeq & 2.7 \text{ keV cm}^{-1} \\
\text{Kr} & \simeq & 5.0 \text{ keV cm}^{-1} \\
\text{Xe} & \simeq & 7.3 \text{ keV cm}^{-1}
\end{array}
\qquad (3.24a)
$$

It is obvious that most particles deposit energies in excess of about 10-15 keV in a 5 cm deep counter (particularly in the heavier gases), and so will be rejected by a pulse height analyser looking at the lower energy X-rays.

The passage of the charged particles through the counter <u>walls</u> can also lead to events which are recorded. These include δ-rays released into the gas, bremsstrahlung radiation from the primary particle and δ-rays, and fluorescent X-rays following ionization in the walls. In the majority of cases these will be associated with and indistinguishable from primary ionization in the gas and neglected as above. Very similar effects arise from Compton

collisions in the walls, this time unaccompanied by primary

gas ionization, and discussed in more detail in the next

sub section.

3.5.2 Nuclear Interactions

Rocket borne and laboratory experiments, in which the

high energy charged particle background has been efficiently

rejected, have shown that as much as half of the total non

X-ray background is unexplainable in terms of ionizing

primaries, even though a dependence similar to that in

equation (3.23) persists; (Fisher and Meyerott 1966, Culhane

et al 1966, Gorenstein and Mickiewicz 1968, Cornell et al

1968). Furthermore Gorenstein et al (1969), establish that

more than 90% of the "unexplainable" component at rocket

altitudes is detected in the counter in the form of charged

particles, with extended ionization paths.

Nuclear collisions between primary cosmic rays and

matter in and near the rocket are the most obvious source

of the additional background. Gamma rays from photon

electron cascades and from the decay of radioactive isotopes

produced in the collisions, and betas also from the

radioactive isotopes are likely candidates. (At atomic

numbers representative of the rocket matter, the predominant

radioactive decay is typified by a 1-2 second half life,

ejecting a $\pm$ beta of about 5MeV accompanied by gammas around

1-2 MeV).

The gamma rays, for which the counter has an omnidirectional sensitivity, and which can release electrons into the gas as a result of <u>Compton collisions</u> in the walls and gas, are widely quoted as being responsible for the background remaining after fast charged particle rejection. In a Compton collision between a gamma
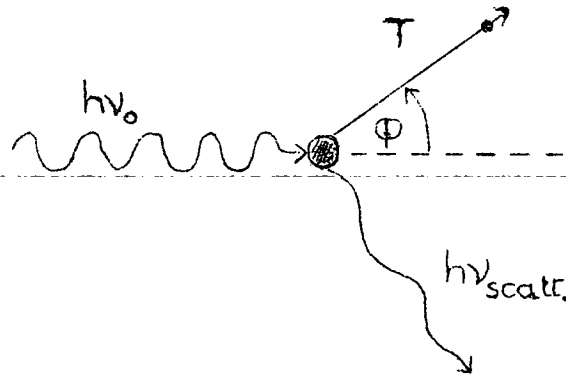
of energy $h\nu_0$ (MeV) and an atomic electron of rest mass $m_e c^2 = 0.51$ MeV, the electron receives energy T given by

$$T = h\nu_0 \frac{2\alpha \cos^2 \varphi}{(1+\alpha)^2 - \alpha^2 \cos^2 \varphi}$$

where $\alpha = h\nu_0/m_e c^2$. Maximum energy transfer occurs when $\varphi = 0$, i.e.

$$T_{max} = \frac{h\nu_0}{1 + (1/2\alpha)} \tag{3.25}$$

The energy distribution of Compton electrons is peaked at T_{max}, falling off rapidly to a relatively constant value which persists until zero energy.

Table (3.5) gives the photon attenuation lengths, (total mass absorption coefficient x density)$^{-1}$, in argon (column 2) and aluminium (column 3), (representing the counter gas and walls respectively), for incident gammas of

TABLE   3.5

ENERGY AND RANGE OF GAMMA RAYS AND COMPTON ELECTRONS

(1)	(2)		(3)	(4)
Gamma Energy	Gamma Attenuation Length (cm)			Maximum Compton Electron energy (MeV)
$h\nu_0$ (MeV)	Argon (NTP)		Aluminium	
0.1	$3.0_{10}3$		2.3	0.05
1.0	$9.8_{10}3$		6.0	0.79
10.0	$2.3_{10}4$		16.1	9.75

(4)	(5)		(6)	(7)
	Maximum Electron Range (cm)			Bremsstrahlung Yield in Aluminium
(MeV)	Argon (NTP)		Aluminium	
0.05	2.4		0.0015	0.0005
0.79	170		0.11	0.007
9.75	2800		1.85	0.18

0.1, 1.0 and 10 MeV. Mass absorption coefficients are
taken from Grodstein (1957); since they predominantly
represent Compton interactions they are nearly independent
of the nature of the absorber and absorption is determined
by the mass $(g.cm^{-2})$. For example at 1 MeV, the efficiency
for Compton collisions in a 0.5 cm wall is $\sim 8\%$ and in 5 cm
of gas $\sim .05\%$. Column 4 gives T_{max}, so that Compton electron
energies from 0 to T_{max} are represented for a given gamma
energy. The ranges of electrons of energy T are
approximately described by

$$.01 < T < 3\text{MeV}, \quad R(mg.cm^{-2}) = 412 \ T^n, \quad n = 1.265 - .0954 \ \ln T \left.\begin{array}{c} \\ \\ \end{array}\right\} (3.26)$$
$$1 < T < 20\text{MeV}, \quad R(mg.cm^{-2}) = 530 \ T - 106.$$

Alternatively accurate and comprehensive tabulations of
ranges and stopping powers are listed by Berger and Seltzer
(1964). Ranges of the T_{max} electrons are given in columns
5 and 6. The relatively large ranges in aluminium show
that collisions deep in the wall can release electrons into
the gas. The fast electrons have a minimum ionizing energy
at about 0.7MeV, where in argon (NTP) the ionization loss
rate is about 2.5keV/cm. (The loss rate increases only very
slowly with increasing energy, but rises rapidly as T
approaches zero).

The Compton electrons will be indistinguishable from
betas arising from the decay of light isotopes produced near
the counter, both (after passage through the counter walls

etc.) having energies ranging from those representing near minimum ionizing electrons, to zero energy. In general, background rejection techniques are equally effective for both sources of electrons.

Electrons in the <u>walls</u> can indirectly initiate pulses in the counter by radiating bremsstrahlung X-rays, or by exciting fluorescent X-rays, which are absorbed in the gas.

The bremsstrahlung contribution is indicated in column 7 of table (3.5) for electrons .05 - 10 MeV in aluminium and only becomes appreciable for electrons > 10MeV. A $(1/M_0)^2$ dependence makes heavy particle bremmstrahlung negligible.

<u>Fluorescent X-rays</u> arise from de-excitation of ionized wall atoms, where ionization results from Compton and decay electrons, primary and secondary charged particles and δ-rays (those not accompanied by primary ionization of the gas being of particular significance). The K fluorescent yield in aluminium (see section 3.1.1) is 3% and the attenuation length of the isotropically released K X-rays (1.49keV) is 10^{-3} cm. Again the effect is small.

3.5.3 Low Energy Radiation

This sub-section is concerned <u>only</u> with background rates determined by the window area, rather than the total counter surface area as above. With a minimum of mass immediately above the window, the number of incident nuclear

secondaries from this direction will be small. The

efficiency of detection for normally incident charged

particles is summarized in table (3.6), where the energies

and stopping power are given for protons and electrons with

ranges equivalent to wall, window and gas thicknesses.

Ranges and stopping powers for protons and electrons have

been taken from tables of Barkas and Berger, and Berger and

Seltzer, respectively. {The data for polypropylene is in

fact that quoted for polyethylene which has a similar

composition, $(CH_2)_n$, and density (0.9 g cm^{-3}) }.

For example, in a T8 counter incident electrons with

energies less than 2.2MeV are stopped in the walls, and

access to the gas is only through the window; for energies

less than 23keV the window becomes opaque. Those electrons

which traverse the full 5 cm depth of gas {i.e. emerge from

the window with > 65keV (and therefore reach the window with

about 70keV or more)}, deposit a minimum of (5×2.5) keV,

and up to (5×6.8) keV in the gas, and give pulses mostly

outside the range of interest (see equation 3.24a).

Similarly for electrons with energies less than 70keV, only

a small fraction deposit less than about 10keV in the gas.

This is a result of the rapidly increasing stopping powers

at low energies, and can be seen from the fact that the

difference in ranges in polyethylene for 20 and 25 keV

electrons is $4_{.0}-3 \text{ g cm}^{-2}$, a range equivalent to that of

TABLE 3.6

ENERGY AND STOPPING POWER OF "THRESHOLD" PARTICLES
IN COUNTER

E = energy in <u>MeV</u>, corresponding to given range

S = stopping power in <u>keV/cm</u> in ARGON, corresponding to E.

Range ($g\ cm^{-2}$)	Electrons		Protons	
	E	S	E	S
0.5 cm Aluminium 1.35	2.2	2.7	32	21
40G Polypropylene 10^{-3}	.023	13.5	1	570
3 mil. Beryllium $1.5_{10}-2$	.093	5.3	2.2	150
5 cm (NTP) Argon 10^{-2}	.065	6.8	1.7	180

10keV electrons in argon. In other words only a narrow
"slice" of the incident electron spectrum, about 5keV at
23keV, is totally absorbed to give pulses in the X-ray
range. The corresponding figures for the 3 mil beryllium
window are about 1keV at 93keV. If it is assumed that the
electrons have an (omnidirectional) energy spectrum similar
to that given by Cladis (1961) for the inner Van Allen belt
electrons, i.e.

$$dN/dE \simeq 132\ E^{1.6} \cdot \exp(-.022E)\ \text{electrons cm}^{-2}\text{sec}^{-1}\text{keV}^{-1} \quad (3.28)$$

(even though there is no experimental verification for such
an assumption, and remembering that the trapped electron
spectrum is variable and may be further modified by a
precipitation process) then the relative sensitivities of the
polypropylene and beryllium windows to low energy electron
contamination will be about 50 to 1.

For protons with higher window threshold energies the
rejection of particles stopped in the gas is much more
severe. Also the background contribution of protons and
electrons (<32MeV and 2.2MeV, respectively) which do not
stop in the gas, but which have path lengths small enough
to deposit < 10keV, are practically eliminated by a collimator.
Both effects will be negligible compared to the lower energy
electron "slice".

Early X-ray astronomy flights using thin window geiger
tubes and scintillators concluded that the possible low

energy charged particle contamination of X-ray measurements
at mid latitudes was small. For example Gursky et al (1963),
whose rockets were launched from White Sands, New Mexico
(32°N, L $\simeq$ 1.7) during 1962-1963, dismissed an electron
contribution on the grounds of a comparison of results from
detectors with markedly different responses, a lack of
anisotropy around the local magnetic field direction and a
constant count rate versus altitude above 100 km. With the
advent of proportional counters, the detector insensitivity
to low energy charged particles, and isotropy of the
measured background have been almost universally used as
sufficient argument against contamination; this, despite the
development of large areas of thinner windows, and the
possibility of variable electron spectra with undetermined
isotropy.

Direct observations of mid latitude, rocket altitude
charged particle fluxes are sparse. However the results of
O'Brien et al (1965) deserve special mention. A rocket
launched from Wallop Is., Virginia (38°N, L $\simeq$ 2.5) in July,
1963, carried, among other detectors, a small pair of thin
window geiger tubes, one with a magnetic broom. A count
rate difference was observed, and from considerations of the
thresholds of window and field penetration, it was concluded
with 99% confidence limits, to be due to electrons with
energies between 40keV and 1MeV. The diffuse count rate was

some 8 times higher than that implied by the Gursky results.
Assuming the Cladis spectral shape (3.28), the O'Brien flux
can be related to the UAT flights. For example such
electrons would have contributed less than 0.3% to the
measured 2-8 keV background count rates of the flight I, II
beryllium window counters. With 40G Propafilm windows
electrons may have contributed up to 20% of the diffuse
background.

Early satellite observations by O'Brien, also at
L ≃ 2.5 but nearer solar maximum and at higher altitudes,
indicated precipitated electron fluxes 10 to 100 times
greater than implied by the rocket result. O'Brien makes
two important comments,

(1)   Even the smallest of the precipitation events
measured represents an appreciable drain on the Van Allen
belts, implying that they are relatively infrequent. On
the other hand, detection may be difficult since

(2)   during the larger events, isotropy of the electrons
(rather than a pitch angle distribution with maxima
perpendicular to the field) might be expected.
Confirmation of widespread electron precipitation during
1967, at low L values and at an altitude around 500 km,
has recently come from scintillator observations from
OSO-III by Schwartz (1970).

Rocket observations of Hayakawa et al (1966) suggest

a possible altitude dependence of the precipitated particles

which might partly explain the high satellite fluxes reported

by O'Brien. They report a steady count rate increase from

about 200 to 1000 km at Uchinoura (31°N, L $\simeq$ 1.1),

attributed to low energy electrons. The effect was assumed

negligible at 100 to 200 km.

In summary, it is felt that the possibility of low

energy charged particle contamination of mid latitude cosmic

X-ray fluxes should be considered for each individual flight,

with particular reference to geomagnetic disturbances that

might accompany large fluxes of precipitated electrons (e.g.

the magnetic Kp index). Smaller corrections may be necessary

for a steady "drizzle" of particles from the inner radiation

belts (Kennel and Petschek, 1966) with possibly some low

energy albedo electrons from the atmosphere (Charakhch'yan

et al, 1967). The possibility of electron contamination

receives further attention in section 7.2, where the

particularly variable diffuse X-ray observations are discussed.

Bremsstrahlung X-rays from very high fluxes of

precipitated electrons at high latitude stations, can be very

intense compared with the cosmic X-ray fluxes and high

latitude launch stations are undesirable for low level work.

Results have been obtained from Resolute (L $\sim$ 100) reporting

both cosmic and local X-rays (Wilson et al, 1969). Measurable

localized X-rays also result from <u>scattering and fluorescence</u>

<u>off the atmosphere</u> of the very strong solar X-ray fluxes

(Harries and Francey, 1968, see section 5.1.4). At energies

less than 1keV a <u>diffuse airglow</u> is particularly serious, and

persists well after sunset (Grader et al, 1969).

3.5.4 Intrinsic Counter Background

A source of counter background will be long lived

<u>radio-active impurities</u> in the gas and construction materials.

These problems have been discussed by Kocharov et al (1967),

who list observed counting rates from common materials. For

example β rays from commercial aluminium give among the

highest count rates for possible construction materials

contaminants amounting in the UAT worst-case (largest wall

area), to about 4 counts sec^{-1}, compared with about 200

counts sec^{-1} due to the isotropic cosmic X-ray background.

Since many of the common β active contaminants will deposit

much greater than 10keV in the gas (e.g. C^{14} at 156keV, H^3

at 18keV), pulse height analysis will make the effect very

small. Alpha particles from natural sources deposit 2-10

MeV and are more efficiently rejected. Gamma rays

accompanying the radioactive decay of impurities are

inefficiently detected (3.5.2) and will also give small

effects. The effect of Kr^{85} and perhaps other contaminants

in xenon and krypton gas fillings has already been discussed,

section (3.2). The count rate due to radon-free P-10 (Rn half

life 3.8 days), used by Kocharov et al, would be quite

negligible in a large UAT counter.

Laboratory tests on different UAT counters have shown a

number of pulse effects (ranging from very small to very large

pulses) associated with _electrical breakdown._ Thorough

cleaning of anode wires, insulators and EHT capacitors

effectively removes the majority of these, however for some

counters the evidence for a persisting infrequent (less than

1-2 per sec.) very large discharge pulse is strong. The

phenomenon is adequately explained in terms of a "Malter

effect" discussed by Benjamin et al (1968), and resulting

from small insulating deposits (e.g. tungsten oxide) on the

tungsten anode wires which emit heavy charged particles above

certain electric field values. These authors effect a cure

by heating the tungsten to $1000^{o}C$ in vacuum, a process not

easily achieved in situ with large area thin plastic window

counters, and in view of the low rate and efficient pulse

height rejection, not yet attempted here.

3.5.5 Background Rejection Methods

Pulse height rejection has been mentioned throughout

the previous discussion and is an intrinsic property of a

counter operated in the proportional mode to obtain pulse

height information. The rejection efficiency can be

enhanced by choosing a gas in which the charged particle

energy deposition for most path lengths exceeds that due to

X-rays being studied, e.g. see equations (3.24a). The

rejection efficiency for the high energy charged particles

is then determined by the geometry of the counter, and for

example in the flight I and II xenon-filled counters, more

than 75% of paths due to an isotropic flux of minimum

ionizing protons deposited more than 8keV in the counters.

Mesons are similarly rejected, whereas heavier particles are

almost totally vetoed. Minimum ionizing electrons with

moderate path lengths can still be recorded.

In argon, pulse height rejection is considerably less

efficient than in xenon and coincidence rejection is most

commonly utilized. Two or more counters are placed in close

proximity and pulses occurring "simultaneously" in different

counters are rejected. This has no effect on X-rays which are

completely absorbed in a collision with an atom, but removes

pulses due to fast charged particles which pass through more

than one gas volume with an efficiency again determined by

geometry. The vetoing circuit must accept pulses separated

by a time determined by the maximum drift time of electrons

in any counter, so introducing a "dead" time. The veto

efficiency, V, for a "pill box" counter of diameter, L, and

depth, d, which is backed by an identical guard is

$$V = \frac{L}{L + d}$$

Such an arrangement was used by Culhane et al (1966) with $\dot{V} = 0.7$, however the measured background rejection in the laboratory was 0.5 compatible with the total background comprising roughly equal contributions from fast ionizing particles and nuclear effects (see 3.5.2). It is therefore necessary to subscript V to indicate that it applies only to the high energy ionizing (mostly cosmic ray) component, i.e. V_{cr}. In the case of two identical rectangular box counters (length L, width W, depth d) placed back to back (i.e. forming a box L x W x 2d),

$$V_{cr} \simeq \frac{L}{L+W} \left(\frac{W}{W+d}\right) + \frac{W}{L+W} \left(\frac{L}{L+d}\right) . \qquad (3.29)$$

In order to reduce the background due to electrons released from the walls, counters have been developed in which the main X-ray counter gas volume is in immediate and extensive contact with the detecting medium of the guard, i.e. "wall less" counters with coincidence rejection. The T8 counters (see figure 4.1) embody this principle. The X-ray detecting counter is surrounded on three sides by other proportional counters, all sharing one gas volume and electrically isolated by widely spaced wire grids. V_{cr} is obtained (3.29) with the term $W/(W + d) = 1$. The "scattered" background is reduced from the thick walled

case by the ratio of the area of the walls replaced by grids

to the total surface area of the counting volume (with

adjustment for the relative masses and positions of

scatterers). Cornell et al (1968) quote a laboratory back-

ground rejection measurement on an aluminium counter with

three sided guard, in which molybdenum (ρ = 10.2 g cm^3) mesh

separates the compartments and supports the window; a

collimator of brass slats was used. For their arrangement

equation (3.29) gives $V_{cr} \simeq$ .99, and V_{meas} was 0.7 ($\curvearrowright$

constant over 1-6 keV).

A final background rejection method uses <u>pulse rise-time</u>

<u>discrimination</u>, relying on the different path lengths in the

gas of photo-electrons (released after X-ray absorption), and

charged particles (primary cosmic rays, δ rays and most other

electrons), which deposit similar amounts of energy. The

electrons resulting from an extended ionization path have

differing drift times into the avalanche region - except for

paths aligned with the anode wire. The superposition of

avalanches initiated by the electrons at different times

gives a slow rise pulse compared to that for an initial photo

electric absorption in the gas when the total particle energy

is normally absorbed in $\ll$ 2mm (see section 3.1.2). The

exceptions will include photo electric absorptions accompanied

by κ X-ray emission when the κ X-ray is reabsorbed in the gas.

By choosing a gas in which the electron drift velocity is

small, discrimination is improved; also since the pulse rise
time due to every individual avalanche is determined by the
ion mobility (equation 3.16), this must be relatively fast.
The method is described in more detail by Mathieson and
Sanford (1963), Gorenstein and Mickiewicz (1968), Ricker
and Gomes (1969) and Gott and Charles (1969). Gorenstein
et al (1969) have successfully employed pulse rise time
discrimination in rocket borne experiments, with typical
performance given at ~90% rejection of total background
accompanied by a 20% loss in X-ray efficiency, above about
2.5 to 3 keV.

3.6   COLLIMATORS

The collimator (see Appendix C3) can be considered an
intrinsic part of the UAT proportional counter, determining
the direction and field of view, mechanically supporting and
shielding the window and influencing the background. In an
experiment to study point X-ray sources the prime
considerations in collimator design are
(1)   good resolution of closely spaced sources, within
limitations set by the rocket motion, telemetry sampling
time and/or a collection of a statistically significant
number of source photons;

(2)   minimum sensitivity of observed count rate profiles on the collimator response function and attitude solution, and

(3)   if not already determined, a small solid angle to reduce the diffuse background.

If, on the other hand the <u>diffuse</u> X-ray flux is to be studied, then

(1)   the solid angle is increased to collect more photons and reduce sensitivity to (unresolved) point sources, and

(2)   the shape and direction of the field is chosen for a given rocket motion, to minimize possible contamination from the galactic disc, atmospheric horizon etc.

In <u>both</u> applications minimum obscuration of the sensitive window area and small cross section for scattering (of betas, Compton electrons, gammas and fluorescent X-rays) into the counter are desirable. Angular resolution and background subtraction are often greatly improved by combining results from two or more similar counters with different fields of view.

3.6.1 Collimator Response Function

The collimator response function is the percentage transmission of a parallel beam of photons as a function of the angle of incidence of the beam. It is normally possible to specify a collimator in terms of two <u>independent</u> functions corresponding to directions parallel and normal to the rocket

spin direction, the product of which gives the actual

response for any given pair of "azimuth" and "zenith" angles

respectively. In each direction, the field is determined by

a series of parallel slats or cells, of depth d, and

separation w.
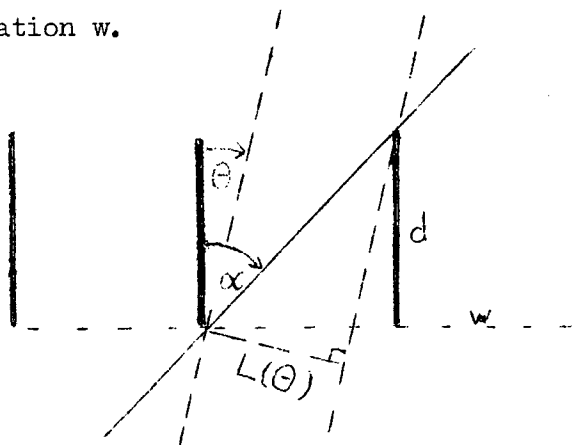
The response function, L (θ), normalized so that L = 1 at

θ = 0, is

$$L(\theta) \quad = \quad \cos\theta \ - \ \cot\alpha \ \sin\theta \tag{3.30}$$

For small θ, L(θ) is adequately described by a simple

triangular response

$$L_\triangle (\theta) \ = \ 1 \ - \ \theta/\alpha, \tag{3.31}$$

in which case, α, given by

$$\tan \alpha \ = \ w/d \tag{3.32}$$

is the **full width at half maximum** (FWHM) of the response.

Table (3.7) gives the percentage deviation of the area under

L(θ) from that under $L_\triangle (\theta)$, as a function of α.

TABLE 3.7

DEVIATION OF COLLIMATOR RESPONSE FROM A TRIANGLE

Triangle FWHM α (degrees)	$\dfrac{\text{Area (L)} - \text{area (L}\Delta)}{\text{area (L}\Delta)}$ (%)	
2.5	(+)	.01
5		.06
10		.25
20		1.03
40		4.27
80		20.19

In all situations of interest here, the rocket precession period is much greater than the spin period (table 2.1). In these circumstances, and for a constant spin rate, the shape of the count rate profile on any one scan or spin across a source is identical in shape to the collimator response function in the spin direction (i.e. with FWHM $\simeq$ α_s), allowing for statistical variations in the number of collected photons.

In a <u>slowly spinning rocket</u> ($\varphi \sim 0.1$ rev sec^{-1}), a typical $\alpha_s = 4^\circ$ implies that a source is seen for about 0.1 seconds on each scan, compared to a single telemetry channel sampling time of .0125 seconds. Thus the telemetry has negligible influence on the resolution and signal to noise ratio. Since the rocket can precess 10° in the time between

successive scans of a source, α_p ($\simeq$ FWHM normal to the spin direction) is made large, of the order of $30\text{-}40^\circ$. Then for accurate source intensity and position to be determined, the source must give a statistically significant response on each of a number of successive scans. The data analysis involving α_s, α_p and rocket attitude solution is described in (5.2.3). The large α_p minimizes the effect of error in the attitude solution (normally $2\text{-}5^\circ$).

For a __spun up rocket__ ($\varphi \sim 3$ rev sec^{-1}) a source is seen for only .004 seconds per scan with $\alpha_s = 4^\circ$. To obtain a statistically significant result of comparable sensitivity the responses on a number of successive scans must be combined, and this process is assisted by the small precession cone half angle. On the other hand, in order not to degrade the collimator resolution and signal to noise, the telemetry sampling time must be small compared to .004 seconds (which is equivalent to that obtained with 3 telemetry channels). With restricted telemetry channels and an uncertainty in the actual spin rate, some resolution and signal to noise degradation is unavoidable. Figure 3.6 shows the effect of telemetry sampling time t_T ($= 1/80$ sec for one channel) on collimator response function represented by $t_c = \alpha/\varphi$. The integrated response curves represent a large number of superposed scans (non synchronous with the telemetry switch), for $t_T/t_c = 0.1, 0.5, 1, 2$. In practice α_p is again made
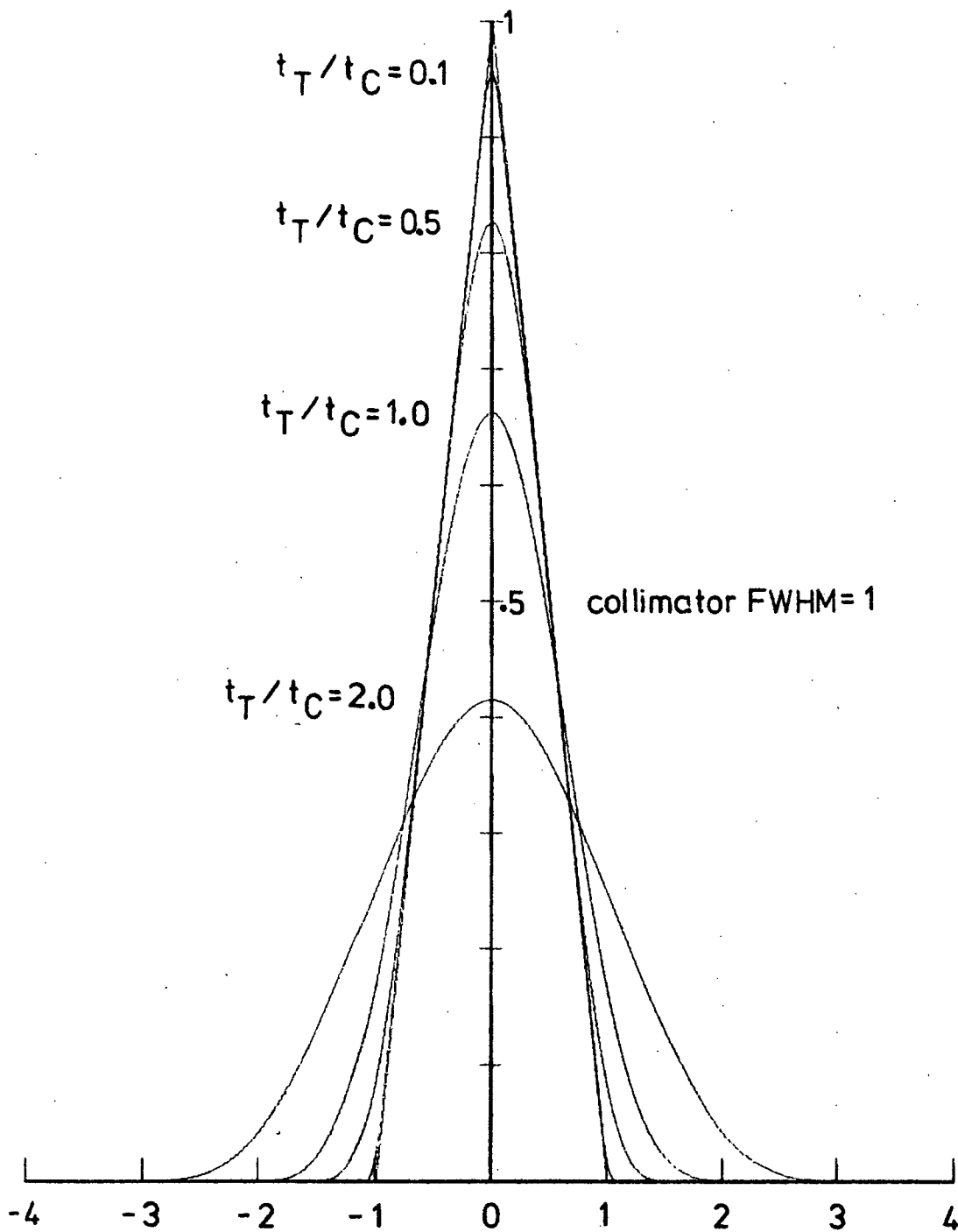
FIGURE 3.6: Effect of Telemetry Sampling Rate on Collimator Response to a point source, for collimator FWHM = t_C = 1 and telemetry sampling rates t_T = $0.1t_C$, $0.5t_C$, t_C, $2t_C$.

large so that the summing of responses on successive scans

is not critically dependent on attitude solution, and also

to allow a reasonably large sky area to be scanned. This

gives rise to difficulties in interpreting the "zenith"

angle of the source and a different field of view (of

different extent, or orientation) must be used.

The discussion has so far been restricted to

rectangular fields of view with

(a)   a direction of maximum response normal to the spin

axis OX (also to the window), and

(b)   the longer field direction aligned with the spin axis,

defining a <u>vertical</u> collimator.

Different fields of view on flights IV-VI are obtained with

a <u>diagonal</u> collimator in which (a) holds but the long field

direction is at $\delta = 30^{\circ}$ or 45° to OX. When used in

conjunction with a vertical collimator, the source zenith

angle is determined in an identical fashion to that employed

for the sunslits of 2.4.5, using equation (2.4). To obtain

intensity information from the diagonal slit alone requires

knowledge of the response in the spin direction now given by

$$L(\theta) = 1 - d\,\tan\theta\left[\frac{\sin\delta}{w_p} + \frac{\cos\delta}{w_s}\right] + \left[\frac{\tan^2\theta\,\sin^2\delta\,\cos\delta}{\tan\alpha_s\,\tan\alpha_p}\right]$$

reducing to (3.30) for $\delta = 0$,

(Mr. A. Broderick, private communication) plus knowledge of

the response function in the long field direction, i.e.

α_s, rather than α_p.

As well as the normal vertical and a diagonal collimator, flight VI has a <u>tilted</u> collimator. This is a vertical collimator with the direction of maximum response tilted $20°$ towards OX, permitting an extension of the sky area surveyed and also contributing to source "zenith" determination. The normal vertical data reduction technique is applicable.

The long rectangular field of view is generally not suited to diffuse X-ray measurements because of ambiguities in photon origin. The collimator determined sensitivity to diffuse X-rays is now discussed.

3.6.2 Collimator Geometric Factor

The geometric factor used here refers to an effective solid angle for the collimator and is measured in steradians. The response of a counter to an incident X-ray flux is the sum of identical responses determined by the many individual cells comprising the collimator so that the geometric factor of an average cell is the same as that for the whole collimator (ignoring edge effects). For one cell the counts C_{cell}, due to an isotropic flux of I_0 photons $cm^{-2} sec^{-1} ster^{-1}$ is obtained by integrating the projected area, solid angle product $(\delta a . \delta \omega)$ for each incident direction, within the limits determined by α_s, α_p, so that

$$C_{cell} = I \int \int \delta a \; \delta \omega$$

The <u>geometric factor</u>, Ω, is defined by

$$\Omega = \int\int \delta a \delta \omega / a \qquad (3.33)$$

where **a** is the normal cell area. Thus for a total unobscured
(normal) window area A (cm^2),

$$C_{total} = I\ A\ \Omega\ counts\ sec^{-1}. \qquad (3.34)$$

The geometric factors of rectangular and square section boxes
have been studied and documented by cosmic ray physicists
using meson telescopes (e.g. Stern, 1960). The results for
a number of UAT collimator configurations are shown in
table 3.8 and were obtained from a program developed and
kindly lent by Mr. D.J. Cooke.

TABLE 3.8

EFFECTIVE COLLIMATOR SOLID ANGLE

Response Function		α_s x α_p	Geometric Factor
α_s	α_p	(steradians)	(steradians)
10°	10°	.0304	.0305
20°	20°	.1219	.1231
(T8) $3^o24'$	$34^o48'$	.0381	.0393
(NC) $4^o12'$	$33^o00'$	.0420	.0435
(Honeycomb) 4.7^o circular			.0054

These are compared with the simple approximation (for α_s,
α_p in radians),

$$\Omega \simeq \alpha_s \alpha_p \qquad (3.35)$$

showing that (3.35) is accurate to better than 3-4% for all
cases. Also included in table 3.8 is the geometric factor

of a cylindrical cell, applicable to honeycomb collimators used in some UAT flights. For this case Ω is given in terms of the radius r, and diagonal length g, and depth d, by

$$\Omega = \pi \left(\frac{2r}{g + d}\right)^2 \qquad (3.36)$$

(Henry et al, 1970).

3.6.3 Reflection, Scattering, etc.

The index of refraction of solids for X-rays is less than unity, so that from an optical standpoint, <u>total external reflection</u> will occur for incident angles (measured between the beam and surface) less than some critical angle ξ_c. Experimental evidence (Hendricks, 1957, Reiser, 1957) is reasonably well described by theory where ξ_c is determined by the real index of refraction $\{\xi_c \sim (h\nu)^{-1}\}$, and the sharpness or width of the fall from zero to total reflection is increased by large absorption in the medium (determined here by the photo electric absorption coefficient). Aluminium has smaller ξ_c values at a given energy than most common metals and has been used almost exclusively here. The values of ξ_c for thick evaporated films of aluminium at energies used by Hendricks and Reiser are shown table 3.9. In practice the efficiency of reflection at angles less than ξ_c is very much dependent on the surface structure. For the evaporated Al films used by Reiser, reflection efficiences greater than 90% were

measured. However the efficiency will be greatly decreased

by using normal commercial sheet, and measurements on the

sheet employed in the UAT collimator have not yet been

carried out.

TABLE 3.9

CRITICAL ANGLES FOR TOTAL REFLECTION (ALUMINIUM)

Photon Energy (keV)	Critical Angle (degrees)
1.49	1.03 (H)
5.43	0.30 (R)
8.04	0.24 (R)

H - Hendricks (1957).   R - Reiser (1957).

Scattering of low energy X-rays by the collimators

is described by a non relativistic limit of the Compton

scattering (see equation 3.25). In classical Thomson

scattering each electron scatters independently. The

relative intensity removed from an incident beam Io (keV

cm^{-2} sec^{-1}) and scattered into a solid angle $d\Omega$ at mean angle

ξ is

$$\frac{d(I)}{Io} = (7.93_{10}-26 \ N.Z) \ sin^2\xi \ d\Omega \, dx \qquad (3.37)$$

where Z is the atomic number, and N the number of atoms per

cm^3 in a thickness dx of scatterer. {In heavier elements

and at longer wavelengths the electrons do not act

independently and scattered photons can be in phase

effect to be considered, i.e. the <u>increased window thickness</u>
for large incidence angles. For a 40G propafilm window the
transmissions at 1.5keV for incident photons at 0°, $\alpha_s = 4^o$
and $\alpha_p = 35^o$, are .576, .575, .510 respectively; above 3keV
the corresponding variation in transmission is less than 1
percent. Integrated over all possible incidence angles, the
spectral distortion is small.

CHAPTER FOUR

UAT DETECTOR DESIGN AND PRE-FLIGHT CALIBRATION

4.1 INTRODUCTION

Chapters 2 and 3 have summarized the design
considerations imposed by the rocket, and the requirement of
good proportional counter action, respectively. Having once
determined a basic proportional counter configuration (e.g.
gas, EHT, anode diameter, anode-cathode spacing), it has been
employed with only slight modifications to each of the
situations encountered, by paralleling separate units to most
efficiently use the space available. (Thus the different UAT
counter designs are labelled according to the rocket site for
which they were originally designed, see section 2.2).
Construction techniques inevitably influence counter
behaviour, and mechanical details of the various counter
types are discussed along with tests verifying their
effectiveness, in this chapter.

The term detector is used to describe the counter plus
its associated electronics, both imposing limitations on
knowledge that can be gained from the incoming radiation. A
basic electronics system with features common to all UAT

flights is described, and calibration techniques are

established which are applicable to all detectors to verify

their correct operation and allow correct interpretation of

their data. The chapter concludes with a discussion of

peculiarities in the performance of multi-anode counters

without continuous anode-isolating baffles (th T8 counters).

4.2   COUNTER MECHANICAL DESIGN

Figure 4.1 schematically summarizes the main

differences between the various counters. The relative cross

section dimensions are shown to scale, with the length of the

gas volume indicated in brackets. LND refers to the commercial

counters of flights I and II, and refurbished for use in

flight III; BR to the UAT counters in base rings of III and

IV; NC to nose-cone counters of IV and V and T8 to the

counters in type 8 bays in V and VI. In the nose cone space

of flight IV, scaled down 6-anode and 4-anode versions of

the illustrated 8-anode NC counter were also employed. The

collimator slats are shown in each case (correct depth but

arbitrary spacing) to indicate the direction of view. Filled-

in circles are used to indicate X-ray detecting or X-anode

positions and open circles the guard or G-anode positions.

The dots in the T8 counter represent grounded wires used to

define a "wall-less" cathode about each X-anode (see section

3.5.5); in the LND counter they represent field forming electrodes described in (3.1.6) and discussed below.

Construction details are summarized in Appendix C, including integration into the rocket and mechanical tests. The general features of the counters are illustrated in the photographs of Appendix D.

4.3   FLIGHT ELECTRONICS

The basic logic of the electronics used in UAT flights has remained unchanged throughout. Figure 4.2 summarizes the main features for a typical situation including anti-coincidence background rejection and four channel pulse height analysis. The circuits are discussed below with brief mention of the peculiarities on each flight. The most notable development has been the introduction of integrated circuits into the flight IV (NC), V and VI electronics.

4.3.1 Power Converter

The 26-27 volts from the rocket batteries (section 2.5) operates an oscillator (at 7.5 kHz in I, II, III, IV (BR) and 3-4 kHz in IV (NC), V and VI) which drives a number of transformers. The square-wave transformer output is rectified and stabilized at the following voltages;
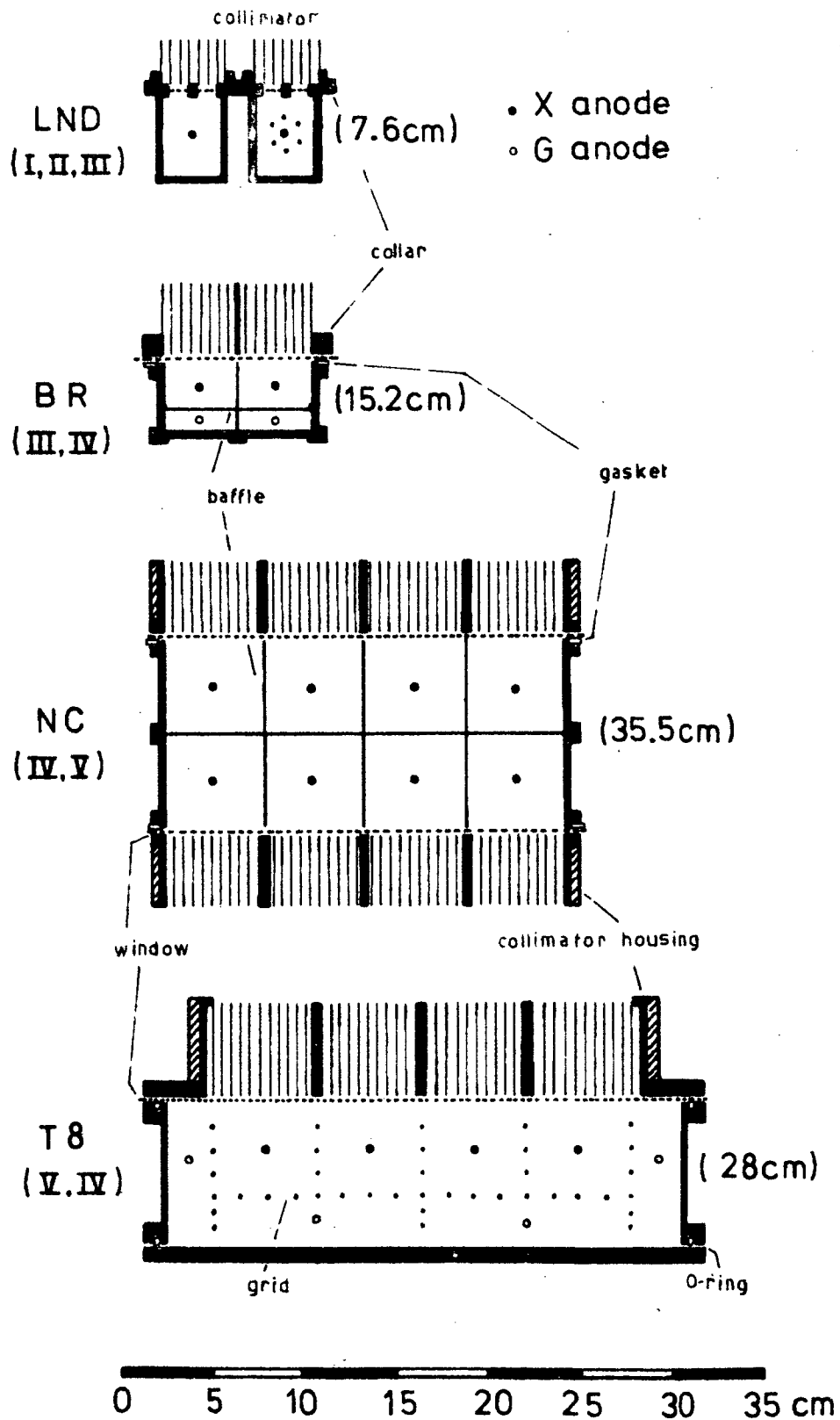
**FIGURE 4.1:** Cross Section and Dimensions of UAT Proportional Counters
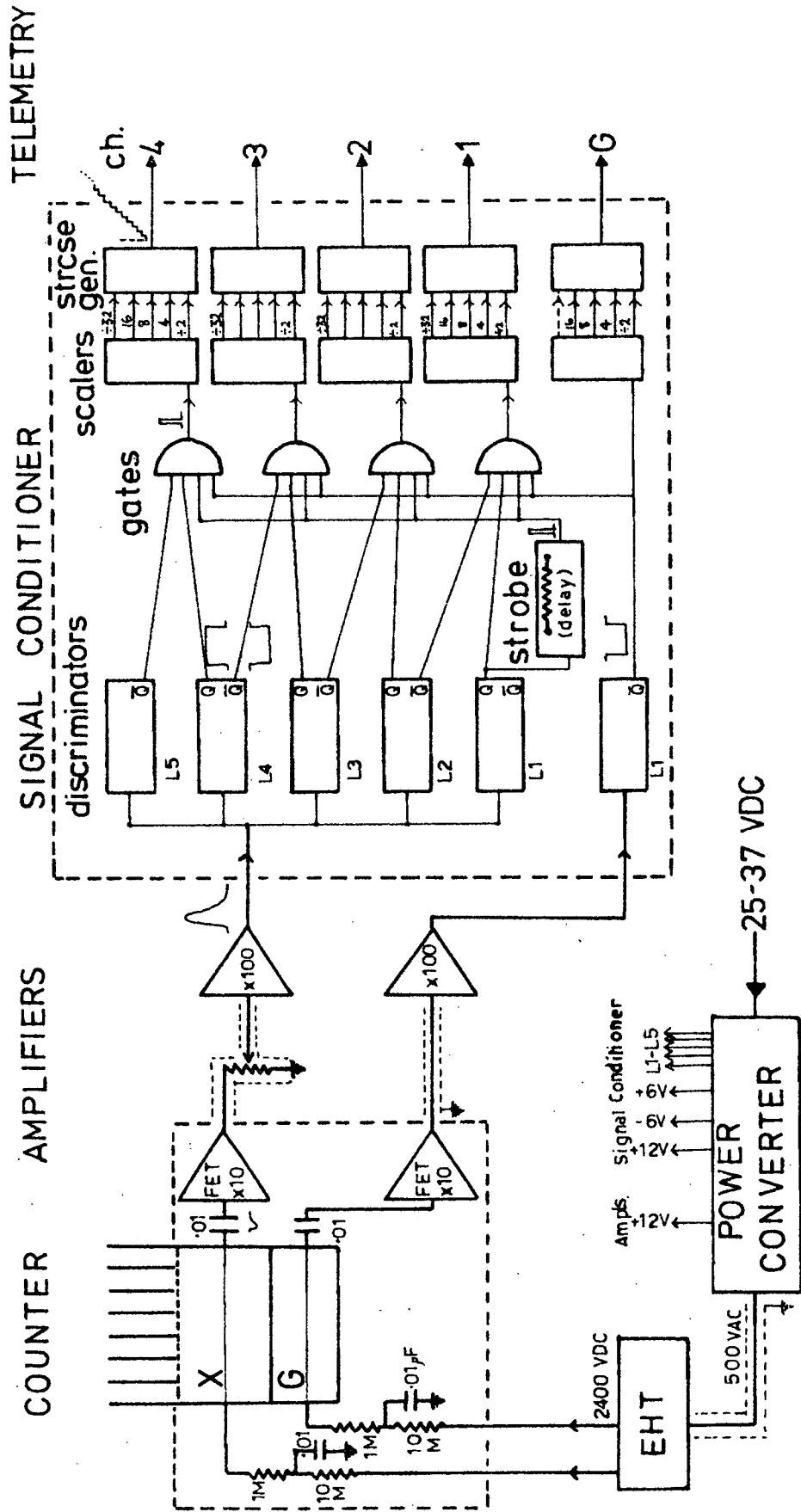
FIGURE 4.2: Block Diagram of Typical UAT Electronics

(1)   + 12 VDC and -6 VDC supplying amplifiers,

discriminators and staircase generators. Typical current

drains are of the order of 100mA;

(2)   + 6 VDC for the logic (scalers, gates etc.), and also

supplying bias levels, L1 to L5 in this case, via adjustable

potentiometers. Transistorized logic current drains were

typically 200mA; for the integrated circuits a +5 VDC supply

with less than 0.1% variation for current drains between 0

and 1.2A is employed.

A high voltage square wave, 500 to 1000 VAC peak to peak, is

used directly from a transformer for EHT generation. In V

and VI, the EHT is supplied from a completely independent,

stabilized oscillator.

4.3.2 EHT Supply

The 500-1000 VAC from the power converter winding is

fed through shielded cable into a Cockroft-Walton voltage

multiplier, comprising a diode-capacitor chain which

rectifies, and multiplies a positive DC component to about

3000 volts. The 3000 VDC is filtered with one or more RC

networks (e.g. series 3MΩ, .01μF to ground), and regulated

to 2400 VDC using a corona tube. Under normal circumstances

the proportional counter draws negligible current (usually

less than 10^{10} electrons per second), and a heavy RC filter

of three series 20MΩ, .01μF networks is used on the corona

output to minimize transient variations.

4.3.3 Counter Connections

The counter connections are illustrated in figure (4.2). The 2400 VDC from the EHT generator is led to the counter, through sealed copper tubing in IV (NC), V and VI, and is distributed to each independent anode through a 10MΩ, .01μF RC _filter_, plus a _load_ resistor (1MΩ on I - IV (BR), 100K elsewhere). The output pulses are taken from the anode via a .01μF, 3kV <u>coupling capacitor</u>. The components and leads at EHT are potted and/or sealed in end compartments.

The four stages of filtering have an overall time constant approaching 20 seconds or so. However when the load current gives a small perturbation persisting for a time short compared with the time constant of an individual stage (e.g. as occurs when a counter scans over the sun) the recovery time to an acceptable voltage level is primarily determined by this last stage, i.e. with time constant 0.1 secs.

4.3.4 Amplifiers

In flights I-IV(BR), an <u>FET input</u> pre-amp and main-amp were in a single shielded can, connected to the counter output by a short length of co-axial cable. In the more recent packages, the pre-amp resides in counter end compartments. The <u>pre-amp</u> has a diode protected input to guard against FET damage due to large pulses (e.g. <u>counter breakdown</u>).

Negative going input pulses of the order of 1-5mV, with
approximately 0.5μsec rise times, are accepted from the anode
and amplified by a factor of about 10. Pulse shaping and
fine gain control (accessible from outside the rocket in more
recent flights), are provided between the buffered pre-amp
output, and the main-amp. The latter has a gain of about 100
and produces positive going 0.6V output pulses, from a very
low output impedance. Course gain control is attained by
altering negative feed-back resistors in both pre- and main-
amp. The noise level due to the pre-amp varies from one FET
to the next, and is usually equivalent to an energy deposition
in the counter of much less than 100eV. Overall gain is
relatively independent of temperature and supply voltage
variations.

4.3.5 Signal Conditioner

The amplifier output from the "X-amplifier", is
paralleled into a number of (in this case 5) discriminators.
In I to IV (BR) each discriminator comprised a Schmidtt
Trigger followed by a mono-stable circuit, elsewhere an
integrated circuit μA702 is used. Each discriminator is
biased with independently adjustable, stable levels
obtained from the power converter. These range from
L1 $\simeq$ 0.75 V (corresponding to 1.5keV, with Fe-55 calibration
X-rays peaking at 3V at the amplifier output) to L5 $\simeq$ 5V

$d(I)/I_o$ then has a Z^2 dependence}. Two points are of

·relevance. Firstly the ratio of cross section for Thompson

scattering to that for photoelectric absorption in

aluminium is small ($\sim 10^{-2}$ at 10keV decreasing with energy to

$\lesssim 10^{-4}$ at 1keV). Secondly the number of photons scattered

at small angles, as required to enter the window, is

governed by the $\sin^2 \xi$ term. Thus even with intense solar

fluxes ($\sim 10^4$ - 10^5 photons $cm^{-2} sec^{-1}$ above 1.5keV), the

number of X-rays scattered into the counter is small

compared with direct cosmic fluxes.

Two other effects must be considered here. The first

is <u>transmission through the collimator material</u> which is

made thin to minimize window obscuration. Typical aluminium

slats are .023 cm thick so that for 8° incidence ($\simeq 2\alpha_s$, and

typical worst case for transmission of one slat aligned with

the spin axis) the transmission at 10keV is <.01% (figures

3.3 - 3.4). For the slats parallel to the spin axis,

corresponding incidence angles approach 70° ($\simeq 2\alpha_p$) and the

10keV transmission is 20%. Because of the small subtended

window area (~ 0.3), relative infrequency of 10keV photons

compared to lower energies, and rapid improvement in

absorption with decreasing energy (i.e. the last figure can

be compared with $\sim 1\%$ at 5.5keV), the influence on overall

spectrum is usually negligible. This suggests the last

(10keV), and are spaced to suitably distribute the number of
expected counts from a typical source over the 4 energy
channels determined. The discriminator outputs, $\bar{Q}$ (normally
1) and Q (normally 0), change states the moment a pulse
exceeds the bias level, and are maintained in the unstable
state for a relatively long time ($\sim 12\mu$s in I-IV (BR), 4-5μs
in IV(NC) - VI), compared with the pulse rise time.

Double differentiation of the Q pulse from the lowest
level (L1) discriminator produces a narrow strobe pulse,
which can be delayed from the initial triggering time by an
amount determined by a resistor in the differentiating circuit.
(Delays of $\sim 8\mu$sec were used with the slow rise time amplifiers
of I - IV(BR), and 2-3μsec delays are used in the more recent
electronics). The strobe pulse event can also be vetoed by a
$\bar{Q}$ from a single guard counter discriminator biased at L1.
Thus the delay fills two functions, it allows the X-input
pulse to reach its peak before sorting, and it allows for
variations in the relative arrival times of pulses from the
X and G anodes, due to a single charged particle. Such
variations arise as a result of the finite drift times of
electrons into the avalanche regions of the counter.

The number of X-pulses in an energy channel with
limits determined, for example, by bias levels L2, L3, is
counted at the output of a "NAND" gate which samples the L2Q,
L3$\bar{Q}$, guard $\bar{Q}$ and strobe, and gives a detectable output when it

4.3

receives all 1's, i.e. a change of state of L2Q <u>and</u> strobe,

but <u>not</u> the $\bar{Q}$'s.

The gate output is fed into a chain of n <u>scalers</u>, and

the output state (0 or 1) of each scaler is fed into a

resistive network or <u>staircase generator</u>. Thus n scalers

produce 2^n analogue levels at the staircase generator output

such that 2^n successive pulses from the gate step the staircase

in an orderly manner through one complete cycle of analogue

levels. The extreme analogue levels are adjusted to lie

within the $\pm$ 3V telemetry limits, and are prevented from

exceeding these by zener diodes. A buffered staircase output

is sampled directly by the telemetry. This produces an upper

limit on the count rate that can be recorded, i.e. less than

about 2^n counts per telemetry sample. From section 2.7 it is

seen that n = 5 for a -3 to +3V staircase, gives the greatest

number of steps which can be individually and independently

identified on the photographic flight records. In the flight

IV (NC) electronics, access to a telemetry synchronization

pulse permitted the scalers to be reset after each sampling,

and produced a direct count rate against time profile on the

records.

4.4   PRE-FLIGHT CALIBRATIONS

It is obviously extremely difficult to predict
accurately the behaviour of proportional counters constructed
and operated under conventional tolerances. Great emphasis
is therefore placed on extensive laboratory calibration of
counter and electronics to establish the ranges of correct
action and to document behaviour outside these ranges.
Limited in-flight calibration is reserved for the more
critical parameters governing laboratory behaviour, and is
discussed for each flight in the next chapter. The results
of pre-flight calibrations, quoted here, are applicable to
all UAT counters unless otherwise stated.

The calibration techniques have rested heavily on two
items. The first is iron-55, a radioactive isotope of 2.9
year half-life, which decays by internal conversion to give
manganese K X-rays. The K α X-rays, of mean energy 5.895keV,
dominate the spectrum providing a convenient "mono-energetic"
source (see figure 4.3a). Figure 4.3(b) shows the percentage
absorption for 5.9keV X-rays as a function of gas depth,
related to the situation in a T8 counter (i.e. for P-10 at
1 atmosphere, 20°C). The second item is the multi-channel
pulse height analyser (pha). In Tasmania calibrations are
done with a Nuclear Data 1024 channel analyser. The pha
input accepts 0 to + 10 volt pulses, compatible with the
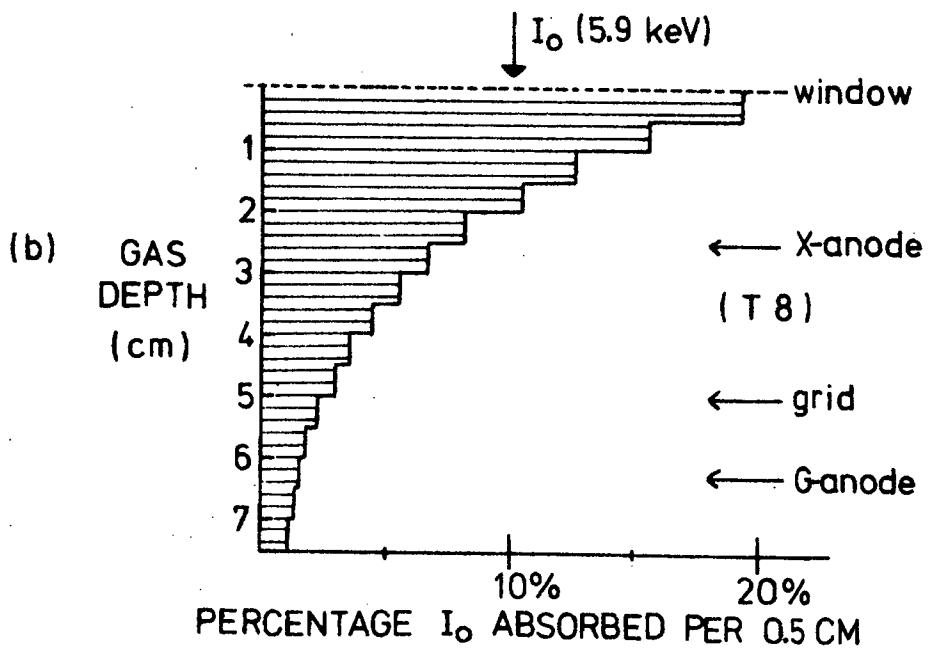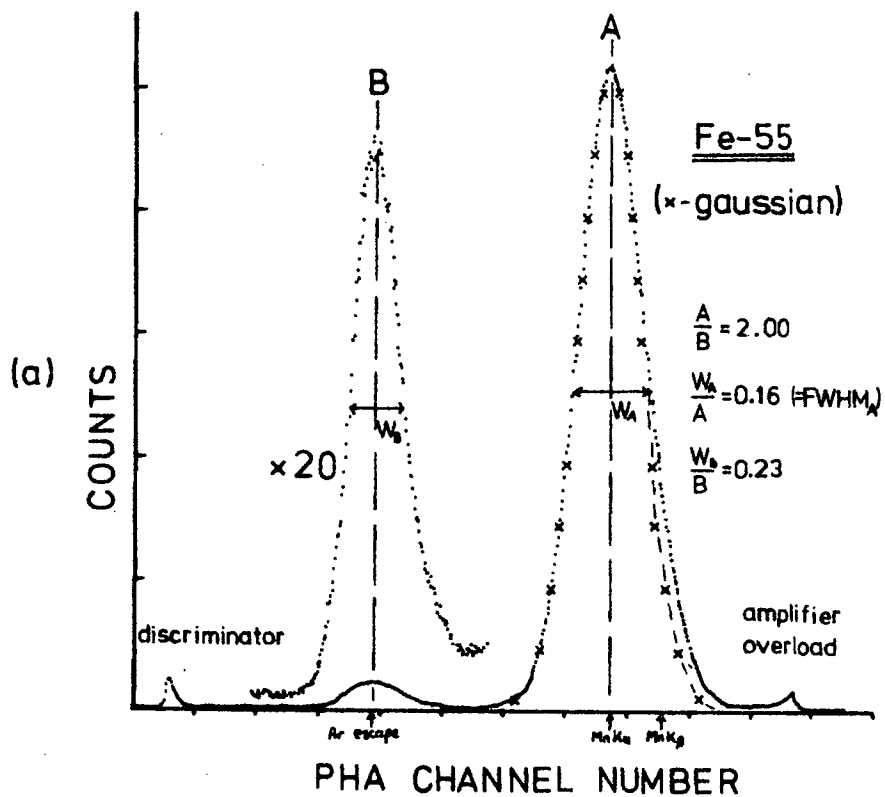
FIGURE 4.3: (a) Response of Proportional Counter to Fe^{55} X-rays
(b) Absorption of Fe^{55} X-rays in Counter as a function of Gas Depth

amplifier outputs. The pulse height is determined at a change

in sign of the pulse slope so that linearity is relatively

insensitive to pulse risetime. The quoted integral linearity

is better than $\pm$ .075% over the top 99% of full scale. The 0

to 10 volt pulses can be sorted into 128, 256, 512 or 1024

channels. An anti-coincidence facility is one of many aids to

pulse counting and is discussed further in 4.4.7. Output

devices include oscilloscope, point plotter and teletype. In

Adelaide, and at Woomera, a portable 400 channel TMC analyser,

with similar pulse requirements has been employed.

4.4.1 Proportionality

In a P-10 filled counter, the Fe-55 spectrum gives an

immediate indication of proportionality, due to the escape

peak phenomenon discussed in 3.1.1. The figure 4.3(a) pulse

height spectrum shows two peaks, the smaller one resulting

from the absorption of a 5.90keV X-ray followed by the escape

of an argon K α X-ray of 2.96keV, i.e. resulting in a 2.94keV

deposition in the gas. The two peak heights should then be in

the ratio 2.01 : 1, implying that the multiplication process

is linear for incident X-rays of energies $\lesssim$ 6keV.

Two other situations require investigation; one for

X-ray energies $>$6keV and the second for X-rays, particularly

the low energy ones, which may be absorbed in a region of

weak or distorted field (in corners immediately below the

window, for example). To do these, long lifetime radioactive

sources have been used to excite characteristic line

radiation from a range of thin absorbers. A 5 mCi Fe-55

source and an extended similar strength Am-241 source have

provided the exciting radiation. However this extremely

convenient technique becomes inefficient for characteristic

energies much less than the fixed excitation energies, and a

conventional X-ray tube has been employed to obtain line

emissions $<$2keV, see section 5.4. Table 4.1 summarizes the

range and origin of readily available calibration lines.

Figure 4.4 illustrates the T8 proportionality over a

wide range of photon energies. Some of the data were collected

by Mr. Luyendyk and all have been measured with respect to the

Fe-55 radiation, permitting normalization of the various

results; error estimates are of the order of the spot sizes.

The only noticeable deviation from linearity occurs at the

high gas gains (high EHT) and high photon energies. For

example at 2400 volts, when from table 3.1 the gas gain is

$\sim$10^4, non linearity appears at about 10keV in excellent

agreement with the Hanna criterion, equation (3.9), and

indicating the onset of space charge effects.

Only counter IV - NC-C has exhibited significant non

proportional behaviour below 10keV and this was deliberately

introduced in order to have sufficient gain to observe

$\sim$0.28keV X-rays with existing amplifiers. The counter

TABLE 4.1

CALIBRATION PHOTON ENERGIES

Principal Energy (keV)	Associated Energies (approx.intensity) keV		Origin	Excitation
27 - 37	120%	60	Am^{241}	
14.4	100%	β,γ's	Co^{57}	
11.91	<10%	13.28	$_{35}Br(K)$	Am^{241}
8.04	<10%	8.91	$_{29}Cu(K)$	Am^{241}
6.40	<10%	7.06	$_{26}Fe(K)$	Am^{241}
5.90	<10%	6.49	$_{25}Mn(K),(Fe^{55})$	
3.69	<10%	4.01	$_{20}Ca(K)$	Fe^{55}(5 mCi)
2.98	<40%	3.2	$_{47}Ag(L)$	Fe^{55}
2.94			$Mn(K)-Ar(K)$	Fe^{55}(Ar counter)
2.29	<40%	2.5	$_{42}Mo(L)$	Fe^{55}
1.49	<10%	1.55	$_{13}Al(K)$	(Fe^{55}), tube
.282			$_{6}C(K)$	tube
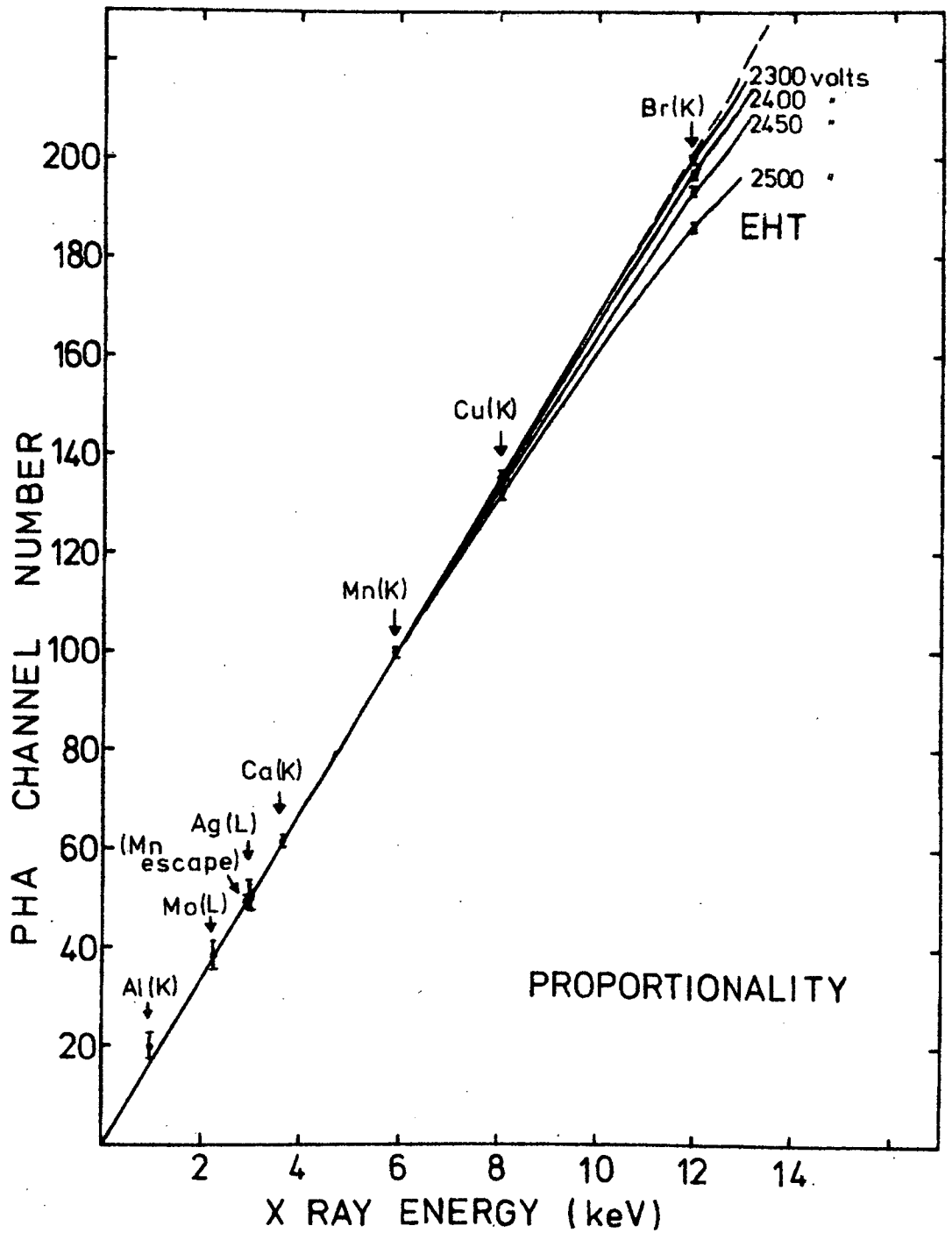
FIGURE 4.4: Pulse Height versus X-ray Energy for T8 Counter

operated in a region of "limited proportionality" above
3keV.

4.4.2   Energy Resolution

The intrinsic energy resolution of a proportional
counter is discussed in 3.1.4. Section 3.1.6 lists the
factors which in practice degrade this resolution. A typical
pulse height spectrum is shown in figure 4.3(a) for a narrow
collimated beam of Fe-55 X-rays. The FWHM (5.9keV) of the
main peak (at A keV) is 16%. The crosses have been
calculated for a gaussian curve with standard deviation
σ = A.FWHM_A/2.36 = 0.40keV, showing excellent agreement with
the left hand side of the pha peak and clearly indicating the
Mn Kβ contribution on the right hand side. (By using finer
collimation and careful selection and cleansing of an anode
wire, FWHM (5.9keV) $\simeq$ 14.5%, in agreement with equation 3.13,
have been measured).

In practice, the integrated response for X-rays over the
total window area, combining all anodes is used. This is a
variable, depending on the cleanliness of the anodes etc. and
is measured prior to launch by continuously accumulating
counts while a source is moved at a constant rate along each
anode wire. FWHM in the range 16% - 20% have been measured
with the T8 and NC counters. Apart from the Mn Kβ effect
the curves are well represented by gaussians and the

resolution degradation within this range has very little

influence on the quality of spectral data, particularly for

continuous source spectra.

With the Be windowed III-BR counter best integrated

resolution was FWHM (5.9keV) $\simeq$ 25%, the high value being

attributed to field distortion near the window due to the

supporting mesh, as suggested in the previous subsection.

The variation of resolution with photon energy is

shown in figure 4.5, using data obtained for figure 4.4.

The "best resolution" for a P-10 counter, equation 3.13,

is shown as a dotted line. The experimental points were

obtained with only loose control over the irradiated window

area, background count rates etc. No systematic variations

in resolution are apparent over the 2300 to 2500 volt EHT

range and the data agree adequately with a $h\nu^{-\frac{1}{2}}$ dependence.

4.4.3 End Effects

In collecting the data above, due care was taken to

avoid irradiating the ends of the counters where fields are

obviously distorted. In order to define suitable sensitive

areas, end effects have been studied and the results for a

T8 counter are shown in figure 4.6. The relative positions

of end wall and insulators etc. are shown in (a), and (b),

(c) and (d) show the count rate, gain and energy resolution

as a function of distance from the end wall for a normally
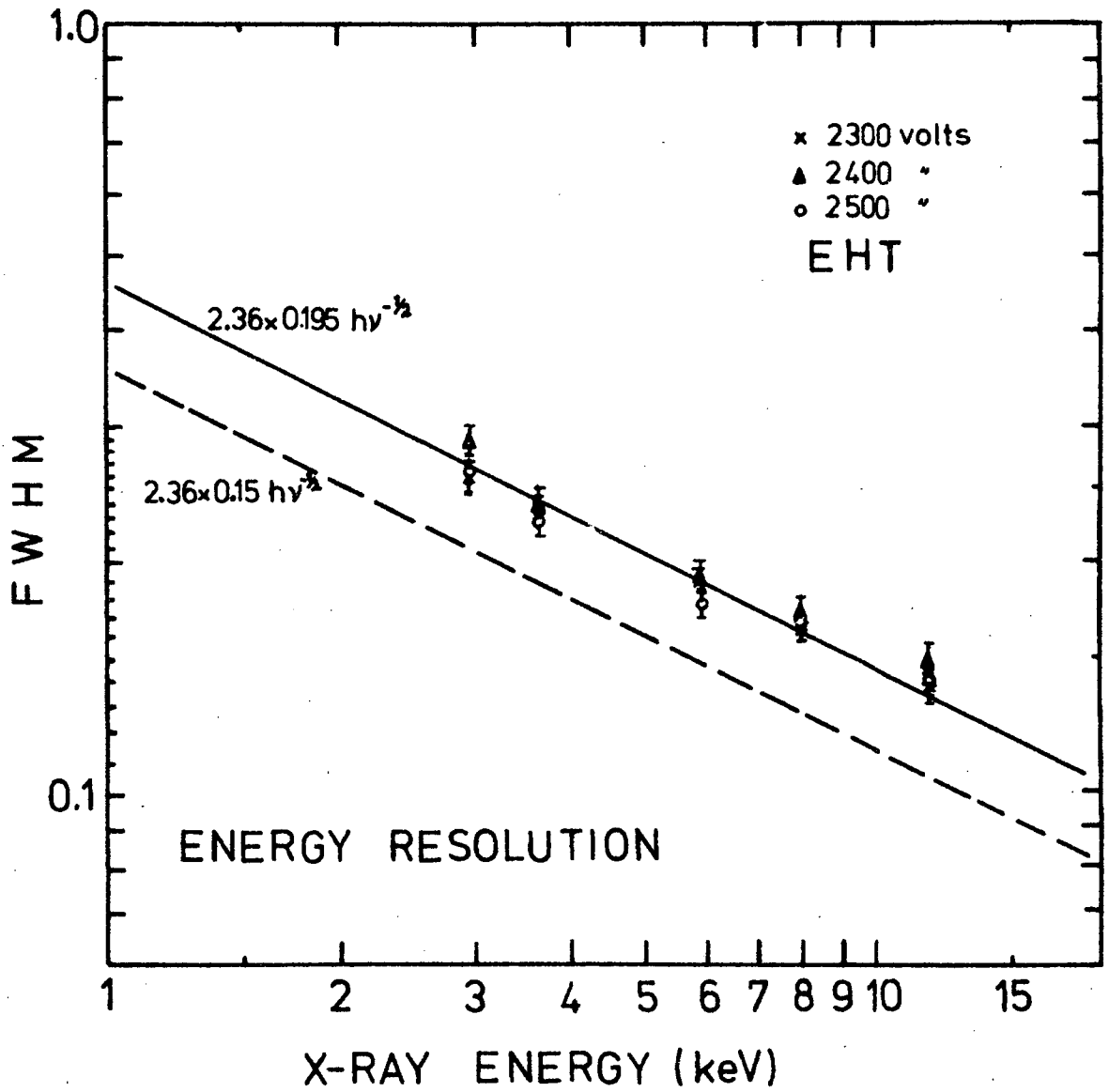
FIGURE 4.5: Energy Resolution (FWHM) versus X-ray Energy for T8 Counter
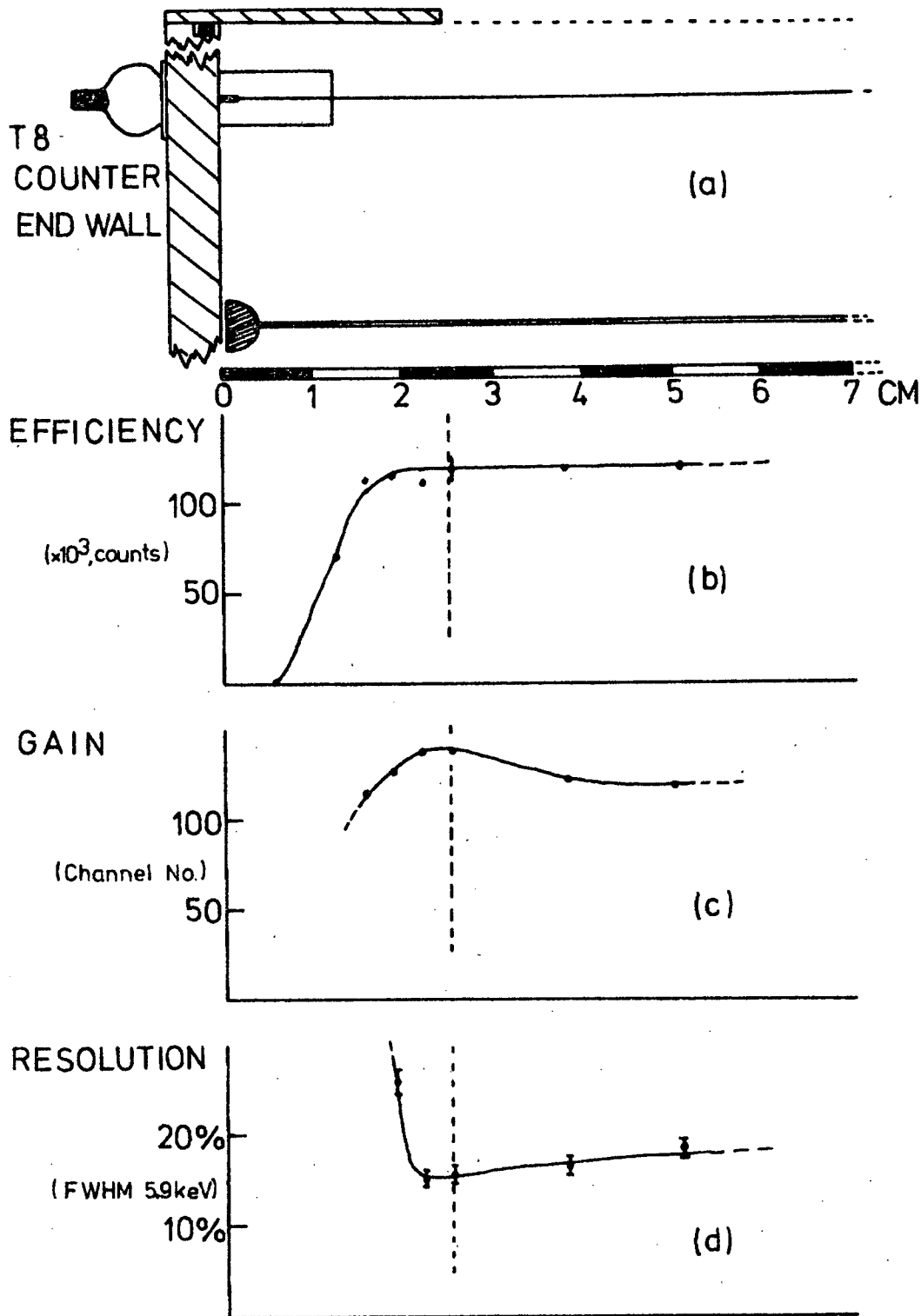
FIGURE 4.6: End Effect in T8 Counter of Cross Section (a).
(b) is Count Rate, (c) Gain and (d) Resolution,
as function of separation from the End Wall.

incident collimated Fe-55 X-ray beam. Generally the area

extending to 2.5 cm from the end wall (i.e. to the dashed

lines) is masked.

4.4.4 Count Rate Effects

Saturation effects in both counter (3.1.6) and

electronics can distort measured spectra. The gain and

resolution for a T8 counter, plus laboratory amplifier, are

shown in figure (4.7) as a function of count rate. The

measurements were made using the 5 mCi Fe-55 source

suspended some 30 cm above the exposed window (no

collimator). The count rate variation was obtained by

gradually interposing absorbing sheets. The dashed line

represents the count rate expected from a normally incident

source with <u>twice</u> the 1.5 - 15 keV intensity of Sco XR-1. At

this count rate the 4% gain decrease, and resolution change

from 19.5% to 27%, are tolerable.

The laboratory amplifiers, with pulse lengths $\sim 20 \mu$sec,

obviously dominate these curves. The absorption of a single

5.9keV photon produces an avalanche charge $\simeq 4_{,0}-13$ coulombs,

which is dissipated here with a time constant 0.1 sec, compared

with the static charge per anode of $\sim 2.4_{,0}-8$ coulombs. Any

small space charge effect will be even smaller at the typically

lower cosmic photon energies. The flight amplifiers for the

large T8, NC counters are faster (pulse length $\sim 8 \mu$sec) and in
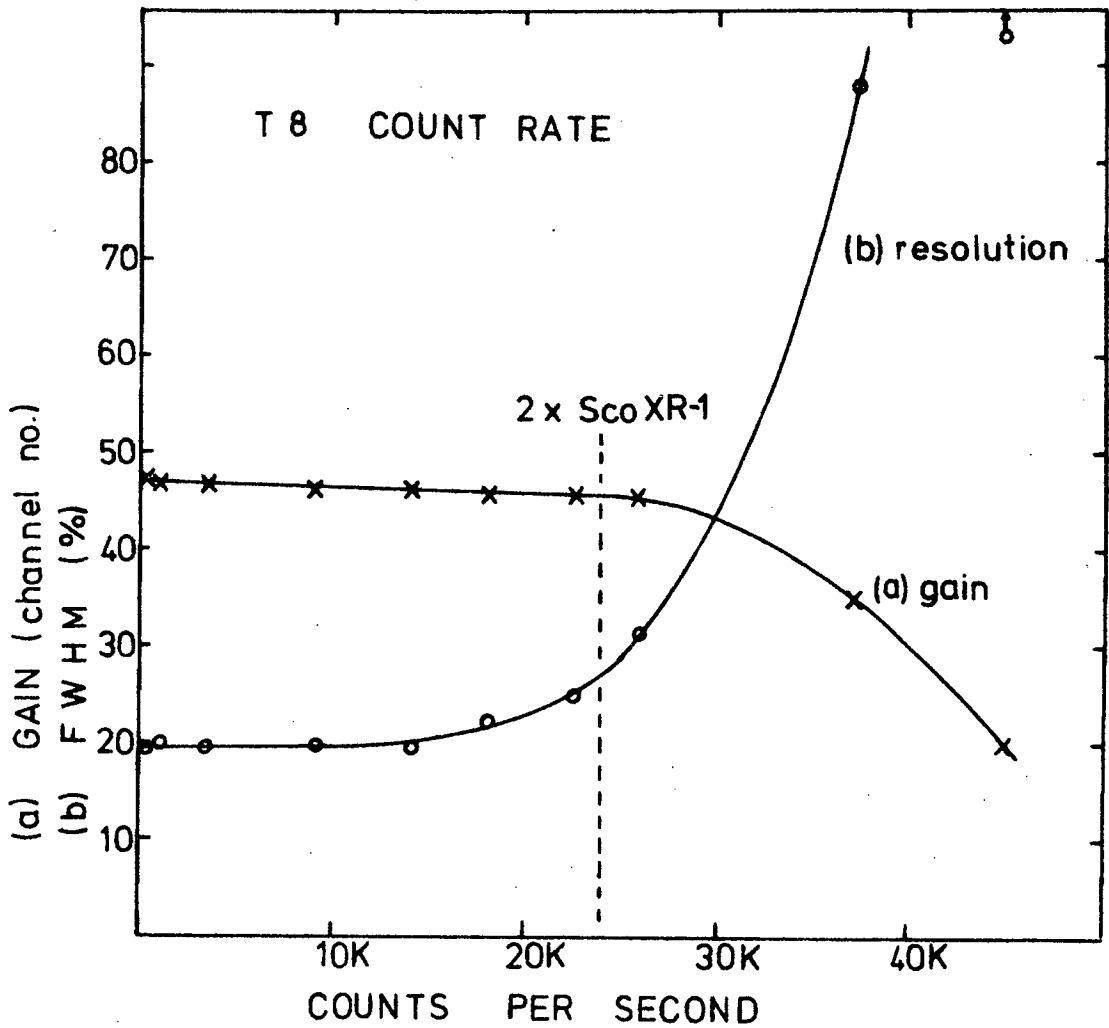
FIGURE 4.7:   Effect of Countrate on (a) Gain, (b) Resolution
(FWHM 5.9 keV), in a T8 Counter plus Amplifier.

any case a source at normal incidence would be expected
relatively infrequently. Overall, for sources with intensity
$\leqq$ Sco XR-1 there will be negligible count rate effect. (An
EHT effect which persists after a very high count rate was
mentioned in 4.3.3).

4.4.5 Lifetimes

The stability of counters in both laboratory (or
launcher) and vacuum environment is important. The word
"lifetime" is associated here with the time for a 10% decrease
in gas gain of a counter in the "sea level" environment.
Finite laboratory lifetimes are a result of gas contamination
by electronegative gases (mainly O_2, H_2O) and obviously
varies from counter to counter and with the climatic
conditions. With the large plastic window T8 and NC
counters lifetimes of the order of 6 hours are common and
anything less than this has prompted leak testing and
resealing.

Where gas gains have been monitored under vacuum
conditions, counters with the best laboratory lifetimes show
very little ($\ll 5\%$) change over 5-10 minutes (representing
the flight duration). Others exhibit an increase in gain
indicating a decrease in pressure (table 3.1) and thus
undetected leaks from the gas volume. Emphasis is placed
on in-flight calibration of this critical factor.

4.4.6 Collimators

Section 3.6.1 discusses the techniques used to correct data for collimator response function and to determine the relative source intensity throughout a flight. To determine the absolute source intensity it is also necessary to know accurately the collimator obscuration when the maximum number of photons is being transmitted (usually when the incident beam is normal to the counter window). With large areas of multi-cell collimators used here, it is extremely difficult to correct for such effects as buckling, burred edges, dust and slight misalignment from cell to cell etc, and direct calibration is highly desirable.

The attenuation length of 5.9keV X-rays in air (N.T.P.) is ~36 cm, indicating the difficulties involved in calibrating with perfectly collimated X-rays. An optical method has been devised to measure both the shape and area of a collimator response function, neglecting possible X-ray scattering (see 3.6.3). The contributions of Mr. Tuohy and Mr. Broderick who carried out many of the calibrations of flight collimators and introduced a number of sophistications in lining up procedures, are acknowledged, and the latter's results are quoted below.

The experimental set up is schematically represented by figure 4.8(a). A point light source is placed at the
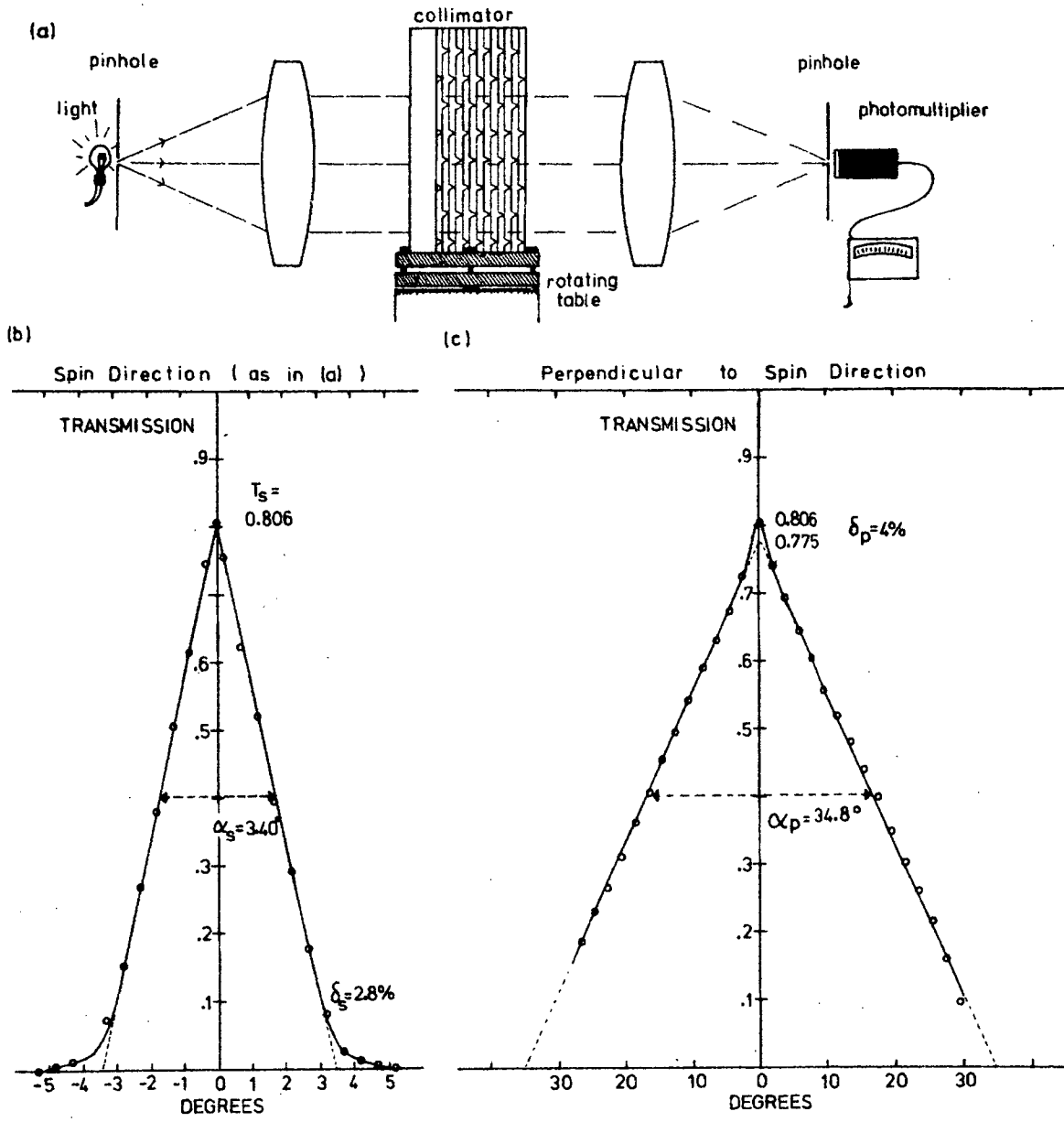
FIGURE 4.8: Collimator Calibration. (a) Experimental Set-up, (b) Response of Vertical Collimator in Spin Direction, (c) Response of Vertical Collimator Normal to Spin Direction.

focus of a 15 cm aperture lens, using a telescope focused
at infinity to determine the point of focus. Measurements
on the "parallel" beam using a screen, typically show a
divergence of much less than 20 min of arc. The collimator
is mounted on a horizontal rotating table, calibrated in
parts of a degree. Fine adjustment of the table "tilt"
permits accurate alignment in both horizontal and vertical
axes. The light passing through the collimator is collected
by a second similar lens and focussed through a pin hole
onto the photo cathode of a photo multiplier, (whose output
is proportional to the light received). Light reflected
from the collimator slats, which might normally invalidate
the calibration, can no longer reach the pin hole. Other
sources of diffuse light are equally well suppressed by the
lens system. The accurate alignment of the whole system
is greatly facilitated using a laser beam and pin hole
apertures at front and back surfaces of each lens.

Figures 4.8(b),(c) give results for a T8 vertical
collimator. The data points are normalized to maximum
transmission values obtained from the measured values by
correcting for reinforcing slats or bars included in the
circular light beam area during measurement. Dashed lines
are the triangles of best fit, used for analysis purposes.
In the spin direction, the FWHM and maximum transmission
(T_s) of the triangle are indicated, along with δ_s defined by

$$\delta_s = \frac{\text{area triangle} - \text{area measured response}}{\text{area triangle}} \tag{4.2}$$

The FWHM of all large detection systems described in the next chapter have been obtained in this fashion, and the T_s, δ_s values are incorporated in the calculation of effective window areas. Thus the response in the spin direction gives a measure of source intensity modified only by the relative response of the collimator in the perpendicular direction.

The triangle of best fit to the measured response in the perpendicular direction gives a FWHM 34.8°, but the maximum triangle ordinate underestimates the source intensity by $\sim 4\%$ (largely due to the contribution of the V shaped indentations, Appendix C3. It is convenient to introduce

$$\delta_p = \frac{\text{max. ordinate triangle} - \text{m.o. measured response}}{\text{m.o. triangle}} \tag{4.3}$$

δ_p must be clearly distinguished from δ_s. For example in the case of a rocket motion with negligible precession cone, δ_s would be applied to the integrated response in the spin direction if the 3.4° FWHM triangle was used in fitting this response. On the other hand there is no necessity to use a triangle approximation to the perpendicular response (unlike the case for a large precession cone requiring least squares fitting in this direction). Thus in a spun up round δ_p is probably not required.

In section 5.5, the results for the more unusual diagonal and tilted collimators are discussed.

4.4.7 Background Rejection Efficiency

There are three factors which can change from payload to payload and which influence the efficiency of rejection of non X-ray events in an X-counter operated in anti-coincidence with a guard. The first is the geometry of the anti-coincidence arrangement, discussed in 3.5.5 and governing the rejection of penetrating charged particles passing through both counters. The second relates to a non penetrating component discussed in 3.5.2, and influenced by the distribution of mass in and around the counter. The final factor is the ability of the electronics to recognise and veto non simultaneous but related events, as required by the finite electron drift times in a proportional counter.

The first two factors are not independent and with no certain knowledge of the non X-ray radiation composition during flight it is very difficult to predict performance. What can be done is to subject counters to selected laboratory radiations and compare the laboratory performance with in flight data, as a step towards predicting future flight performances. Preliminary laboratory data are reported here and in the next section, in anticipation of flight V and VI results which will contain information on all three of the X, G, and veto rates for these counters.

The data were collected using a "blocking" facility on the Nuclear Data pha. Every pulse to be analysed is

automatically delayed ~ 1.25 μsec, whereas the block or

guard pulses have no delay and persist for a time long

compared with the maximum electron drift time in a counter.

For an electron drift velocity given by, (see 3.1.3),

$$v \; = \; 4\sqrt{X/P} \; \text{cm}(\mu\text{sec})^{-1}$$

this is

$$T_{max} \; = \int_0^{2.5} \frac{dr}{4\sqrt{X/P}} \; \simeq \; \frac{1}{6} \; \left(\frac{P \ln b/a}{V_a}\right)^{\frac{1}{2}} \left[r^{3/2}\right]_0^{2.5}$$

In a typical counter $T_{max} \simeq 1.5$ μsec but may be longer in

the guard counters due to longer drift paths and distorted

field. (Measurements with a collimated beam of β's from

Sr^{90} in the particular T8 counter discussed below indicated

occasional delays of around 2-4 μsec in the guards). Thus

these measurements may tend slightly to underestimate the

rejection efficiency, but will suffice to illustrate the

effectiveness of the rejection measures.

Using a NC counter (similar to that in figure 4.1, and

representing all UAT counters with solid separating baffles)

the percentage of <u>laboratory</u> background counts rejected

when one side is used to guard the other were

$$V_{max}(\text{lab.}) \; \simeq \; 47\%$$

$$V_{min}(\text{lab.}) \; \simeq \; 25\%$$

depending on the counter orientation. Maximum rejection is

obtained with one side vertically above the other, in

accordance with the approximate (cosine)^2 zenith angle

dependence of the penetrating component of cosmic rays at

sea level.   To a first approximation the numbers are

compatible with a laboratory background comprising half

this penetrating component, and half non penetrating and

isotropic (see 3.5.2).   When the NC counter is subjected

to a relatively high count rate as a result of irradiation

with gammas (1.3MeV) from <u>Cobalt-60</u>, there is no

appreciable difference with or without the guard connected,

consistent with the counts being due to Compton electrons

scattered from the walls.   It is reasonable to assume that

the non penetrating component of the laboratory background

has a similar nature.

Similar tests were made on a T8 counter like that in

figure (4.1) except that, to facilitate construction, the

three pairs of grid wires separating the four guard anodes

were omitted.   The directional sensitivity of the system is

expected to be appreciably reduced by the three sided geometry

of the guard.   Figure (4.9a) shows the X-count rate as a

function of pulse height due to Co^{60}.   When the guard is

connected (veto) around 75% of the total X-counts (no veto)

are rejected.   In figure (4.9b), this rejection efficiency

is shown per 10 channel (∼1keV) interval for Co^{60}, Am$^{2\,41}$

and laboratory background.   The americium is a source of

60keV and ∼30keV gammas and the poor rejection efficiency is

(a)

T 8-4
COBALT-60

no veto.

veto

Fe-55

COUNTS (/4000sec)

15000

5000

10 30 50 70 90

(b)

T 8-4

Co⁶⁰

Lab. bg.

Am²⁴¹

REJECTION EFFICIENCY (%)

100
90
80
70
60
50
40
30
20
10
0

10 30 50 70 90

CHANNEL NUMBER
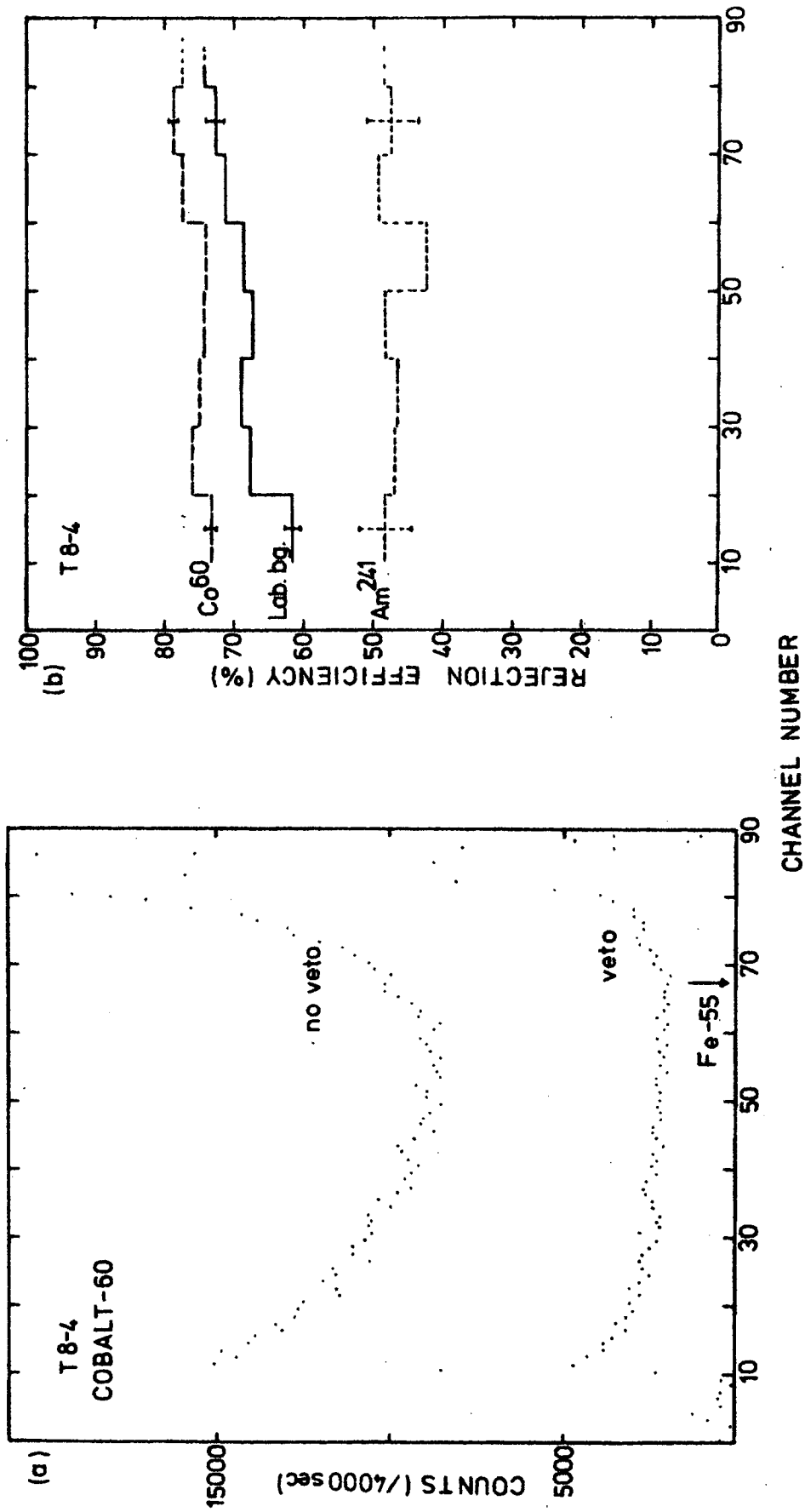
FIGURE 4.9: Background Rejection in T8-4.
(a) Count Rate versus Pulse Height for Co⁶⁰.
(b) Rejection Efficiency versus Pulse Height
    for Co⁶⁰, Am²⁴¹ and Lab. background.

a consequence of the short range of electrons ejected by these gammas.

Despite the marked improvement from the NC case, the overall rejection efficiencies are less than expected in view of the improved geometry for the penetrating particles (from 3.5.5 $V_{cr} = 0.93$) and great reduction of matter about the main X-counter, even taking the electron drift times into account. Also the similar rejection efficiencies for the background and Co^{60} indicate either that the background comprises mainly gammas, in conflict with the NC results, or that the penetrating component, in particular, is not being rejected as efficiently as expected. The reason for the discrepancy is interpreted in terms of "dead" regions in the guard, and is discussed along with other properties of the T8 counters in the next section.

4.5   WALL LESS MULTIANODE (T8) COUNTERS

The design philosophy for the T8 counters is discussed in section 3.5.2 and its effectiveness is partly illustrated above; in brief, in order to minimize the production of background pulses in a counter, the mass surrounding the sensitive volume must be kept small. The properties of a proportional counter are relatively insensitive to cathode configuration and, for example, Charpak et al (1968) have

investigated a row of adjacent, independent anode wires
between two flat cathode planes, and obtained good
proportional counter properties on each anode. In the T8
counters the requirement for identical gain on neighbouring
X-anodes is important if the anode outputs are to be
paralleled and retain good energy resolution. Thus to
reduce cathode mass and obtain electrical independence of
neighbouring X or G anode compartments in these counters,
each X-anode is surrounded on three sides by widely spaced,
grounded, wire grids (and on the fourth by low mass windows).
The number of particles produced in the mass about the
counter which interact with the X gas volumes without also
passing through a G volume, is very small.

The choice of cathode wire separation was made after
a comparison of counter behaviour with anodes (between two
cathode planes 5 cm apart) separated by 0, 1, 2, 3 wire
grids and by solid baffles successively. These tests were
carried out by Mr. Luyendyk who reported that the
demarkation between adjoining sensitive volumes became
slightly ill-defined with less than 2 wires in the grid;
apart from this and the gain changes, no deterioration of
proportional counter properties were observed. Four wire
grids were chosen as a compromise between low mass and
anode independence.

The performance of a single T8 X-compartment is given
in figure (4.10). A finely collimated 5.9keV X-ray beam was
stepped at fixed height, and known distances from a side
wall, across the X4 compartment shown in (a). The area,
peak position and FWHM (5.9keV) of the X1 pulse
distributions at each position give the relative efficiency,
gain, and the energy resolution of the counter, as shown in
(b), (c) and (d) respectively. The count rate (relative
efficiency) curve varies from about 10% to 90% of its
maximum value in a distance of 0.35 cm, which is also the
maximum divergence of the collimated beam in the gas volume,
and the integrated response is not significantly different
from that obtained for solid baffles. Both gain and
resolution data are similar for the solid baffle case. The
importance of a neighbouring field in defining the sensitive
X1 volume is illustrated by the curves corresponding to a
scale measure $>$ 9 cm, which pass through measurements
obtained from X1 but with the high voltage removed from X2.
While the detection efficiency remains relatively constant
well into the X2 compartment, the increasing effect of
recombination is illustrated by the decreasing gain and
deteriorating energy resolution.

A noticeable feature in figure 4.10(b) is the uneven
count rate "plateau" across the X1 sensitive volume. The
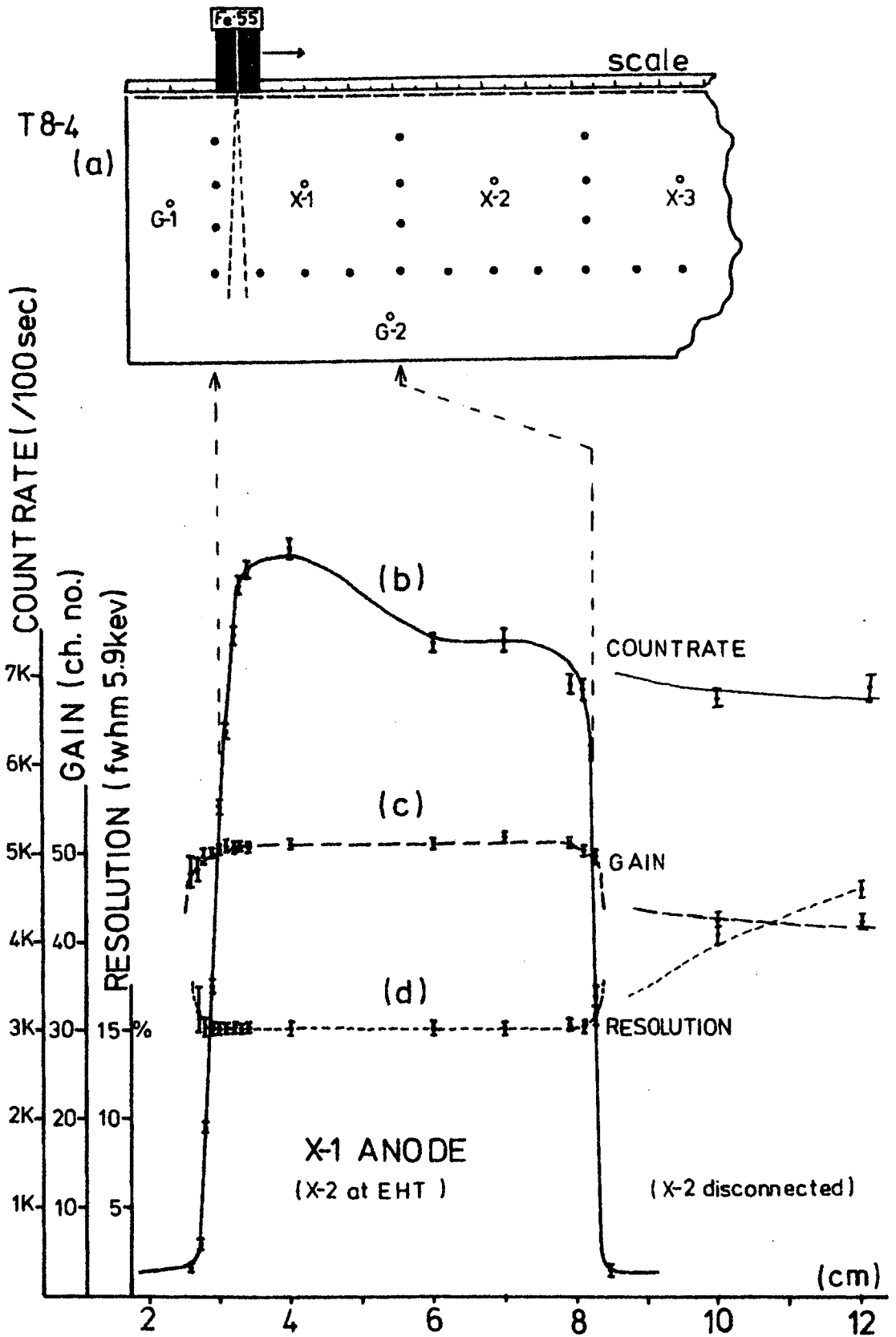
FIGURE 4.10: Performance of Single T8-4 X-Compartment (a) Cross Section. (b) Countrate, (c) Gain, (d) Resolution versus Scale Reading.

shape of the curve was found to be related to guard anode

position in counters with cathode grid configurations as

shown in (a). Figure 4.11(a) shows count rate versus

source position for a traverse across the whole width of

the counter. The peaks are thought to be due to photons

absorbed in regions of weak guard fields where the electrons

released are influenced by the X-anodes and either recombine

or find their way into the X compartments. There may be

some reciprocal effect in the "valleys". Figure 4.11(b)

shows the fall off in field strength (plotted as X/P) with

distance from anode, for two situations representing the

ideal and an approximate actual guard geometry (insets).

For X/P values less than the   P-10 recombination level

(see 3.1.6) we anticipate increasing recombination, or

electron motion in a "perpendicular" field component due

to a neighbouring anode wire.

This phenomenon has two implications on counter

performance, neither very serious. These are

(1) An uncertainty in mean absorption efficiency which

if not taken into account might distort spectra. Once the

"average gas depth" of the X counter is established, for

example by repeating scans at different photon energies,

it can be applied with accuracy to predict source spectra.

Preliminary tests (below) indicate that most "migration"
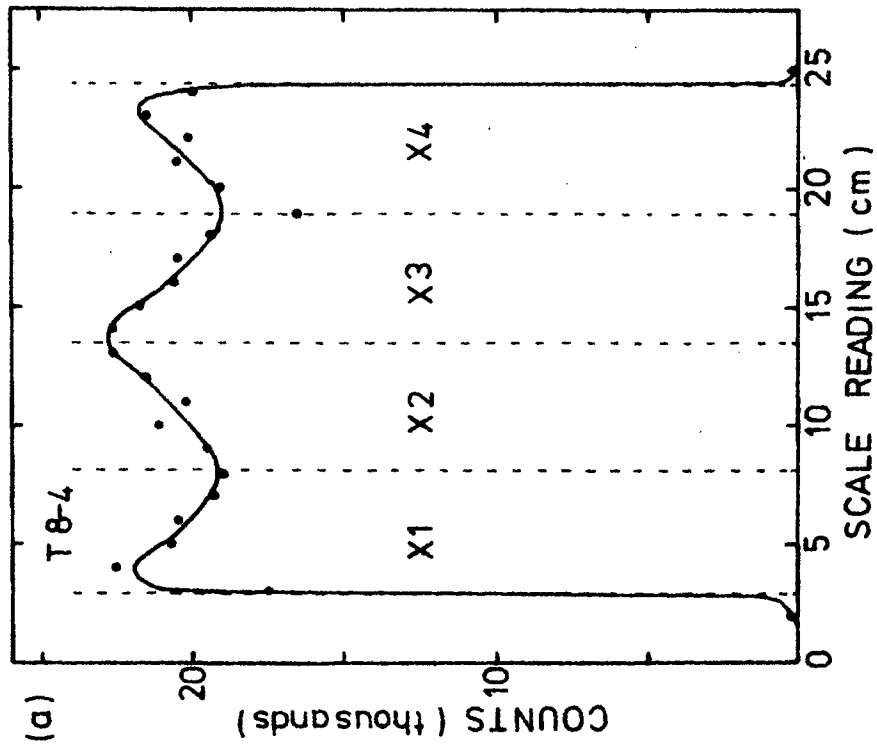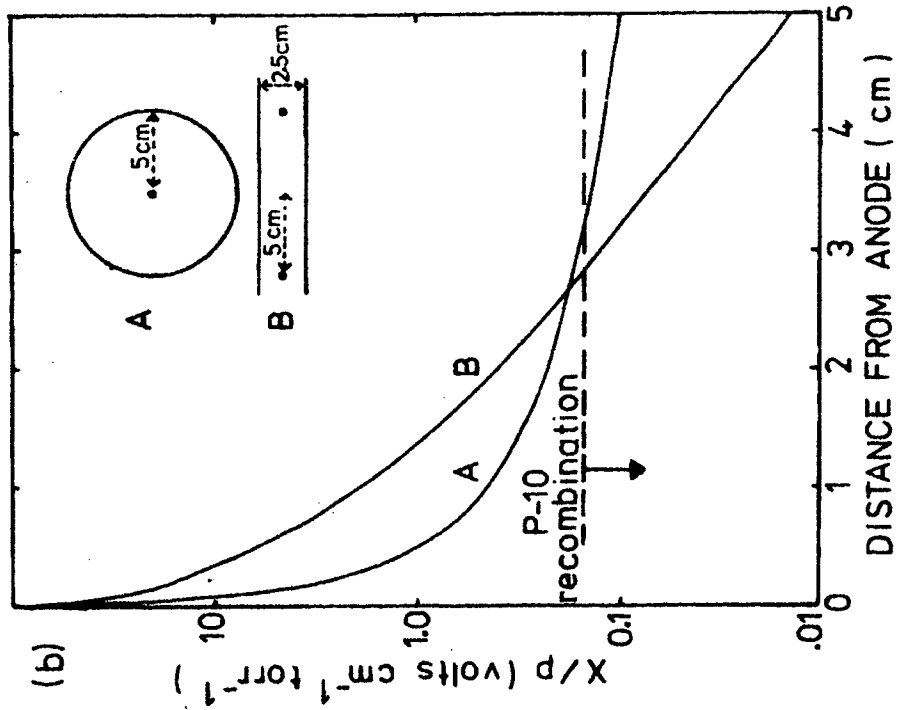
FIGURE 4.11: (a) Countrate Variation across T8-4.
              (b) Field strength (/760 torr) versus Anode Distance
                   for approx. Guard geometries.

takes place from the guards into the X-compartment,
slightly increased efficiency at high energies.

(2)   A reduction in rejection efficiency due to
inefficient detection of charged particles in the guard.

As a preliminary test of this interpretation the T8
counter of the previous section was connected with the G
pulses into the pulse height analyser, using the X-pulses
to veto. From the point of view of Compton scattering this
situation is inferior to the normal one, however if there
are no "dead" regions in the X-counter, an improvement in
rejection efficiency is expected since each charged
particle which passes through both volumes and gives a G
pulse, also gives an X pulse. Rejection efficiencies of
86% of Co^{60} (c.f. figure 4.9) were obtained.

The T8 counter on flight V was similar to the one
described here. On flight VI, grids were included between
the guard wires as shown in figure 4.1, to increase the
guard field strengths. Detailed analysis of the performance
of both counter types, using flight electronics, is
proceeding.

In conclusion, it is anticipated that simple T8
counters will be developed to reject $>$ 90% of the inflight
background over the energy range 1-10 keV, comparable with
best reports using the pulse rise time method ($>$ 3keV), but

without the loss of efficiency which accompanies the latter

technique (see 3.5.5).

TRANSFORMATIONS EMPLOYED IN ATTITUDE SOLUTIONS

Information in flight is gathered
with reference to the rocket axes X, Y,
Z, as in figure (a), and in particular
in flights I and II, with reference to
the -OZ axis. The problem is to obtain
-OZ in space-fixed axes x,y,z as a
function of time (t). It is convenient
to align Oz with the fixed rocket
precession axis in space, and to relabel
the rocket axes x_3, y_3, z_3 with Oz_3
representing the spin axis, as in
figure (b).

The rocket precesses about Oz,
with precession angle

$$\psi = \omega_p t + \Psi \qquad (1)$$

Then, from figure (c),

$$\begin{vmatrix} x_1 \\ y_1 \\ z_1 \end{vmatrix} = \begin{vmatrix} c\psi & s\psi & 0 \\ -s\psi & c\psi & 0 \\ 0 & 0 & 1 \end{vmatrix} \begin{vmatrix} x \\ y \\ z \end{vmatrix} = T_1 \begin{vmatrix} x \\ y \\ z \end{vmatrix}$$

where $c\psi = \cos\psi$ and $s\psi = \sin\psi$.
The spin axis is at angle ρ to the Oz
axis, ρ being the precession cone half
angle. Thus, from figure (d),
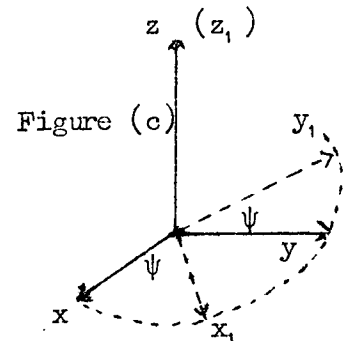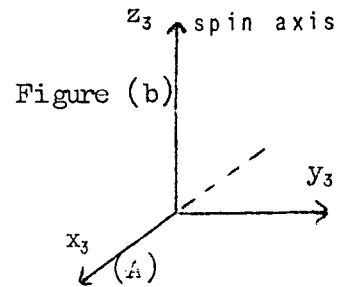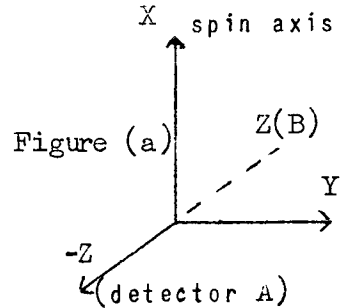
Figure (a)

X spin axis

Z(B)

Y

-Z

(detector A)

Figure (b)

z_3 spin axis

y_3

x_3

(A)

Figure (c)

z (z_1)

y_1

ψ

y

ψ

x

x_1

$$\begin{vmatrix} x_2 \\ y_2 \\ z_2 \end{vmatrix} = \begin{vmatrix} 1 & 0 & 0 \\ 0 & c\rho & s\rho \\ 0 & -s\rho & c\rho \end{vmatrix} \begin{vmatrix} x_1 \\ y_1 \\ z_1 \end{vmatrix} = T_2 \begin{vmatrix} x_1 \\ y_1 \\ z_1 \end{vmatrix}$$

The rocket spins about Oz_3, the spin angle being

$$\varphi = \omega_s t + \Phi \qquad (2)$$

and, from figure (e)

$$\begin{vmatrix} x_3 \\ y_3 \\ z_3 \end{vmatrix} = \begin{vmatrix} c\varphi & s\varphi & 0 \\ -s\varphi & c\varphi & 0 \\ 0 & 0 & 1 \end{vmatrix} \begin{vmatrix} x_2 \\ y_2 \\ z_2 \end{vmatrix} = T_3 \begin{vmatrix} x_2 \\ y_2 \\ z_2 \end{vmatrix}$$

Therefore $\begin{vmatrix} x_3 \\ y_3 \\ z_3 \end{vmatrix} = T_1 \ T_2 \ T_3 \begin{vmatrix} x \\ y \\ z \end{vmatrix}$

Figure (d)

Figure (e)

and $T_1 \ T_2 \ T_3$ is an orthogonal matrix whose inverse is its transpose (T) i.e

$$\begin{vmatrix} x \\ y \\ z \end{vmatrix} = (T_1 \ T_2 \ T_3)^T \begin{vmatrix} x_3 \\ y_3 \\ z_3 \end{vmatrix} = T_1{}^T T_2{}^T T_3{}^T \begin{vmatrix} x_3 \\ y_3 \\ z_3 \end{vmatrix} ,$$

evaluating for $x_3 = 1, \quad y_3 = 0, \quad z_3 = 0$

$$\begin{vmatrix} x \\ y \\ z \end{vmatrix}_{\{precession \ cone \ axes\}} = \begin{vmatrix} c\psi \ c\varphi - s\psi \ c\rho \ s\varphi \\ s\psi \ c\varphi + c\psi \ c\rho \ s\varphi \\ s\rho \ s\varphi \end{vmatrix} \qquad (3)$$

(This is the case for a detector with direction of maximum response along the rocket -OZ, i.e. +Ox$_3$, axis. For directions away from the max. resp. direction, or for detectors with max. resp. in some other direction, the relevant x_3, y_3, z_3 values are inserted here).
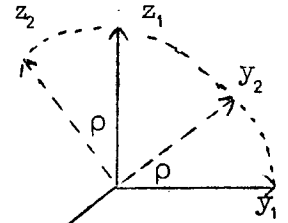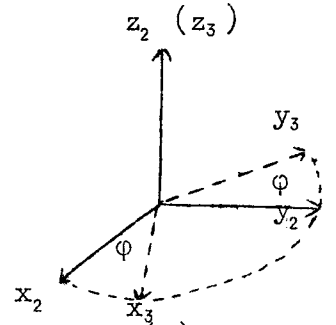
The precession cone axes are transformed into equatorial axes
x', y', z' so that, declination

$$DEC = \text{arc sin} \frac{z'}{\sqrt{(x'^2 + y'^2 + z'^2)}} \qquad (4)$$

and right ascension

$$RA = \text{arc tan } (y'/x') \qquad (5)$$

It is convenient to assign a <u>southerly</u>
direction to Ox precession cone axis
to align Oz with the North celestial pole
a rotation of $(90-\delta)^0$ about Y is required,
where δ is the declination of the
precession cone z-axis (figure f). Right
ascension is measured <u>eastwards</u> from
γ-Aries, requiring a further rotation of
$(-\alpha)$ about the North pole direction, α
being the right ascension of the
precession cone z-axis (figure g). Thus

Figure (f)

$$\begin{vmatrix} x' \\ y' \\ z' \end{vmatrix} = \begin{vmatrix} c\alpha & -s\alpha & 0 \\ s\alpha & c\alpha & 0 \\ 0 & 0 & 1 \end{vmatrix} \begin{vmatrix} s\delta & 0 & c\delta \\ 0 & 1 & 0 \\ -c\delta & 0 & s\delta \end{vmatrix} \begin{vmatrix} x \\ y \\ z \end{vmatrix}$$

or

Figure (g)

$$\begin{vmatrix} x' \\ y' \\ z' \end{vmatrix}_{equatorial} = \begin{vmatrix} c\alpha\, s\delta & -s\alpha & c\alpha\, c\delta \\ s\alpha\, s\delta & c\alpha & s\alpha\, c\delta \\ -c\delta & 0 & s\delta \end{vmatrix} \begin{vmatrix} x \\ y \\ z \end{vmatrix}_{precession} \qquad (6)$$

In flight I it was necessary to rotate the BAC
solution about the sun position, to obtain reasonable
agreement with the known X-ray source positions, in
particular Sco XR-1. The BAC solution consisted of the
RA and DEC of the rocket -OZ, i.e. $+Ox_3$ axis as a function
of time. Thus
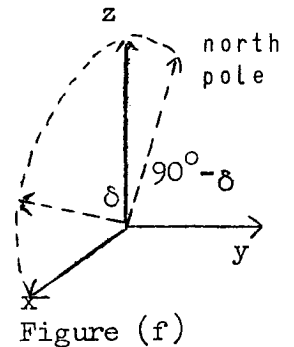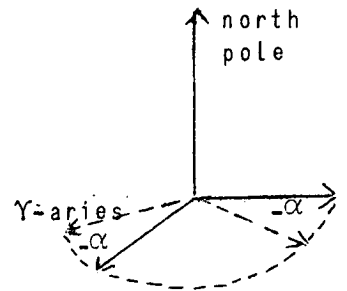
$$x' = \cos DEC \cos RA, \quad \mathring{y}' = \cos DEC \sin RA, \quad \mathring{z}' = \sin DEC \quad (7)$$

To get a co-ordinate system (x_s, y_s, z_s) with the sun at zenith required a rotation of α_s about z' followed by a rotation of $(\delta-90)^{\circ}$ about the transformed y' axis, where α_s, δ_s are the RA and DEC of the sun, thus

$$\begin{vmatrix} x_s \\ y_s \\ z_s \end{vmatrix} = \begin{vmatrix} c\alpha_s & s\alpha_s & 0 \\ -s\alpha_s & c\alpha_s & 0 \\ 0 & 0 & 1 \end{vmatrix} \begin{vmatrix} c(90-\delta_s) & 0 & -s(90-\delta_s) \\ 0 & 1 & 0 \\ s(90-\delta_s) & 0 & c(90-\delta_s) \end{vmatrix} \begin{vmatrix} x' \\ y' \\ z' \end{vmatrix} = T_s \begin{vmatrix} x' \\ y' \\ z' \end{vmatrix}$$

A rotation of Δ about the Oz_s axis,

$$\begin{vmatrix} x_s' \\ y_s' \\ z_s' \end{vmatrix} = \begin{vmatrix} c\Delta & s\Delta & 0 \\ -s\Delta & c\Delta & 0 \\ 0 & 0 & 1 \end{vmatrix} \begin{vmatrix} x_s \\ y_s \\ z_s \end{vmatrix} = T\Delta \begin{vmatrix} x_s \\ y_s \\ z_s \end{vmatrix} \quad ,$$

followed by a conversion of the (x_s', y_s', z_s') back to equatorial co-ordinates gave the desired result, i.e. the corrected equatorial co-ordinates

$$\begin{vmatrix} x' \\ y' \\ z' \end{vmatrix}_{corr.} = T_s^{-1} T\Delta \begin{vmatrix} x' \\ y' \\ z' \end{vmatrix} \quad , \tag{8}$$

where

$$T_s^{-1}T\Delta = \begin{vmatrix} c\Delta + c^2\delta c^2\alpha\Delta' & , & s\Delta s\delta + c^2\delta s\alpha c\alpha\Delta' & , & -s\Delta s\alpha c\delta + c\delta s\delta c\alpha\Delta' \\ -s\Delta s\delta + c^2\delta s\alpha c\alpha\Delta' & , & c\Delta + c^2\delta s^2\alpha\Delta' & , & s\Delta c\delta c\alpha + c\delta s\delta s\alpha\Delta' \\ s\Delta c\delta s\alpha + c\delta s\delta c\alpha\Delta' & , & -s\Delta c\delta c\alpha + c\delta s\delta s\alpha\Delta' & , & 1 - c^2\delta\Delta' \end{vmatrix}$$

$$\tag{9}$$

Δ was varied to obtain best agreement with the Sco XR-1 position, and $\Delta' = (1 - c\Delta)$.

Conversions RA, DEC to new galactic co-ordinates l^{II}, b^{II} and then to the hammer equal area projection used in figures 5.1, 5.2 and 5.4 were achieved using Algol procedures kindly provided by Mr. P.A. Hamilton.

LEAST SQUARES FIT TO A TRIANGULAR RESPONSE

The response function of a collimator in the spin
direction, and the response from scan to scan (involving
both collimator response normal to the spin direction and
the attitude solution), can usually both be approximated
by a triangle. In the latter case it is sometimes
necessary to use a triangle asymmetric about the peak.
The least squares fitting technique, jointly developed
with Dr. Harries, and programmed by the author for the
analysis of flights I and II data, is reproduced in brief
here because of its general applicability.

The digitized data consist of a series of count-rates,
$X(t_i)$ observed at times t_i. If the theoretical response
function is $g(t)$, with $g(0) = 1$, then the theoretical count
rate profile is of the form $Ag(t-t_0)$ where A is the source
strength and t_0 the time of maximum response. In a triangle
of base W1 and W2 as shown, and for $t_0 - W1 < t < t_0 + W2$,
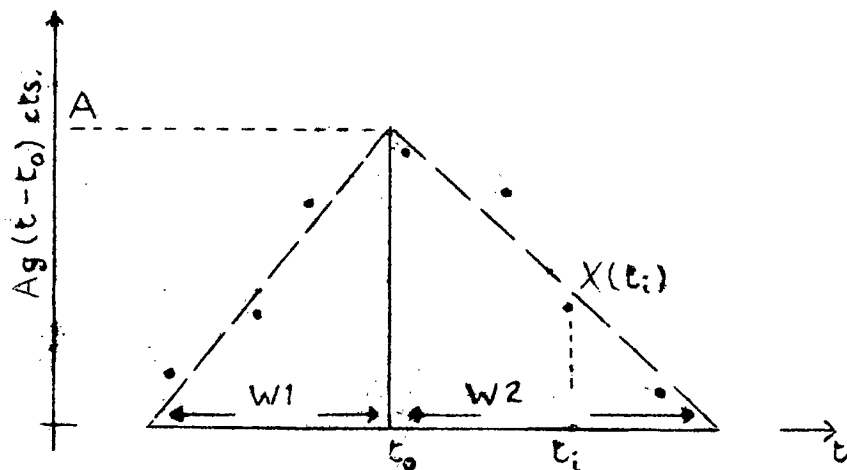
$$g(t-t_0) = (1 - \frac{t-t_0}{W}), \tag{1}$$

where for $t < t_0$, $W = -W1$ and $t > t_0$, $W1 = W2$. (e.g. for the response in the spin direction, $W1 = W2 =$ collimator FWHM).

The least squares method involves minimizing the sum of the squares of the deviations of the data from the response function, i.e. minimizing

$$D = \sum\{X(t_i) - A\,g(t_i-t_0)\}^2 \tag{2}$$

Differentiating (2) with respect to A and solving for $\partial D/\partial A = 0$,

$$A = \frac{\sum X(t_i)\,g(t_i-t_0)}{\sum g^2(t_i-t_0)} \tag{3}$$

and the variance of A is given by

$$V(A) = \frac{\sum g^2(t_i-t_0).V\{X(t_i)\}}{\{\sum g^2(t_i-t_0)\}^2} = \frac{\sum g^2(t_i-t_0).X(t_i)}{\{\sum g^2(t_i-t_0)\}^2}, \tag{4}$$

for poisson distributed $X(t_i)$.

Differentiating (2) with respect to t_0 and solving for $\partial D/\partial t_0 = 0$,

$$t_0 = \frac{1}{N}\{\sum t_i - \frac{W}{A}\sum X(t_i)\} + W \tag{5}$$

where N is the number of data points. Then, as above

$$V(t_0) = (\frac{W}{NA})^2 \sum X(t_i) \tag{6}$$

{in practice, t_0 can be determined by minimizing $V(A)$}.

APPENDIX C

MECHANICAL CONSTRUCTION, INTEGRATION AND
TESTING OF DETECTION SYSTEMS (Chapt. 4)

C1   LND COUNTERS

The most significant experimental results so far
obtained in the UAT rocket program are those of flights I
and II, made with these commercial counters. They were
constructed by LND Incorporated, Oceanside, New York, to
specifications drawn up by Dr. J.R. Harries and Prof. K.G.
McCracken. Since they were designed for a space very much
smaller than that eventually provided by the multipurpose
ring, the counter windows occupied an appreciable part of
the total counter length, with the result that the flight
II data had to be corrected for end-effects. Flight I
counters, constructed at a later date incorporated the
field forming electrodes with partial success; both types
are represented in figure 4.1. The necessary data
corrections for both cases are discussed in (5.2.3).

The counter bodies were milled from solid aluminium
block leaving a wall thickness ~ 0.3 cm. Six apertures
~1 cm x 1.8 cm, with minimum separation 0.25 cm, were
milled from two overlying 0.3 cm thick Al plates which

subsequently formed a "sandwich" around a large, thin
(nominally $5_{10} - 3$ cm) beryllium window. The Be window
frames and body (with anode) were assembled with an epoxy
resin to form a gas tight box. The counters were evacuated,
baked and filled with Xe - CH_4 through a small glass tube,
which was then sealed and potted, in the hope of an
"infinite lifetime".

C2   UAT COUNTERS

General features of some of the counters are illustrated
in figure (4.1) and in the photographs of Appendix D.

In all cases _aluminium_ has been used to form the counter
outside walls. This is chosen because of its low mass,
negligible fluorescent effects, and low cost. The use of
cast aluminium offers considerable freedom and convenience
in matters of construction and mounting etc. however
porosity is a problem, and leaks through as much as 0.6 cm
Al have been detected in "quality" castings for T8 counters.
Porosity problems are avoided by using hard (typically 65S
Alcan) _rolled or extruded_ alloys, but this introduces
problems in making reliable gas tight metal to metal seals.
The use of common epoxy resins is undesirable for two reasons,
(1) they tend to absorb water vapour and re-emit it into
the gas volume (e.g. see Culhane et al, 1966) and (2)
isolated samples have been observed to lose their mechanical
strength after long periods (for reasons which are obscure,
but may be related to incorrect mixing, cleaning solvents,
and/or moderate temperature outgassing etc.). With the
plastic-window flush counters (section 3.2), (1) is
negligible compared to window permeability, and the epoxy
"Araldite" has proved an effective seal in most cases. In

flight V, the NC counter walls have been successfully <u>argon-
arc welded</u> in preference to "Aralditing". Factors dissuading
wide use of this technique relate to difficulties associated
with obtaining welding fluxes suitable for different alloys,
difficulties in welding inside corners, and heat buckling.

In all cases, counter walls have been milled away (to
a minimum of 0.2 cm) to reduce weight and local background
production. It is necessary to leave bolt-hole blocks, and
also <u>reinforcing</u> build-ups to accommodate pressure
differentials described in section 2.7.4. In the very large
NC counters extra measures were required to prevent walls
bulging out in vacuum. These have included firmly aralditing
the centre baffle to opposite side walls, and inserting 0.5
cm diameter steel tensioning rods through the collimators,
immediately above the windows.

Windows, comprising a thin sheet of plastic (or
beryllium pieces araldited to a thin aluminium frame for some
BR counters) have been sealed over counter bodies using both
<u>flat gaskets and O-rings</u>. Limited wall thickness with rolled
or extruded Al have normally provided insufficient space to
include O-ring grooves plus bolt-holes, thus the BR and NC
counters have used Viton A or neoprene, 0.2 cm thick, <u>flat
gaskets</u>. In practice, the gaskets have been susceptible to
damage in the course of changing windows, and unless
contained tightly from all sides, have tended to "creep"
after prolonged use under pressure. No such problems are
encountered with O-ring seals on the T8 counters, and the
freedom to use O-rings on these cast bodies has largely
outweighed problems associated with porosity. 4BA bolts
spaced every 4 cm or so are used to pull a solid metal plate
(e.g. the base of a collimator housing) onto the window and
rubber seal.

To mount anode wires, <u>insulators</u> are located and "Araldited" in accurately positioned holes drilled in the end walls. (In this application the area of Araldite exposed to counter gas is small, and in any case is normally in a sealed end compartment and not exposed to water vapour). In the BR and early NC counters, <u>ceramic</u> to metal insulators (Ducon, K1974B, test voltage 17kV at 60 Hz RMS, 40% Rel.Hum.) were employed. The task of keeping the ceramic sufficiently clean to prevent EHT leakage paths (with subsequent X-ray like pulses) was difficult and required continuous attention. The change to "<u>glass to metal</u>" seals {Lactronics, (U.S.A.) 95.2042, flash over voltage 13.2kV} in the T8 counters is apparently a successful one, with standard cleaning (ether, plus ultrasonic clean in distilled water) removing all obvious discharge effects.

Tungsten <u>anode wires</u> have been used throughout. The tungsten (normally $7_{10}-3$ cm diameter) is spot welded at each end onto thick (~ 0.5 cm diameter) nickel wire. (A double weld is used for strength, and care is taken to remove the sharp pointed end of the tungsten). The wire is pulled taut through the insulators, and the nickel soldered to the outer insulator ends. Using a tension T, a wire of length l and mass per unit length M has resonant frequencies at

$$\nu_{res} = \frac{n}{2l} \sqrt{\frac{T}{M}}, \quad n = 1, 2, \ldots \quad (4.1)$$

With $T \sim 5_{10}6$ dynes, the T8 anodes of length ~ 30 cm and mass per unit length $3_{10}-3$ g cm^{-1}, resonate at frequencies $\not> 700$ Hz. Although such low frequencies maybe associated with launch vibrations, sinusoidal vibrations with accelerations up to 6G (as described in 2.7.2) have been applied to all counter types with no adverse affects (see also flight III and IV results, sections 5.3, 5.4 respectively).

Multianode configurations have been employed in all UAT counters, and in each case, X-ray anodes have been electrically isolated from each other and from guard anodes by solid aluminium baffles or wire grids. Baffles of 0.1 - 0.2 cm Al have been used in the BR and NC counters. In the T8 bays, in order to eliminate mass around the sensitive gas volume, widely spaced 0.1 cm nichrome wires have been soldered to supporting brass frames which have been bolted under tension, against the end walls. These wires resonate at about 200 Hz, but are much more ruggedly mounted than the anode wires, and again have successfully withstood vibration tests.

Where solid baffles have been employed, these have determined the relative positions of gas flushing inlet and outlet. The baffles, perforated at one end, are used to form a continuous path for the gas throughout the volume. In all counters gas entry and exit has been through two 1/8" BSP tapped holes ($\sim$0.6 cm diameter), suitably spaced relative to the baffles, or at diagonally opposite corners in the case of the T8 counters. The BSP thread is immediately compatible with the Schrader tank valve (type 1468B). In the actual rocket payload, all Schrader valves are situated together in a spot accessible from outside the ring or nose cone (e.g. through a small cover plate), and the gas is fed to the counter through $\sim$0.3 cm bore copper tubing. The gas flow becomes turbulent when the Reynolds number, $R = \left(\frac{m}{\pi\eta kT}\right)\frac{Q}{a}$ $>$1000, where for argon the term in brackets = 2.23_{10} -3 microns^{-1} cm^{-2} sec, Q is the flow rate and a the tube diameter (Dushman and Lafferty, 1962). In this case turbulent flow occurs when Q $\simeq$ 1.3_{10} 5 microns litre sec^{-1}, which at one atmosphere implies a flow of $\sim$10 litres min^{-1}. Flush rates are usually $<$ 1 litre min^{-1}.) Despite the different gas

paths, no significant differences have been noticed in the
"flush-up times" of NC and T8 counters with similar gas
volumes.

C3   COLLIMATORS

A wide variety of collimator geometries have been
employed. Commercially available <u>honeycomb</u>, $\sim$ 0.3 cm cell
diameter and $1\frac{1}{2}$" (3.8 cm) deep and constructed from 1 thou
(2.5_{10} -3 cm) Al is a convenient form.

Rectangular cell collimators have been constructed from
9 thou (2.3_{10} -2 cm) alloy strips, supplied in convenient
"venetian blind" widths ($1\frac{1}{2}$", 2"), by Hunter Douglas (N.S.W.).
The T8 collimators requiring greater depth and rigidity have
been cut from 12 thou (3_{10} -2 cm) Al sheet. In the small
flight I to III collimators a "<u>louvre-type</u>" construction
technique was employed using relatively thick slats
parallel to the spin direction (see 3.6.1) and channelling
these on each side at the desired spacing to accept louvres
of the thin alloy which were punched or glued into position.
In larger collimators the aluminium strip has been fed through
a <u>die</u>, which punches a series of narrow 'V' shaped
indentations of fixed depth and at fixed separation. The
strip is then cut into counter lengths and assembled so that
every strip stands off its neighbour because of the
indentations. The "stand off" distance (equivalent to the
depth of the V) normally represents the collimator width in
the spin direction, and the separation between the V's, the
width perpendicular to the spin direction. The collimators
are firmly contained in a collimator "housing" which bolts
down onto the counter body. The latter method of collimator
construction is easily adapted to cases requiring collimator
axes inclined to the rocket (and collimator housing) axes,

(e.g. to obtain diagonal fields of view (3.6.1) or fields tilted away from the rocket equatorial plane.) Two or three bars running across the top of the collimator slats and firmly bolted onto the counter body have adequately supported the collimator, and thus window, in vacuo.

Vibration tests on the large area "die-constructed" collimators have indicated a considerable movement perpendicular to the strip direction. This could be particularly serious during the Raven motor burn when the window will bulge between the strips due to reduced atmospheric pressure. This has been countered by replacing two or three strips by one 0.3 - 0.4 cm aluminium strip, which bolts to the supporting bars across the top of the collimator wherever the two intersect.

C4   MECHANICAL INTEGRATION

In all cases mounting has contributed appreciably to the mass about the counter. Counters located in a sealed portion of the rocket head (i.e. the LND and BR counters) were sealed directly onto the rocket wall via a mounting collar, milled from 1.25 cm Al plate, and surrounding the counter window. Flat gaskets were inserted between the collar and the ring wall and held fast by 2BA bolts from outside the wall. The collars were sealed onto the counter with araldite (LND) or gasket (BR), while the collimators were independently inserted from outside the ring.

In both NC and T8 locations, the counters (including their collimators) mount directly onto bulkheads. The most satisfactory mounting method involves an additional Al plate (1.25 cm) milled out to fit the top of the counter. High tensile steel rods, fixed through the overlapping

corners of the plate are then bolted down through the bulk-head (or in the case of multi-tiered counter arrays, through the previous "top" plate), firmly anchoring the counter. For the smaller electronics packages, direct bolting onto the bulkhead floor is normally sufficient.

C5   MECHANICAL TESTS

Preliminary tests on the strength of plastic window materials have been carried out. These include pressure cycling the window against representative collimator cell-size apertures with pressure differentials exceeding $1\frac{1}{2}$ atmospheres across the window. Representing the worst situation encountered, 40G Propafilm has survived several cycles against ~ 0.5 cm x 2.5 cm cells {of 7 thou $(1.8_{10} -2$ cm) wall thickness}, with no adverse effects. For an indication of temperature performance the plastic films have been pressed against the back of a collimator for periods of 5-10 minutes, while the front of the collimator rests on a hot plate at 200-300°C. Propafilm was marked but never punctured in these tests.

All NC and T8 counters have been subjected to pressure tests in which the fully assembled and sealed counter is placed in a tank, subsequently evacuated. Strain guages have been employed to measure the "bulging" of walls and collimators etc. For example, the collimator and the solid (0.6 cm) back plate of a T8 counter distort a maximum of 0.2 cm and .05 cm respectively at their centres; the walls of the NC counters move out .06 cm. The reinforcing bars and rods etc. have been shown to be adequate in all flight counters.

These pressure tests have also been used for preliminary leak detection, by monitoring pressures inside and outside the counter. The technique involves leaving the counter volume exposed to the atmosphere during evacuation of the tank. Once the tank pressure is less than ~1 torr, the counter has been sealed and the rate of pressure decrease recorded. A leak rate criterion of .5 torr per minute (at 760 torr) has been achieved in all cases and most counters are up to an order of magnitude better than this. The worst leak corresponds to a gas gain change during a typical flight duration of 6 min, of less than 5% (see table 3.1). Where bad leaks have been first recorded, the most direct and effective method of location has been to pressurise the counter (to ~ $1\frac{1}{2}$ atmospheres) and submerge it in distilled water. For smaller leaks, indicated by the pressure test over long periods, or by a poor shelf lifetime as a proportional counter, a helium leak detector has been employed, using a "sniffer" to detect helium leaking from the pressurized counter. In most cases, excellent counter lifetimes are achieved after the "water test".

All flight counters have been vibration tested according to specifications described in 2.7.2 and with results indicated in the previous sections.

APPENDIX D

1. (Frontispiece)   Skylark Launch.

2. Flight III Launch and Recovery.
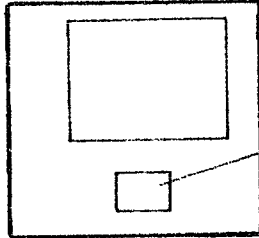
UAT Base Ring recovered in
excellent condition despite
parachute failure.

3. Flight IV UAT Payload.

Proportional counters NC-3(slat)
                      NC-2(slat)
             NC-1(Honeycomb)
    Electronics(Electron exp.)
   Base Ring(Det.A,honeycomb)
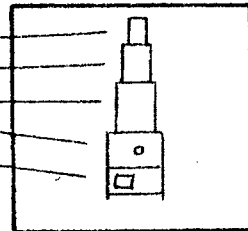
4. Flight IV Vehicle Disintegration (+ 5 secs).
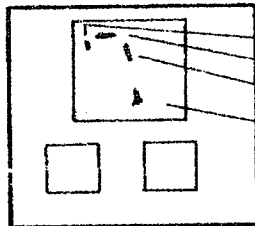
Nose Cone Half
Head (including UAT payload)
Main Motor (unignited)
Cuckoo boost.

5 + 6. Flight V, VI Detectors.
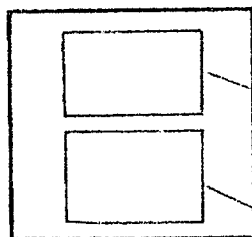
NC Anode
assembly

T8 Anode
assembly
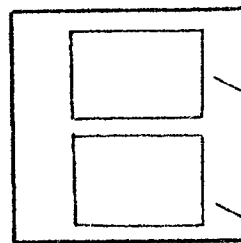
T8 Diagonal
Collimator

T8 fully
assembled
(Vertical
Collimator)